THE UNIVERSITY OF MANITOBA

INFLUENCE OF Nb AND Mn ADDITION ON PHASE TRANSFORMATIONS IN Ti-45 At.% Al GAMMA TITANIUM ALUMINIDES

By

UTTARA PRASAD

A Dissertation Submitted to the Faculty of Graduate Studies
in Partial Fulfillment of the Requirements of the Degree of

DOCTOR OF PHILOSOPHY

DEPARTMENT OF MECHANICAL AND INDUSTRIAL ENGINEERING
WINNIPEG, MANITOBA

MARCH 2002

THE UNIVERSITY OF MANITOBA

FACULTY OF GRADUATE STUDIES

*****

COPYRIGHT PERMISSION

INFLUENCE OF Nb AND Mn ADDITION ON PHASE TRANSFORMATIONS IN Ti-45 At.% AL GAMMA TITANIUM ALUMINIDES

BY

UTTARA PRASAD

A Thesis/Practicum submitted to the Faculty of Graduate Studies of The University of Manitoba in partial fulfillment of the requirement of the degree

of

DOCTOR OF PHILOSOPHY

Dedicated to

My Parents…

ACKNOWLEDGEMENTS

I take this opportunity to thank Dr. M.C. Chaturvedi for his guidance and encouragement throughout the course of this work.

Thanks are due to Dr. N.L. Richards for his valuable suggestions and discussions and also to Dr. J.R. Cahoon for many helpful discussions. I would also like to acknowledge the technical assistance of Mr. John Van Dorp, Mr. Don Mardis and Mr. Mike Boskwick at various stages of this work.

I would also like to thank my colleagues Doug and Lanre for their help and support, especially, Doug for his assistance in all the computer software and hardware related issues.

Last but not the least I would like to thank my family members, especially, my parents and my sisters, Soma and Anupriya, for their constant moral support and encouragement.

Abstract

The effect of alloying elements specifically, Nb and Mn and heat treatment variables such as temperature, time and cooling rate on phase transformations in TiAl-based alloys, was evaluated on small alloy samples by heat treatment and subsequent microstructural characterization by optical, scanning and transmission electron microscopy. The alloys used in this investigation had nominal compositions of Ti-45Al (alloy I), Ti-45Al-2Nb (alloy II), Ti-45Al-2Nb-0.4Mn (alloy III) and Ti-45Al-2Nb-2Mn (alloy IV), all compositions in atomic percent. The effect of alloying elements (Nb and Mn) and cooling rate on phase transformations was studied by cooling small samples from the alpha-phase field at various cooling rates. Small specimens (~12mm x 6mm x 6mm) were encapsulated in vycor capsules that were evacuated and backfilled with commercial purity argon. The encapsulated specimens were annealed at 1350°C (in the α-phase field) for 30 minutes and subsequently cooled to room temperature by furnace cooling (FC), air cooling (AC), oil quenching (OQ) and water quenching (WQ). The cooling rates induced by FC, AC, OQ, and WQ were measured to be 2-3 °C/min, 25 °C/sec, 155 °C/sec and ~1000 °C/sec, respectively. The microstructure of the heat-treated alloys was observed to vary significantly with cooling rate, and the cooling rate dependence of microstructural evolution was observed to be a strong function of alloy composition. FC resulted in the formation of equilibrium lamellar microstructure. The alloys' susceptibility to massive transformation was found to increase with increased cooling rate. The critical cooling rate required for massive transformation was also observed to vary with alloy composition. The susceptibility to massive transformation decreased with an increase in Mn

concentration, that is, the critical cooling rate increased with increase in Mn concentration in the alloy. The rate of transformation, on the other hand, was found to increase with Mn concentration in rapidly quenched specimens. The effect of alloying elements on microstructural evolution has been rationalized in terms of their site occupancies in TiAl and their influence on phase boundaries and on grain size. Based on the microstructural characterization by TEM, tentative mechanism of massive transformation in TiAl-based alloys has been proposed. Schematic CCT diagrams of the four alloys used in this investigation have also been proposed. Alloys III and IV, that contain Mn, exhibit greater potential for microstructural modification.

The effect of grain size on the rate of massive transformation was also investigated on alloy III. Small samples were first wrapped in Ta-foil, encapsulated in vycor capsules and heated at 1350°C for various periods of time, specifically, 30 min, 90 min and 150 min so as to obtain different grain sizes and were subsequently quenched. It was observed that at a fixed composition and cooling rate, an increase in grain size resulted in a decrease in the rate of massive transformation. Schematic CCT diagrams have also been proposed that demonstrate the effect of grain size on the mode of transformation.

The grain growth kinetics of alloy II and alloy III at 1350°C was studied by annealing the alloy samples for various time periods ranging from 15 to 240 minutes. Grain growth equations for both the alloys have been established. The rate of grain growth in alloy II was found to be slower as compared to alloy III. The grain growth exponents for alloy II and III were determined to be 0.38 and 0.52, respectively.

TABLE OF CONTENTS

List of Figures

Chapter 2:

Chapter 3:

Chapter 4:

Chapter 5:

List of Tables

Chapter 5:

Chapter 1

INTRODUCTION

Titanium aluminide TiAl-based alloys have captured a great deal of attention from the aerospace, automotive, and power generation industries due to their potentially attractive properties for high temperature structural applications [1-11]. The ordered structure of titanium aluminides reduces dislocation mobility and diffusion processes at high temperatures and consequently, promotes the retention of strength at high temperatures. Titanium aluminides have high specific moduli, high specific strength, and good oxidation resistance below 850°C [5,10,11]. Various components of gas turbine engines including the rotating parts like low pressure turbine blades, high pressure compressor blades, high pressure turbine blade cover plates, and the stationary parts like transition duct beams, vanes, swirlers, cases, and nozzle flaps and tiles have been identified to be made of γ titanium aluminide based alloys [1-10].

The γ titanium aluminide alloys of engineering importance are based on Ti-(45-48)Al with appropriate combination of other alloying elements. The new generation of alloys under development have compositions of Ti-(45-47.5)Al-(1-2)M-(2-6)N-x(W, Hf, C)-(0-0.3)B, where M= Cr, V, Mn and N= Nb, Mo, Ta [5,11,12]. These are two phase alloys containing the ordered phases, α_2 (DO_{19}) and γ ($L1_0$). Four major types of microstructures have been identified to be present in these alloys: near γ, duplex, nearly lamellar, and fully lamellar [5,12-18]].

Mechanical properties of titanium aluminides are strongly dependent on microstructure. Alloys with duplex microstructure exhibit highest ductility and strength. On the other hand, higher toughness values and good creep properties have been observed in alloys having fully lamellar microstructure. The tensile properties of alloys with fully lamellar microstructure can however be improved by reducing the grain size. An optimum balance of all the mechanical properties can therefore be achieved by controlling the proportions of equiaxed and lamellar grains and also by controlling the grain size. These microstructural modifications can be brought about by varying the alloy chemistry, alloy processing and by thermal and thermo-mechanical treatments.

In order to obtain a desired microstructure for desired properties in these alloys, a comprehensive understanding of phase transformations that take place in the Ti-Al system, and a better insight into the effect of various processing and heat treatment variables on these transformations are essential. Extensive research over the last two decades has enabled the researchers to identify numerous modes of phase transformations in the Ti-Al system during various heat treatments. The important transformations relate to the $\alpha \rightarrow \alpha_2$ ordering reaction, formation of two-phase γ/α_2 lamellar microstructures, discontinuous coarsening of lamellar microstructures, $\alpha \rightarrow \gamma_m$ massive type transformation and formation of monolithic γ grains. The transformation mode depends on the alloy composition, applied stress, temperature of transformation, and the heating and cooling rates experienced during the heat treatments. An effective control of these parameters allows development of the desired microstructure. Numerous researches have been, and

are being, conducted in order to gain a better understanding of the phase transformations in titanium aluminides, but most of these studies have been limited to the binary system.

The γ-based titanium aluminide alloys of current interest contain ternary and quaternary alloying elements, which also play a significant role in determining the transformation mode operative during a particular heat treatment. A more systematic research is, however, required to completely understand the phase transformations and the effect of various parameters on these transformations so that a relationship between the microstructure and mechanical properties can be better understood, and more confidently predicted. The present investigation was therefore, undertaken to study the effect of various parameters, such as composition, grain size, heating time and temperature, on phase transformation behavior in Ti-45(at.%)Al based titanium aluminides. This fundamental research will be helpful in enhancing the current state of knowledge in the field of phase transformations in titanium aluminides, especially in the presence of ternary and quaternary alloying elements. This will be beneficial in understanding the microstructural evolution and will provide us with a sound base for designing an alloy with a proper combination of mechanical properties required for specific applications.

Chapter 2

LITERATURE REVIEW

2.1. PHASE EQUILIBRIA

2.1.1 Binary Ti-Al Phase Diagram

The Ti-Al phase diagram has been under study since 1950's. However, the strong effect of interstitial elements has hampered its accurate determination. The first detailed study of the Ti-Al phase diagram was carried out by Ogden *et al.*[19] in 1951. They summarized the results of prior investigations and proposed a phase diagram for the Ti-Al system. In 1952, Bumps *et al* [20] studied the Ti-Al system much more carefully and in greater detail. They proposed a complete binary Ti-Al phase diagram (Figure 2.1), which was based on their own results and the other available data.

Murray [21] revised the Ti-Al phase diagram in 1988 and proposed a eutectoid reaction at 1125°C. The phase diagram was further revised by McCullough *et al* [22], who introduced two peritectic reactions, $L+\beta \rightarrow \alpha$ and $\alpha+L \rightarrow \gamma$, and indicated the absence of the peritectoid reaction at 1285°C. This was later confirmed by Jones and Kaufman [23]. Ding *et al* [24] also confirmed the absence of the peritectoid reaction at 1285°C. They suggested that the eutectoid reaction, which involves co-operative growth of the two product phases, was virtually impossible to achieve experimentally in this system because of the large differences in the transformation kinetics of the two product phases, viz.,

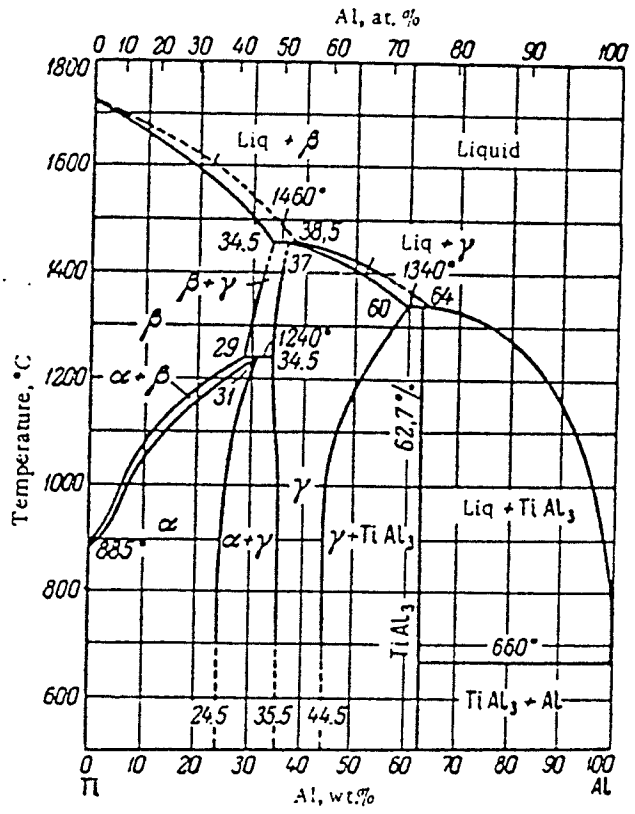

Figure 2.1: Binary Ti-Al phase diagram proposed by Bumps *et al.* [20]

α_2 and γ. The γ phase can precipitate either from α or α_2 phase depending upon the composition of the alloy and the cooling rate. Kattner *et al.* [25] assessed the binary Ti-Al phase diagram using three different analytical thermodynamic descriptions. They showed that the calculated phase diagram agrees well with the critically evaluated experimental data from the literature.

The currently accepted Ti-Al phase diagram is shown in Figure 2.2 [26]. Recently, Veeraraghavan *et al* [27] also studied the Ti-Al system in the composition range of 25-52 at.% Al using electrical resistivity measurements. They have made slight modifications to the binary phase diagram proposed by Mishurda *et al.* [28] in the composition range of 25-43 at.% Al, and have suggested the absence of the $\beta+\alpha\rightarrow\alpha_2$ peritectoid reaction. Their proposed modifications are shown in Figure 2.3.

It should also be noted here that most of the investigations on binary Ti-Al phase diagram has been limited to the Ti-rich and the central part of the system. The Al-rich part of the Ti-Al system is still not well established. The most recent work on Al-rich part of the Ti-Al system has been done by Braun and Ellner [29]. They studied a number of alloys in the composition range of 50 to 76 at.% Al and have suggested the presence of seven stable intermetallic phases in this composition range.

Despite numerous investigations on the Ti-Al binary system, several phase boundaries are still uncertain and hence, it is not possible to precisely define the transformation paths for phase transformations.

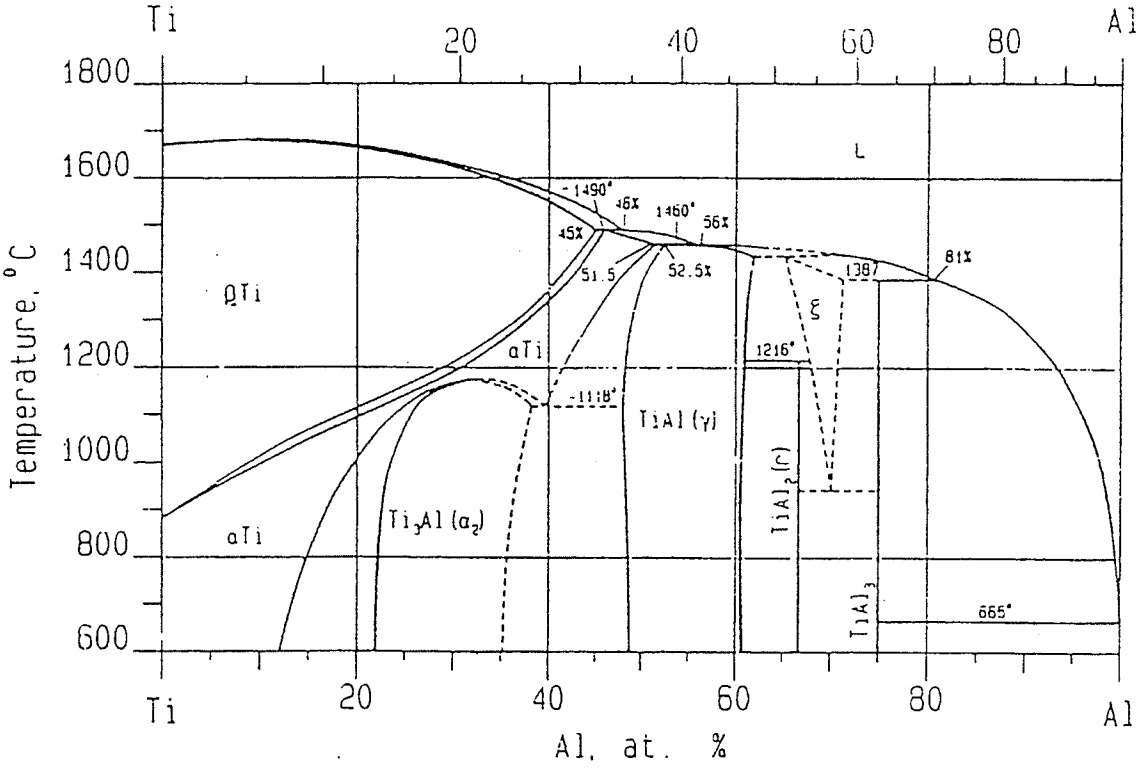

Figure 2.2: Currently accepted binary Ti-Al phase diagram. [26]

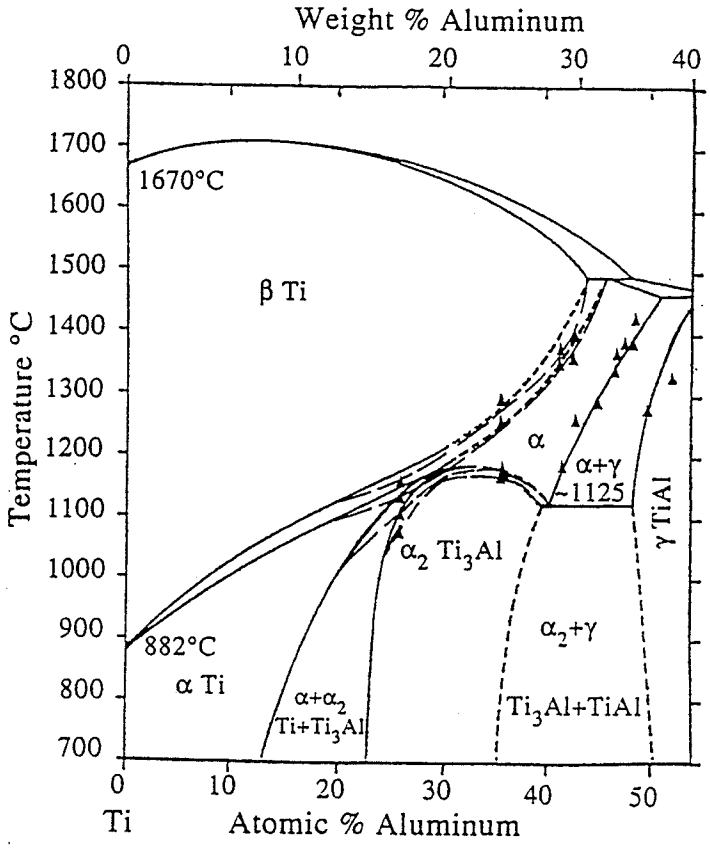

Figure 2.3: Modified Ti-Al phase diagram. [27]

2.1.2 Crystal Structure and Characteristics of Phases

2.1.2.1 TiAl: One of titanium aluminides, TiAl is often designated as the γ phase. It crystallizes with the tetragonal $L1_0$ crystal structure (AuCu-type). The TiAl unit cell is illustrated in Figure 2.4. The $L1_0$ crystal structure results due to ordering in the fcc lattice (Al). The face centered cubic structure is tetragonally distorted because alternate (002) planes are occupied by atoms of the same component. The c/a ratio is 1.015 at the stoichiometric composition. The crystal structure data of γ phase are given in Table 2.1 [30,31]. The γ phase remains ordered up to its melting point.

The maximum composition range over which TiAl is stable is 48-60 at.% Al. The high aluminum content of this compound also increases its resistance to oxidation and burning [13]. TiAl has low density which is an important attribute for jet engine applications as light weight enhances engine performance. The heat of formation of –40 kJ/g-atom of TiAl suggests formation of strong bonds that lead to higher activation energy for diffusion, and help in strength retention at higher temperatures and in increased resistance to creep. However, γ phase lacks ductility and toughness. These mechanical properties can be improved through microstructural control and suitable alloying additions.

2.1.2.2 α-phase: The α-phase is a disordered hexagonal phase and its unit cell is shown in Figure 2.5. This is stable only at higher temperatures with a metastable extension at lower temperatures. When cooled at relatively high cooling rate, it transforms to an ordered α_2-phase (Ti_3Al).

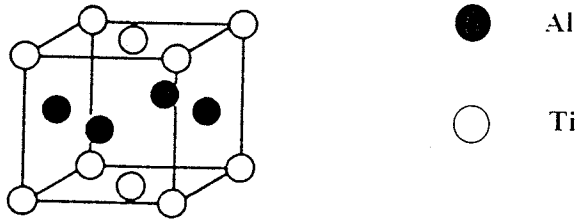

Figure 2.4: TiAl unit cell.

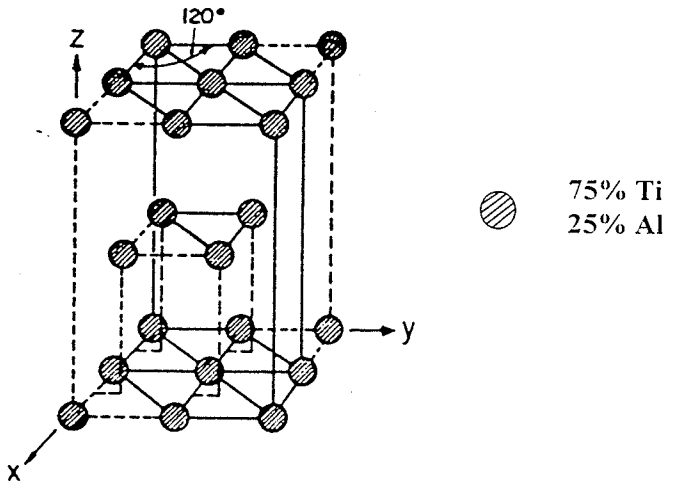

Figure 2.5: Disordered HCP (α) unit cell.

Table 2.1 Crystal Structure data of phases. [30]

Phase	Strukturbericht symbol	Crystal structure	Space group	Lattice parameter		
				a	b	c
Ti_3Al (α_2)	DO_{19}	Ordered hexagonal	$P6_3/mmc$	0.5782	_	0.4629
TiAl (γ)	$L1_0$	Ordered F.C.T	P4/mmm	0.4005	_	0.4070
B2	DO_3	Ordered bcc	$Pm\ \bar{3}m$	0.322	_	_
ω–type	$B8_2$	Hexagonal	$P6_3/mmc$	0.45803	_	0.55204
ω	_	Hexagonal	P6/mmm	0.46	_	0.58
ω'	_	Trigonal	$P\ \bar{3}m1$	0.4555	_	0.5542

2.1.2.3 Ti_3Al: Ti_3Al is often designated as the α_2 phase. It has a hexagonal ordered DO_{19} crystal structure (Ni_3Sn-type). The schematic unit cell of Ti_3Al is shown in Figure 2.6. The ratio of the lattice parameters, c and a, is 0.8 for stoichiometric composition. The crystal structure data of this phase are given in Table 2.1. The α_2 phase transforms to a disordered phase, α, above 1180°C.

The maximum composition range over which α_2 phase is stable 24 to 36 at.% Al. This also lacks room temperature ductility. The ductility can however, be improved by alloying with sufficient amount of β stabilizing element like Nb [32]. In the presence of Nb, the high temperature β phase is retained upon cooling to lower temperatures, and it becomes ordered B2 phase. The presence of B2 phase is believed to delay the cleavage crack nucleation in α_2 and consequently, a small volume fraction of B2 phase increases the ductility of α_2 alloys to 3-8 %. However, the presence of large volume fractions of B2 phase results in a loss of creep resistance. Efforts have also been made to improve the room temperature ductility of α_2 phase by grain refinement [33,34].

2.1.2.4 β-phase: The β-phase has a disordered bcc crystal structure, Figure 2.7 shows its unit cell. The maximum aluminum concentration of the β-phase is $\sim$ 45 at.% at a temperature of about 1490°C. In the presence of alloying elements such as Nb, it is stabilized and orders to the B2 phase when cooled to room temperature.

2.1.2.5 B2-phase: The B2 phase has an ordered body centered cubic structure (CsCl type) and is formed by the ordering of the high temperature disordered β-phase. Its unit

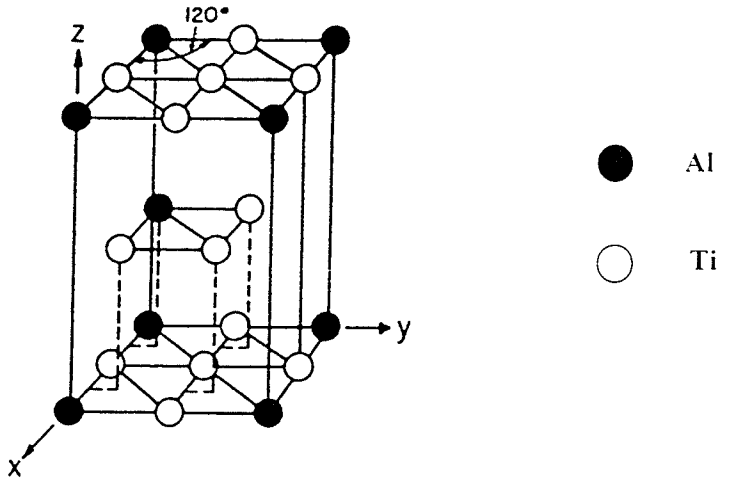

Figure 2.6: Ti_3Al unit cell.

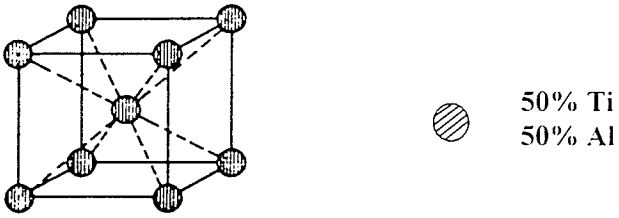

Figure 2.7: Disordered BCC (β) unit cell.

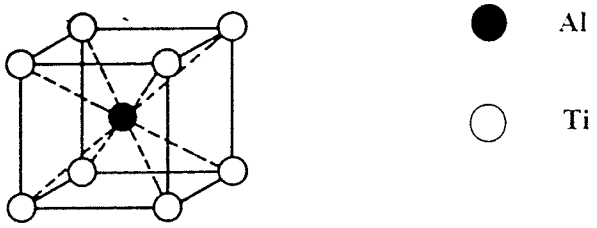

Figure 2.8: B2 unit cell.

cell is shown in Figure 2.8 and the crystal structure data observed in Ti-Al-Nb system [35] are given in Table 2.1. It has a large number of independent slip systems and as a result has a relatively high ductility [32]. However, a large number of slip systems also result in a decrease in creep resistance of the alloy.

2.1.2.6 ω-phase: The ω-type phase which forms as a result of decomposition of B2 phase has a $B8_2$ type crystal structure. The transition phases which appear due to decomposition of B2 phase are referred to as ω′and ω″ [35,36]. The ω-type phase has also been observed in the quenched-in B2 phase [37]. The crystal structure data of ω′, ω″ and ω-type phases are also given in Table 2.1.

2.2. ALLOY MODIFICATIONS

Alloys that have been developed for engineering applications can be grouped into either single phase (γ) or two phase (α_2+γ) alloys. Initially, single-phase alloys attracted a great deal of attention because of their resistance to environmental attack by oxidation and hydrogen absorption. However, their importance as engineering alloys has diminished due to their poor ductility and toughness. TiAl alloys of engineering importance are two phase (α_2+γ) based on Ti-(45-48)Al with appropriate combination of alloying elements. The new generation of TiAl alloys under development have composition of Ti-(45-47.5Al)-(1-2)M-(2-6)N-(0-1)(W,Hf,C)-(0-0.3)B [5,11,12,34,38,39] where M = Mn, Cr, V and N = Nb, Mo, Ta. Presence of these alloying elements alters the phase equilibria and

hence the mechanical properties. A proper combination of these alloying elements can result in the desired improvements in properties for specific applications. Many attempts have been made to improve the mechanical properties of TiAl alloys through various alloy additions.

2.2.1 Effect of Alloying Elements on Phase Equilibria

The alloying elements modify the binary Ti-Al phase diagram and these modifications are mainly manifested as changes in shapes and size of the γ phase field. Three types of isothermal sections (Figure 2.9) have been identified to form in the Ti-Al-X (X = type M or N alloying elements) systems [5,34,40] depending upon the nature of the site occupied by the alloying elements. The type N alloying elements substitute for titanium sites in titanium sub-lattice and increase the aluminum concentration of the γ phase, thereby, forming type I γ phase field. On the other hand, type M elements substitute either for both titanium and aluminum to form type II phase field or for aluminum only to form type III phase field. The aluminum concentration of the γ phase remains the same or increases slightly with an increase in the concentration of type N alloying elements, whereas the aluminum concentration decreases with an increase in the concentration of the type M elements in type II and type III γ phase field. That is, for a given alloy composition, the aluminum concentration of the γ phase varies depending upon the type of alloying elements.

Site preference of an alloying element changes with the overall alloy composition as well as with its concentration in the alloy. Nb has been reported to substitute for Ti in TiAl

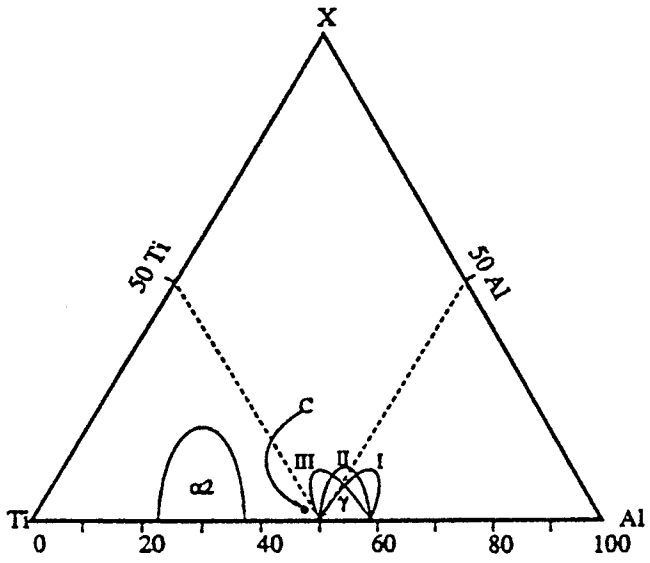

Figure 2.9: Three typical gamma phase fields formed due to addition of alloying elements. [5,34,40]

[41-45] and hence is a type I phase field former. However, in the Ti-48Al-2Nb alloy, aluminum concentration has been observed to be the same as that in the binary Ti-48Al alloy [34], and at Nb concentrations of 2 to 8 at.%, a segment of the phase boundary was found to extend across the 50 at.% Al line resulting in a lower aluminum concentration in the γ phase [34,41]. The reason for this ambiguity has been not yet explained. Moreover, it has been also suggested that site occupancy behavior of Nb does not change with composition [44,45]. Mn, on the other hand, has been reported to have a strong tendency to occupy Al sites in TiAl [42-45] when present in small amounts and hence is a type III phase field former. In Ti-48Al-2Mn alloy, the aluminum concentration of the γ phase is lower than that in the Ti-48Al alloy. A similar decrease in aluminum concentration has been observed in the alloy Ti-48Al-(1-3)Cr and Ti-48Al-(1-3)V alloys[5,34]. The probability of M type alloying elements (V,Cr,Mn) occupying Ti sites, however, increases with an increase in their amount in the alloy and also with the overall aluminum concentration of the alloy [44,45].Ternary phase diagrams are available for a number of ternary Ti-Al-M systems, however, only Ti-Al-Mn and Ti-Al-Nb systems have been extensively studied. Precise determination of phase boundaries in the presence of ternary and quaternary alloying elements has not been done and requires a more systematic investigation.

The Ti-Al-Mn System: There is a lack of information on the Ti-Al-Mn system. This system was first studied in 1955 by Domagala and Rostoker [46], who investigated the composition range defined by Ti and the binary compositions of TiAl and Mn_2Ti at temperatures in the range of 700-1200°C. At elevated temperatures, the phase fields α-

Ti(hcp), β-Ti(bcc), (α + β), (α + β + γ–TiAl) and (β + γ–TiAl +Mn_2Ti) were established, but the ordered α_2-Ti_3Al field was not identified. Domagala and Rostoker found that only body centered cubic β–Ti appeared to have large solubility for Mn and they did not report any new ternary phase. Later, work done by Chakrabarti [47] on Mn rich alloys of the Ti-Al-Mn system showed extensive solubility of aluminum in Mn_2Ti. This is a Laves phase of $MgZn_2$ type and is known to exist in the binary Ti-Mn system. Chakrabarti reported a solubility of about 30 at.% Al in Mn_2Ti. His data indicate that the Laves phase extends into the ternary system along a line of approximately constant Ti concentration (~35 at.%). This observation suggests that Al substitutes for Mn in the Laves phase and that the phase should be properly represented by the formula $(Mn, Al)_2Ti$. Jacob and Shaltiel [48] subsequently confirmed this conclusion. Hashimoto *et al.* [49] performed the study in a composition range of 36-38 at.% Al and upto 5 at.% Mn; however, instead of $(Mn, Al)_2Ti$, they reported the formation of a ternary phase $Mn_2Al_3Ti_3$ (ξ–phase) along with α_2–Ti_3Al and γ-TiAl.

Butler *et al.* [50,51] recently investigated the solidification microstructures in the ternary Ti-Al-Mn system for Ti/Al ratio of ~1.14 with Mn levels of 5, 10, 20, and 30 at.% and proposed several isothermal sections of the ternary Ti-Al-Mn phase diagram at high temperatures. They observed that for 5 and 10 at.% Mn alloys, the microstructure consisted of lamellar γ/α_2 and interdendritic γ, β and $(Mn,Al)_2Ti$. Figure 2.10a shows an isothermal section of Ti-Al-Mn system at 1352°C.

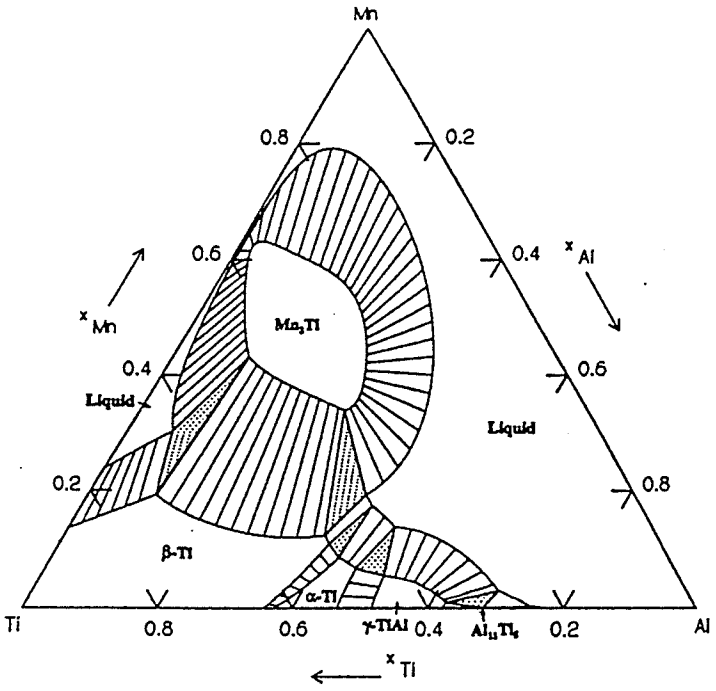

Figure 2.10: (a) Isothermal section of Ti-Al-Mn system at 1352°C. [50]

The Ti-Al-Nb System: Only a limited amount of research has been done to assess the effect of Nb on phase relations and deformation behavior in the ternary Ti-Al-Nb system. Nb behaves as a β stabilizer and also shows solid solution strengthening. However, the main purpose of adding Nb to γ titanium aluminides is to improve the oxidation resistance of the alloy.

Kaltenbach *et al.* [52] studied the binary Nb-Ti and Al-Nb as well as ternary Ti-Al-Nb systems in the year 1989. Li and Loretto [41] studied the microstructural evolution in the Ti-Al-Nb system and based on their results proposed that the addition of Nb expands the γ phase field by shifting the (α+γ)/γ phase boundary towards the Al-lean side. The Ti-Al-Nb system has been recently analyzed in detail by Hellwig *et al.* [53]. They proposed isothermal sections at 1000°C and 1200°C. Several other isothermal sections are also available [54-57]. Figure 2.10b [57] shows the isothermal section of Ti-Al-Nb system at 1400°C.

In Ti-Al-Nb alloys containing 5 to 17 at.% Nb, a ductile ordered bcc phase (B2) forms upon quenching from high temperatures [35,36]. The B2 phase forms by the ordering of equilibrium high temperature β phase in the Ti-Al-X system, where X is a β stabilizing ternary addition [30]. Formation of a number of phases has been also observed subsequent to the ordering of β phase [35,36]. These phases are known as ω or ω related phase. Additionally, an ordered orthorhombic phase has also been detected in Ti-Al-Nb alloys with an approximate stoichiometry of Ti_2AlNb [58,59].

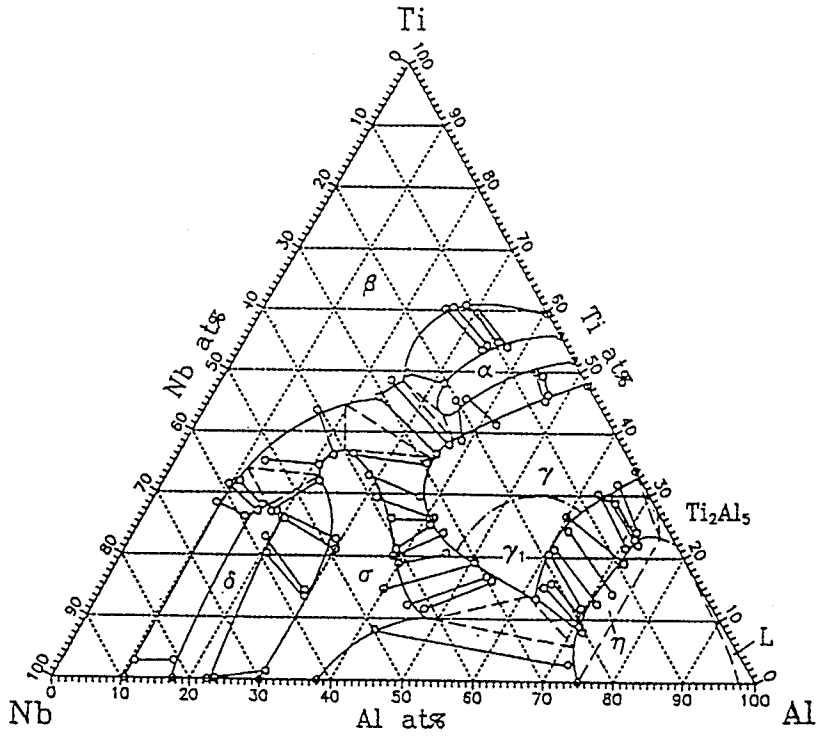

Figure 2.10 (b) Isothermal section of Ti-Al-Nb system at 1400°C. [57]

2.2.2 Effect of Alloying Elements on Mechanical Properties

Single-phase γ is inherently very brittle. Its ductility is, however, a function of the aluminum concentration and increases with a decrease in Al concentration. The M type elements when present either individually or in a combination [5,33,34], enhance the ductility of two phase alloys. For example, an addition of 1-3 at% (V, Cr, Mn, V+Cr or Mn+Cr) to the Ti-48Al alloy almost doubles its ductility [5,60-62]. To be effective in ductilizing, the alloying elements should be limited to 1-3 at.% so that the formation of an excessive amount of B2 phase can be avoided and the duplex microstructure is maintained. Figure 2.11 [13] shows the effect of ternary additions on ductility of TiAl based alloys. Various efforts have been made to identify and understand the causes of ductilizing by elements such as Cr, V, and Mn [13]. Morinaga *et al.* [63] evaluated the effects of alloying elements on ductility of TiAl and concluded that V, Cr, and Mn can effectively improve ductility only when they substitute for Al due to a decrease in bond order. Indeed, these elements preferentially occupy Al sub-lattice sites when present in small concentrations. Their preference for Ti sites, however, increases with an increase in concentration [44,45]. Experimental measurements also show that the presence of Mn reduces the stacking fault energy and hence improves ductility [63,64]. Alloying elements that substitute for Al sites, shift the $(\alpha+\gamma)/\gamma$ phase boundary to Ti rich side of the phase diagram, thereby reducing the covalency of the Ti-Al bond and the stacking fault energy, and are thus able to enhance the ductility of the alloy. Boron imparts ductility to two-phase material by grain refinement [65-67]. Kawabata *et al.* [68] have studied the influence of ternary additions on yield and fracture stresses and fracture strain under various conditions. However, no detailed work has ever been done so as to understand the

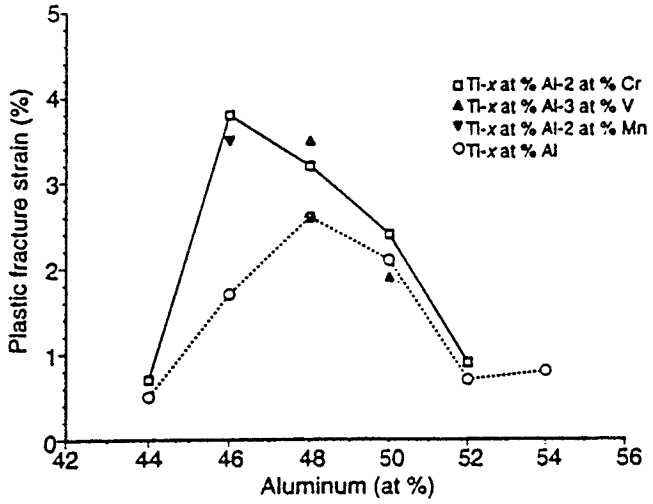

Figure 2.11: Effect of alloying elements and Al content on the ductility of titanium aluminides. [13]

interactive effect of different alloying elements on mechanical properties of TiAl-based alloys. TiAl based aluminides, with the addition of V, have been shown to exhibit superplasticity [69].

Nb and Ta have been reported to improve creep resistance by slowing down the diffusion rate [13] whereas, W and Si improve creep resistance through microstructural modifications [13,70,71]. The addition of W tends to form β particles and at the same time tends to promote lamellar structure and reduce interlamellar spacing. It is however, unclear as to which aspect of the microstructural modification is more responsible for the improvement of creep resistance. Addition of Si causes precipitation of Ti_5Si_3 and also stabilizes the lamellar structure [72-74]. It is also reported to improve creep resistance either by reducing dislocation motion or by stabilizing the lamellar structure. It is well known that lamellar structure has best creep resistance [75]. Addition of small amounts of W, Mo and Si to a Ti-47Al based alloy is reported to reduce creep rate at 760°C by a factor of 30 [76,77]. This increased creep resistance has been attributed to precipitation of silicide and/or formation of mechanical twins parallel to lamellar planes which refines the lamellar spacing. The addition of (1-3) at. % of Cr is also reported to reduce the creep rate of TiAl [78]. The effect of alloying elements on the creep curve of TiAl-based alloys is shown in Figure 2.12 [79]. Recently, it has been reported by Sun *et al* [80] that addition of a small amount of Nd to binary Ti-47.5Al alloy significantly increased its creep resistance at 800°C. In addition, Nd also increased the tensile strength at room temperature and at 900°C.

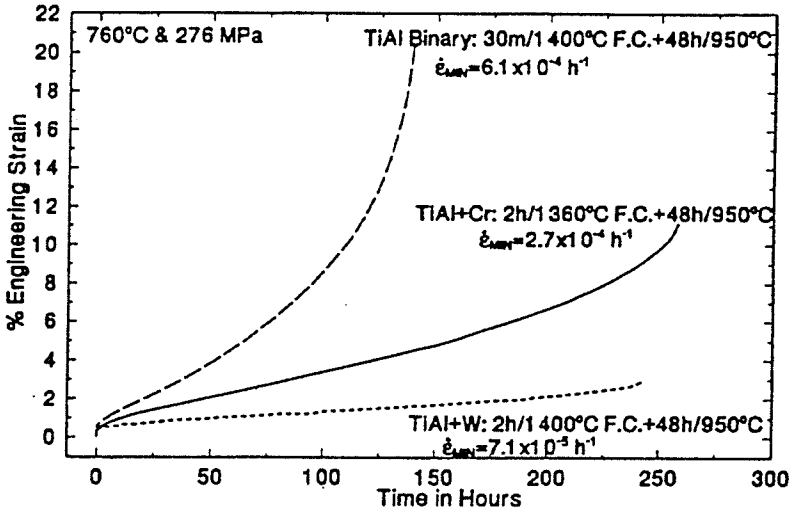

Figure 2.12: Comparison of creep curves for different alloying additions. [79]

The addition of refractory metals such as Nb, Ta and W induces solid solution strengthening. Precipitation strengthening has also been observed in a TiAl-based alloy during aging of alloys containing 0.5 at.% carbon and nitrogen due to precipitation of needle like precipitates of carbide and nitride [81]. The addition of Boron causes precipitation hardening in the TiAl-based alloys [82] and V and Zr are beneficial for yield strength [68,83].

The addition of Mo to TiAl based alloys promotes the formation of B2 phase particles [84]. These particles can form either along the lamellar sub-grain boundaries or at the lamellar interface. Presence of B2 phase particles at grain boundaries promotes grain refinement, which is beneficial to strength and ductility. Moreover, precipitation of B2 particles at lamellar interface increases fracture toughness by diverting cracks away from the brittle interlamellar interfaces [84].

2.3. PHASE TRANSFORMATIONS

The microstructures observed in TiAl-based alloys vary with the alloy composition, processing, post-processing thermal and thermo-mechanical treatments. The microstructures that evolve in the γ-based titanium aluminides can be classified into four broad categories: near γ, duplex, nearly lamellar and fully lamellar. These four types of microstructures are illustrated in Figure 2.13 [10].

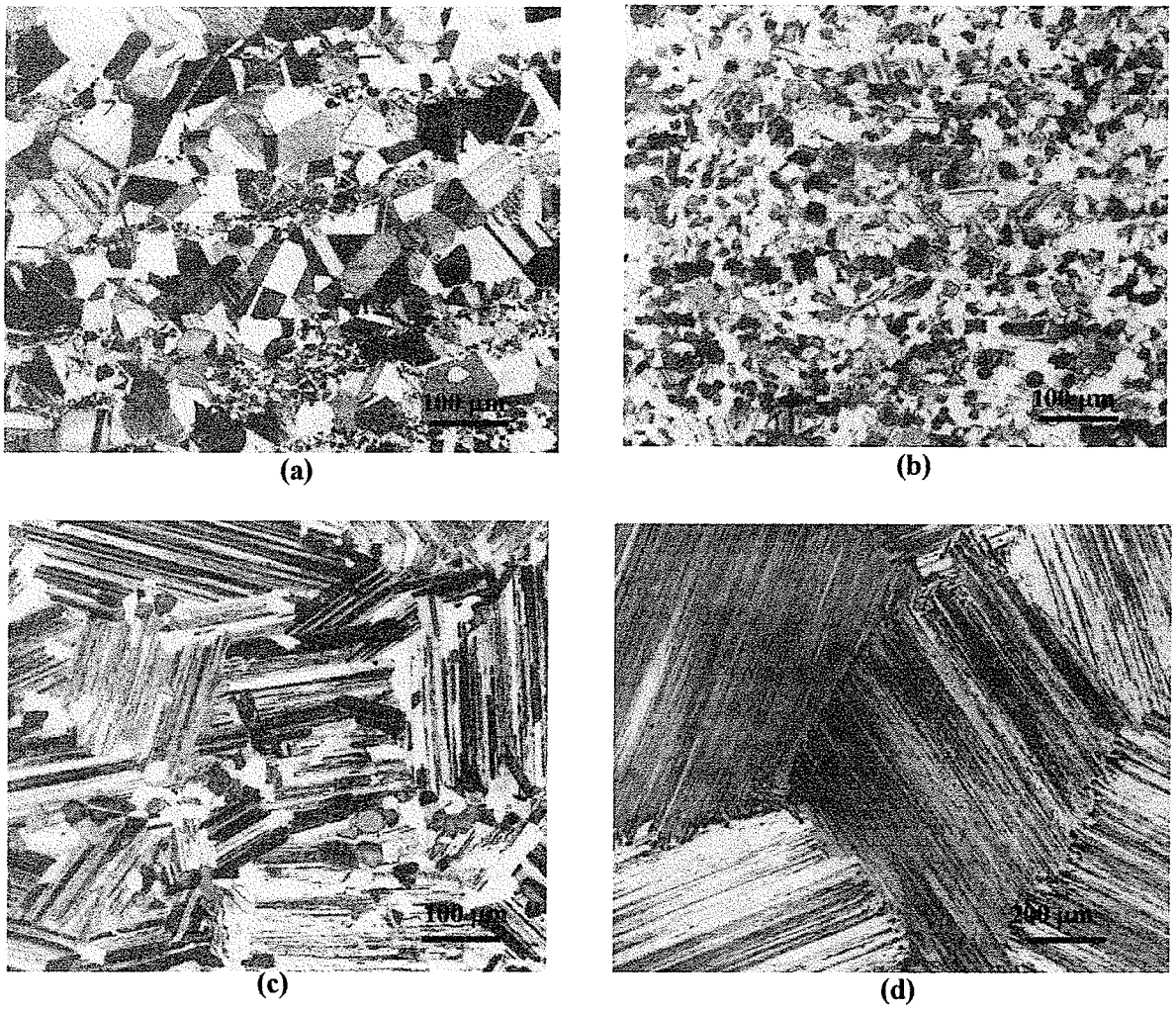

(a) (b) (c) (d)

Figure 2.13: Four typical microstructures of gamma alloys: (a) near gamma, (b) duplex, (c) nearly lamellar, and (d) fully lamellar. [10]

The near γ microstructure consists entirely of γ grains in single-phase alloys, or predominantly γ grains with finely dispersed grain boundary α_2-phase particles in two-phase alloys. The alloys containing more than 52 at.% Al always lie in the single γ-phase field. But, for alloys with aluminum concentration of 46 to 50 at.% Al, heat treatments at temperatures just above the "eutectoid" temperature yield a near γ structure. This type of microstructure is generally non-uniform and coarse grained. Duplex microstructure is typically the finest and is produced after annealing in the $\alpha+\gamma$ phase field at temperatures where the volume fraction of γ and α-phases is approximately equal. When cooled to room temperature, the duplex microstructure consists of equal proportions of equiaxed γ grains and γ/α_2 lamellar grains. The grains are typically 10-35 μm in diameter, and the lamellar plates are 0.1-2 μm thick. The heat treatment of alloys, that contain less than 48 at.% Al, at temperatures close to the α-transus ($\alpha/(\alpha+\gamma)$ phase boundary) result in nearly lamellar microstructures which consist primarily of coarse lamellar grains with small amounts of γ grains. Lastly, heat treatment at temperatures above α-transus result in fully lamellar microstructures consisting of alternate layers of γ and α_2 plates. The grains have relatively coarse grain size suggesting coarsening of α-grains above the α-transus temperature.

The mechanical properties of titanium aluminides, like all other alloys, are known to be strongly dependent on microstructure. In order to obtain a desired microstructure for desired properties, one needs to have a comprehensive understanding of the phase transformations that occur in the Ti-Al system. The mode of transformation depends on the alloy composition, applied stress, temperature of transformation, and the heating and

cooling rates experienced during the heat treatments. Some, but few, attempts have been made to investigate the effect of these parameters on transformation modes. These studies have led to the establishment of continuous cooling transformation (CCT) and time-temperature-transformation (TTT) diagrams for some gamma based alloys. The CCT curves of the binary TiAl based alloys with compositions ranging from 40 – 48 at.% Al are shown in Figure 2.14(a-d) [23]. TTT diagrams have also been developed for some TiAl based alloys. Numerous modes of phase transformations have been identified to be operative in the Ti-Al system during various heat treatments. The important transformations relate to the $\alpha \rightarrow \alpha_2$ ordering [23,85-87], formation of two phase γ/α_2 lamellar structure [23,88-97], discontinuous coarsening of the lamellar structure [95-102], $\alpha \rightarrow \gamma_m$ massive type transformation [41,103-118] and formation of monolithic γ grains. Various aspects of some of the important transformations are discussed in the subsequent sections.

2.3.1 The $\alpha \rightarrow \alpha_2$ Ordering Reaction

The $\alpha \rightarrow \alpha_2$ transformation is a simple ordering reaction that involves ordering of the α-phase which is a high temperature disordered hexagonal phase. The transformation of α to α_2 can occur quickly and without any significant undercooling.

The nature of decomposition of the α-phase is a strong function of both the composition and the cooling rate. The CCT diagrams presented in Figure 2.14 [23], show that the α-phase can completely transform to α_2 phase upon water quenching in the alloys with aluminum concentrations between 40-45 at.%. The $\alpha \rightarrow \alpha_2$ ordering reaction has indeed

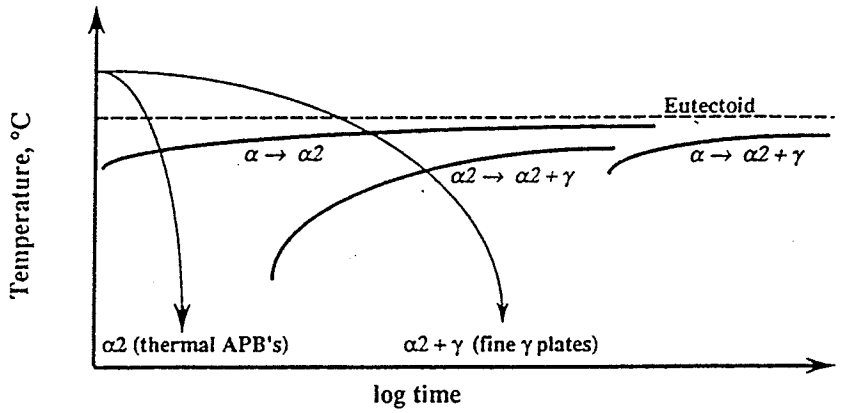

(a)

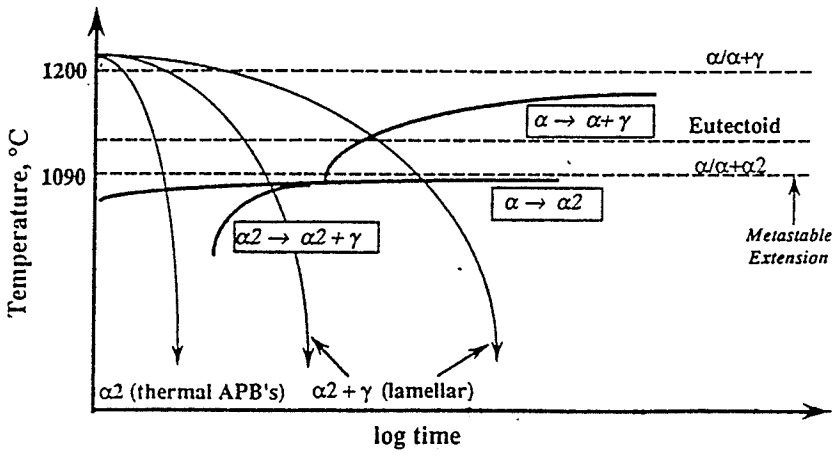

(b)

Figure 2.14 (continued...)

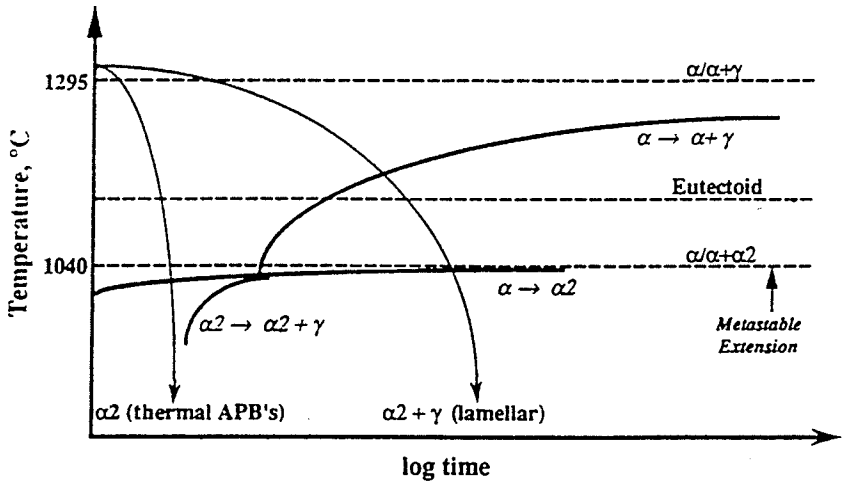

(c)

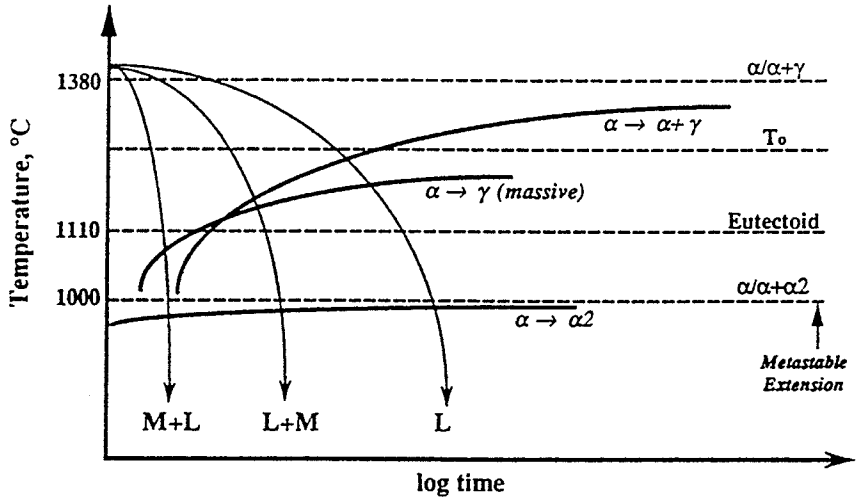

(d)

Figure 2.14: Schematic CCT diagrams for alloys containing (a) 40 at.% Al, (b) 42 at.% Al, (c) 45 at.% Al, and (d) 48 at.% Al. [23]

been observed in Ti-45Al binary alloy [86-87]. However, in the same composition range a slower cooling rate has been observed to yield two phase lamellar structure consisting of γ and α_2 phases [23]. Also, in the alloys where the aluminum concentration is greater than 45 at.% (e.g 48 at.%), it is almost impossible to have the ordering reaction occur prior to other modes of transformation. When aluminum concentration is less than the so called "eutectoid" composition (~40 at.% in binary Ti-Al system), slower cooling (e.g air cooling) also results in ordering of α-phase to α_2 phase. As discussed before, α_2 phase is a brittle phase and is highly prone to oxidation. It is hence not a desirable microstructure. During heat treatments, the aim should always be to have the α-phase decompose and prevent it from ordering before other transformation modes become operative.

2.3.2 The Formation of $\alpha \rightarrow \alpha_2/\gamma$ Lamellar Microstructure

The decomposition of high temperature disordered hexagonal α phase during subsequent cooling gives rise to the formation of two ordered phases, γ (TiAl) and α_2 (Ti_3Al). The α_2 and γ phases are present as alternate lamellae with the orientation relation: $(0001)_\alpha // (111)_\gamma$ and $\langle \bar{2}110 \rangle_\alpha // [110]_\gamma$. This relationship is known as Blackburn's relationship and has been confirmed in a number of studies [23,88,118]. In a lamellar colony, all α_2 lamellae have the same crystallographic orientation due to the fact that there is only one orientation variant for $\alpha \rightarrow \alpha_2$ transformation. It has been also observed that each γ lamella has a number of order domains and adjacent lamellae are twin or pseudo-twin related [85,95,96]. Three types of lamellar microstructures, designated; Type I, II, and III, have been identified through detailed microstructural development studies

[10,34]. Types I and II microstructures are formed when the decomposition of high temperature α phase involves the precipitation of the γ plates through reactions: $\alpha \rightarrow \alpha+\gamma \rightarrow \alpha_2+\gamma$ and $\alpha \rightarrow \alpha_2 \rightarrow \alpha_2+\gamma$, respectively. Both reactions result in alternating α_2 and γ plates with the orientation relationship $(0001)_\alpha // (111)_\gamma$ and $[\bar{2}110]_\alpha // [110]_\gamma$. The fully lamellar microstructure and many of the nearly lamellar microstructures are of this type. Type II lamellar microstructures are typically observed in the duplex alloys and in lower aluminum concentration alloys (40-44 at.% Al) when cooled at relatively high cooling rates [34]. Type III microstructures are formed by the growth of α plates in γ matrix when a hot worked two phase alloy is heated in the $\alpha+\gamma$ phase field. The resulting microstructure consists of alternating plates of α_2 and γ which have the usual orientation relationship. The only difference between the Types I and II, and the Type III is that in Type I and Type II the γ plates are twin related whereas in Type III, the γ plates have the same orientation within a grain.

2.3.2.1 The Mechanism of lamellar transformation: Several investigations have been conducted to establish the mechanism of decomposition of the α phase and subsequent formation of $\alpha_2+\gamma$ lamellar microstructure [23,85,95,96,106 112]. The formation of the lamellar microstructure does not occur through a eutectoid reaction, because of the large difference in the kinetics of formation of the two constituent phases (α_2 and γ) [23,96]. Instead, the transformation results from the precipitation of the γ lamellae in either a disordered α, or an ordered α_2 matrix [96], following one of the two reaction sequences: (1) $\alpha \rightarrow \alpha_2 \rightarrow \alpha_2 + \gamma$ or (2) $\alpha \rightarrow \alpha + \gamma \rightarrow \alpha_2 + \gamma$. The lamellar microstructure formation

involves ordering of α to α_2 phase, a crystal structure change from hcp to fcc, a chemical composition change through atom transfer, and an ordering reaction of the fcc type crystal structure leading to the final $L1_0$ γ phase [96]. A fully lamellar microstructure can be formed in both the (α+γ) and the (α_2 +γ) phase fields depending upon the temperature of transformation, cooling rate and the overall aluminum concentration of the alloy [23].

The precipitation of the γ phase from the α or α_2 phase most likely starts by the propagation of Shockley partial dislocations in the hexagonal matrix. This mechanism was initially proposed by Blackburn [119] and was confirmed by the presence of numerous stacking faults in the hexagonal matrix [86,95,96]. Blackburn explained the precipitation of the γ phase from the α_2 phase in an alloy of "eutectoid" composition (~40 at.% Al). Blackburn's mechanism has been extended to explain the precipitation of γ phase from the disordered α phase when the alloy is cooled from the α phase field to α+γ phase field [96]. It has been also suggested that the initiation process of the transformation involves the dissociation of a perfect a/3<11$\bar{2}$0> dislocation into two Shockley partials, a/3<10$\bar{1}$0> and a/3<01$\bar{1}$0>, bordering a stacking fault. Such a stacking fault is well known to locally create an fcc-type stacking sequence in the hexagonal matrix [120] thereby, facilitating nucleation of the γ-phase. Repeating this mechanism on every two basal planes of the hexagonal matrix brings the crystal structural change (hcp$\rightarrow$fcc) to completion. Also, since the close-packed planes and directions of hcp and fcc are parallel to each other, there is very little crystallographic mismatch and planar and highly coherent interfaces are formed. Denquin and Naka [96] have suggested that the

formation of a local fcc stacking sequence and the creation of highly coherent interfaces constitute a sort of pre-nucleation stage, strongly lowering the nucleation barrier to the precipitation of the γ phase. The γ-phase mainly nucleates at the stacking faults [96,120]. Moreover, grain boundaries are also suggested to serve as nucleation sites when they emit a/3<1100> type partial dislocations [86]. Application of suitable stress is suggested to enhance this process [86].

The nucleation and growth of γ lamellae involves both crystallographic and compositional changes. The crystallographic change involves ordering of the fcc type phase to ordered $L1_0$ γ-phase. The crystal structure change has been described in the preceding section. The ordering process has been dealt with in detail by Denquin *et al* [96]. It consists of a nucleation of orientation variants at a number of separate sites in the metastable fcc phase. This is then followed by an independent growth of these variants and their encounter with each other, resulting in the formation of order domain boundaries (ODBs) or anti-phase boundaries (APBs). It has been suggested that the kinetics of ordering of disordered fcc type phase to ordered $L1_0$ phase is very rapid as no disordered fcc phase has ever been observed to be present in the lamellar microstructure. Equilibrium aluminum concentration in the γ-phase is much higher as compared to that in the α_2-phase. The compositional changes thus involve transfer of aluminum atoms across the interface of the two phases from the hexagonal phase (α or α_2) to the precipitating γ-phase. Due to planar and coherent nature of the interfaces, transfer of atoms across the lamellar interfaces by classical long range diffusion is restricted. This was also corroborated by the absence of any concentration gradient around α_2/γ interfaces [106].

Accordingly, it has been suggested that the transfer of atoms across the interface most probably takes place by the "terrace-ledge-kink" mechanism [106]. Figure 2.15 is a schematic illustration of the formation of the γ plates. As can be seen in this figure, the growth of the γ plates proceeds by shear for plate lengthening and, by diffusion of atoms for plate thickening. Nonetheless, it has been suggested that the transformation is mostly dominated by shear [96,106].

2.3.2.2 Effect of composition and temperature on lamellar transformation: The Ti-Al phase (Figure 2.16) diagram shows three possible temperature ranges in which the transformation can take place [112]. If an alloy is quenched from the α single phase to α+γ two- phase field (alloy 1) above the eutectoid temperature and then aged isothermally, the microstructure is lamellar α+γ. On further cooling to room temperature α orders to α_2. Alternatively, when an alloy (2) is quenched from the α-phase field to a temperature below the α/α_2 order-disorder transformation temperature (T_o), α phase first orders to α_2 and then precipitation of γ takes place in α_2. But, when the α phase (alloy 3) is quenched to a region between the eutectoid temperature and the order-disorder transformation temperature, ordering of α phase does not take place without a change in its composition. According to Jones and Kaufman [23] "the pearlitic mode of transformation might be expected in this region". In this region, initially, the precipitation of γ would take place in disordered α and as the precipitation proceeds, the aluminum concentration of the matrix would decrease. When the matrix composition crosses the T_o line, ordering of α to α_2 phase would occur.

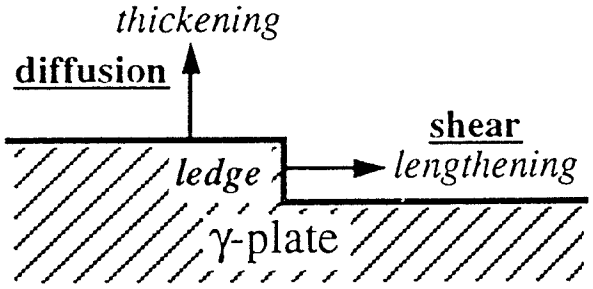

Figure 2.15: Schematic diagram showing growth of γ lamellae. [106]

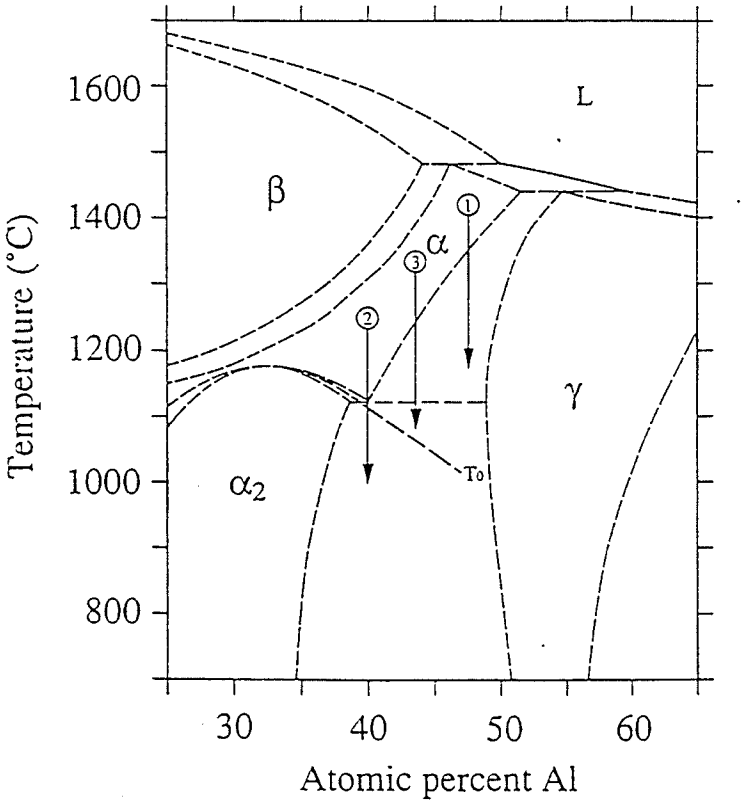

Figure 2.16: Central portion of the Ti-Al phase diagram. [112]

The cooling rate from the α phase field has been also found to have a significant effect on the decomposition of α phase and on the formation of α_2/γ lamellar microstructure. At higher cooling rates, α-phase first orders to α_2 and the γ phase precipitates in α_2 upon subsequent aging [86,106]. It has been also observed that higher cooling rates result in the formation of fine interlamellar spacing [106] with perfectly planar interfaces. On the other hand, slower cooling rates resulted in the formation of coarser lamellar structure with high density of partial dislocation ledges at α_2/γ interfaces suggesting the process to be diffusion controlled [23,96,106].

2.3.2.3 Effect of alloying elements on the formation of lamellar structure: Mn reduces the grain size and the interlamellar spacing, and at the same time promotes the formation of a lamellar microstructure [64]. Si and W are reported to stabilize the lamellar microstructure at higher temperatures [70,71]. Addition of very small amounts of B and W is documented to refine the fully lamellar microstructure and also make it more resistant to coarsening when exposed to high temperatures [121,122]

The alloys with fully lamellar microstructure exhibit the best creep properties, which is an important aspect to be considered while designing an alloy for high temperature structural applications. However, at the same time fully lamellar microstructures exhibit poor tensile properties. Reducing the grain size and interlamellar spacing enhances the tensile properties of fully lamellar microstructures. A reduction in the lamellar spacing also has beneficial effects on the fracture toughness of fully lamellar alloys. The existing knowledge of the effect of heat treatment variables on microstructural features of lamellar

microstructures can be utilized to design heat treatments for microstructural modifications in order to yield the desired properties for a specific application. A more detailed investigation is, however, required to completely understand the mechanism of various phase transformations and the effect of heat treatment variables on microstructural evolution, especially in the lamellar microstructure alloys.

2.3.3 Discontinuous Coarsening

Coarsening of the lamellar microstructure can take place either by discontinuous coarsening or by the formation of monolithic γ-grains [105], depending upon the alloy composition and the transformation temperature. In fully lamellar TiAl alloys, discontinuous coarsening is more pronounced and proceeds by the migration of a lamellar colony boundary leaving behind coarser α_2 and γ lamellae, and occurs at temperatures above 1173 K [99,101]. During discontinuous coarsening reaction, a two-phase microstructure with a high density of interfaces is transformed into a coarser lamellar microstructure by the migration of grain boundary of one grain into the neighboring grain at the expense of its fine lamellae. Discontinuous coarsening of primary lamellar microstructure occurs primarily behind the migrating grain boundary. Therefore, the resulting coarse secondary lamellae remain inside the initial grain of the primary lamellar microstructure. This process is assisted by grain boundary diffusion at the transformation front. The general consensus regarding the discontinuous coarsening is that the main driving force for it is the reduction in surface free energy. The residual chemical free energy of the primary reaction may also be considered to be a contributing factor [101]. Discontinuous coarsening is promoted by highly stable interfaces in the primary lamellar

structure which renders the normal lamellar coarsening of continuous type extremely difficult [105].

2.3.3.1 Morphological features: Discontinuous coarsening of primary lamellar microstructure is generally accompanied by the formation of serrated/interlocked lamellar grain boundaries. It was observed [105] that the coarsening occurred behind moving grain boundaries and that discontinuous coarsening developed on both sides of a given grain boundary. For much longer annealing times it was observed that discontinuous coarsening occupied a large part of the specimen. At higher temperatures, other coarsening mechanisms compete with discontinuous coarsening and more classical coarsening mechanisms become more pronounced.

Three types of morphology of the discontinuously coarsened lamellae have been identified during annealing of Ti-44Al alloy at 1000°C for different times (Figure 2.17) [101]: Type I – the lamellae have low energy habit plane as their interfaces and have the same lamellar direction as the original primary lamellae. Type II – the lamellae have the same crystallographic orientation of the α_2 plates as that observed in the original primary lamellae but have a different lamellar direction from the original primary lamellae and, have faceted lamellar interfaces. Type III – lamellae have a different lamellar orientation and a different crystallographic orientation of the α_2 plates from that in the original primary lamellae, but have a low energy habit plane as their lamellar interfaces. Discontinuous coarsening has also been observed in the near surface region of the specimens during annealing [100]. It was observed that discontinuous coarsening

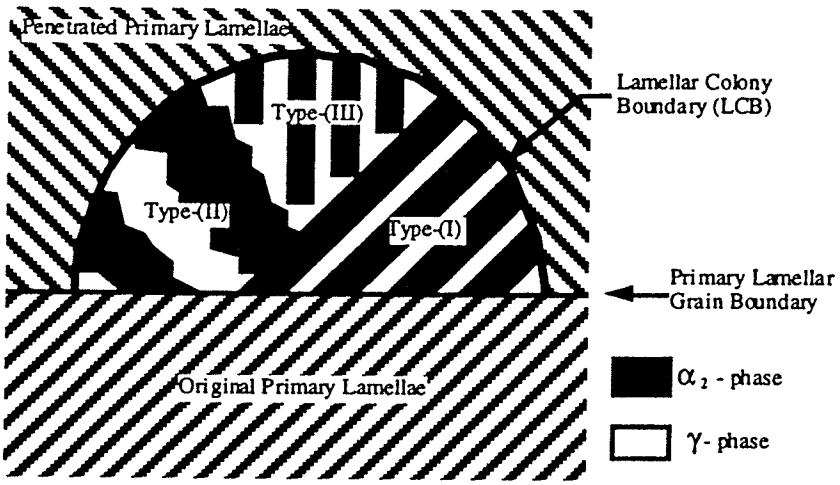

Figure 2.17: Schematic drawing of type I, II, and III lamellae in a single DC cell. [101]

randomly nucleated within the fine primary lamellae of the alloy surface and extended into a limited thickness of the surface layer when a Ti-42Al alloy was annealed at 1000°C. Qin *et al* [100] have suggested that the driving force for the discontinuous coarsening reaction in the surface layer is the elastic strain energy due to spark erosion and mechanical grinding, which was used to prepare the samples for heat treatment. Discontinuous coarsening near lamellar grain boundaries was also observed [98] when a Ti-44Al alloy was heated at 1050°C for relatively longer times. No coarsening was observed in the grain interior.

2.3.3.2 Mechanism of discontinuous coarsening: The primary lamellar microstructure is characterized by the presence of planar, extremely flat and highly coherent interfaces between the two constituent phases, α_2 and γ. Driving force for the thickening of these lamellae, during the growth stage, is provided by solute super-saturation. This thickening gradually slows down as super-saturation decreases and comes to completion/stop when the super-saturation is completely exhausted. Any further thickening of the lamellae can take place by coarsening, and the driving force for this coarsening would be the reduction of interfacial energy. However, it must be noted here that the highly coherent nature of the lamellar interfaces makes the transfer of solute atoms across the interfaces extremely difficult and hence, normal coarsening cannot take place. The coarsening thus occurs by a discontinuous reaction that involves a reduction in the interfacial energy by coarsening of the lamellae behind the moving grain boundary. Although the main driving force for the discontinuous coarsening reaction is considered to be the reduction in surface energy, the residual chemical free energy of the primary reaction may also be a contributing factor.

During discontinuous coarsening, the grain boundaries tend to become curved/undulated, whereas the grain size remains almost unchanged. This leads to an increase in total grain boundary area and hence the energy. Denquin and Naka [105] have suggested that this increase in the total energy could be compensated by a decrease in lamellar interfacial energy through the formation of a coarser lamellar microstructure. They have also proposed that the reduction in interfacial energy is the main driving force for discontinuous coarsening. They also observed that in the secondary lamellar microstructure, formed by discontinuous coarsening, α_2 and γ phases had the same crystallographic orientation relationship but the interfaces were much more irregular. Based on these observations, they suggest a different mechanism for the formation of secondary lamellae which does not involve movement of stacking faults. The detailed mechanism for the formation of secondary lamellar microstructure by discontinuous coarsening has been not yet documented. Though a great deal of research has been conducted on discontinuous coarsening, the mechanism of the reaction has received very little attention.

A diffusion model for the discontinuous coarsening reaction was developed by Livingston and Cahn [101,123]. In this theory, the underlying theory assumes that: (1) both fine and coarse lamellae are normal to a planar grain boundary; (2) the coarsening rate is controlled by grain boundary diffusion; and (3) the driving force for the reaction is the difference in the interfacial energy. This model has been used by Mitao and Bendersky [101] in their analysis of the kinetics of the discontinuous coarsening reaction.

The growth kinetics of the three types of secondary lamellar morphology was theoretically analyzed taking into account the misorientation between the penetrated and the primary lamellae.

2.3.4 The $\alpha \rightarrow \gamma_m$ Massive Transformation

The massive transformation takes place by a diffusion based nucleation and thermally activated growth without any change in composition. It is mainly caused by the diffusion of atoms (transfer of atoms) across the product/parent interphase interfaces. These interfaces are generally presumed to have a disordered structure and there is no specific low index orientation relationship between the transformed product phase and the parent phase.

The massive type transformation was first observed in the Ti-Al system by Wang *et al* in 1992 [104]. They reported the formation of massive γ-phase (γ_m) in a Ti-48 Al alloy when the alloy was cooled from the α-phase field at cooling rates sufficiently high to suppress the formation of lamellar ($\alpha_2+\gamma$) microstructure. Since then, this transformation has been reported in a number of TiAl-based alloys [103-117] and attempts have been made to enhance the understanding of the kinetics, thermodynamics and mechanism of the massive transformation as applied to the Ti-Al system. Attempts have also been made to establish the effect of various processing parameters on the transformation. Several aspects of the $\alpha \rightarrow \gamma_m$ massive type transformation are however, still not fully comprehended, specifically, reaction start temperatures for different cooling rates, driving force for the transformation, nucleation and growth kinetics and their mechanisms

2.3.4.1 Kinetics and Thermodynamics of massive transformation: In order to precisely elucidate the mechanism of massive transformation in the Ti-Al system it is important to have a sound understanding of the kinetics and thermodynamics of the transformation. Vasudevan's research group, at the University of Cincinnati, has made an effort to highlight these features of the massive transformation. In one of their most recent publications [116], they have reported the cooling rate dependence of reaction start temperature, and analyzed the growth kinetics and thermodynamics of the transformation based on the electrical resistivity measurements during continuous cooling experiments in a Ti-47.5Al alloy. They have also proposed a CCT diagram for the alloy used in their study (Figure 2.18). The average growth rate of massive γ_m was estimated to be $\sim 0.14 \times 10^{-2}$ m/s at the transformation temperature of 1120°C and an undercooling of 210°C. It was observed to decrease to $\sim 0.07 \times 10^{-2}$ m/s at the transformation temperature of 1024°C and undercooling of ~310°C. The estimation of growth rate involved the duration of thermal arrest and the size of γ_m nodule, the latter being dependent on the alloy composition and cooling rate. Therefore, the growth rate would depend on the overall composition of the alloy.

Thermodynamic analysis of the massive transformation in Ti-47.5Al alloy has yielded a value of ~-3712 J/mole for the enthalpy and ~ -535 J/mole for the free energy change of the reaction. However, it is important to mention here that the free energy of the α and γ phases varies with the composition of the alloy, as proposed by Zhang *et al.* [124]. It is therefore, not unreasonable to state that the driving force for massive transformation will

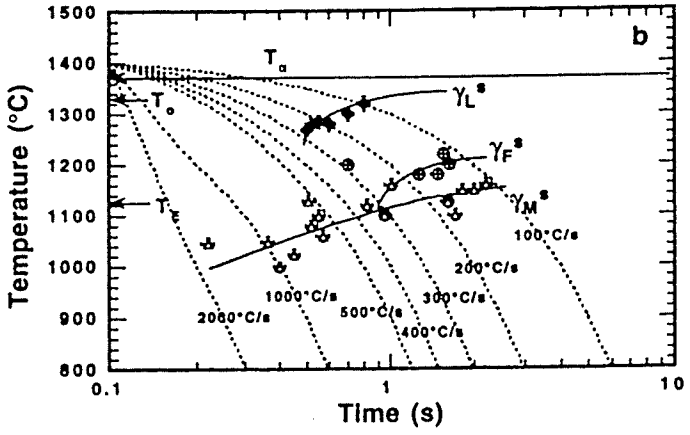

Figure 2.18: CCT diagram for Ti-47.5Al alloy. [116]

depend on the alloy composition. Further, the calculation of enthalpy involves the fraction of the transformation product and the temperature of transformation (undercooling), which in turn depend on cooling rate and also the composition of the alloy. Similar analyses are thus required for a range of compositions to completely understand the kinetics and thermodynamics of the massive transformation in the Ti-Al system. Veeraraghvan *et al.* [116] have also proposed that $\alpha \rightarrow \gamma_m$ massive transformation is controlled by interfacial diffusion rather than bulk diffusion based on the premise that the activation energy for interface diffusion is 0.58 times of that for the bulk diffusion.

2.3.4.2 Mechanism of Massive Transformation: The Massive Transformation is a complex reaction. Though this transformation has been observed in a number of alloy systems, the mechanism of the nucleation and growth of massively transformed product is still not completely understood and is a subject of too many controversies. The mechanism of massive transformation in the Ti-Al system has been intensively investigated by Denquin *et al.* [105], Zhang *et al.* [110,113], Wang *et al.* [115] and Veeraraghavan *et al.* [116]. However, it is not yet precisely defined. Denquin *et al* were the first to analyze the nucleation and growth mechanisms of the formation of γ_m from α-phase based on the experimental results obtained during heat treatment of a Ti-48Al binary alloy. They proposed that grain boundaries act as preferential nucleation sites for the nucleation of massive γ. The absence of Blackburn's orientation relationship between the parent α-phase and the product γ_m phase eliminates the possibility of γ_m phase nucleating at stacking faults of the hexagonal matrix as is the case in lamellar transformation. According to Perepezko [125] and Massalski [126], the growth of the

massive product may be achieved by either of the following two methods: (1) short range jump of atoms across an incoherent interface resulting in a curved interface, or (2) the ledge mechanism resulting in the formation of planar interface. Generally, in Ti-Al system α/γ_m interfaces are a combination of these two types and therefore, growth of nucleated γ_m can proceed by any of the two mechanisms. Nonetheless, Denquin *et al.* have suggested that "the growth mechanism of γ_m phase involves thermally activated jumps of individual atoms across an incoherent interface" because the interfaces observed in their investigation were generally irregular and curved [105]. However, it has been recently shown by Nie *et al.* [127] that even in the absence of any low index orientation relationship, the interfaces can be partially coherent rather than incoherent. On the other hand, Lin *et al.* [128] have reported a completely coherent interface preserving the perfect orientation relationship, i.e., $(111)_{\gamma m}//(0001)_\alpha$ and $[110]_{\gamma m}//[11\bar{2}0]_\alpha$ and hence, have suggested a ledge mechanism for the growth of γ_m.

It is worth mentioning here again that the whole process of massive transformation involves formation of an ordered, $L1_0$, γ_m phase from a disordered hexagonal α-phase. Denquin *et al* [105] proposed two possible mechanisms: direct $\alpha \rightarrow \gamma_m$ transition or $\alpha \rightarrow$ fcc-type phase $\rightarrow \gamma_m$. It is well known that the massive transformation takes place at relatively high cooling rates (e.g. water quenching), and as mentioned earlier, γ_m is an ordered tetragonal phase that forms from a disordered hexagonal phase, α, during the transformation. Also, the experimentally observed presence of stacking faults (SFs) and anti phase boundaries (APBs) cannot be explained if the first mechanism of transformation was operational. Later, Zhang *et al* [113] proposed a mechanism that

involved the formation of an intermediate disordered fcc-type phase prior to the formation of the final massive γ_m phase. According to their proposed mechanism, γ_m develops from γ lamellae that have intersected a nearby grain boundary and spread into the adjacent grain. The growing γ_m stops only if it intersects a transformed region or a grain boundary. This growth mechanism leads to the formation of γ_m possessing the same orientation relationship as that of the lamellar γ phase in the grain in which the lamellae formed. This mechanism, however, fails to explain the formation of γ_m phase that occurs without any prior decomposition of the α phase to form lamellar microstructure and when the competing phase transformation is the $\alpha \rightarrow \alpha_2$ ordering reaction.

Wang *et al.* [115] analyzed the formation of defect structures (SFs and APBs) in γ_m phase. APBs were also observed to be attached to the 1/6[211] and 1/6[12$\bar{1}$] Shockley partials bounding the SF formed by the dissociation of a ½[110] unit dislocation. The dissociation of unit dislocation into two widely separated partial dislocations with SF in between has been deduced to have formed in the disordered fcc phase because of the high SF energy of the ordered γ-phase. SFs formed in the disordered fcc phase would become high energy upon ordering. They will then have a tendency to reduce their energy by attracting the APBs that exist in the vicinity after the ordering reaction. Based on their observations and analysis, Wang *et al* proposed a mechanism that involves the formation of an intermediate disordered fcc phase during the $\alpha \rightarrow \gamma_m$ phase transformation.

Thus, it is noted that to-date no consensus exists regarding the mechanism of massive transformation in Ti-Al system. Efforts are ongoing to understand the mechanism involved in the massive type transformation.

2.3.4.3 Effect of Cooling Rate: Massive transformation normally requires a relatively high cooling rate [103-105,109, 125,126], and a complete transformation of hexagonal α-phase to ordered $L1_0$ γ_m phase requires a critical cooling rate (minimum undercooling). The critical cooling rate of the transformation is, however dependent on the aluminum concentration of the alloy, with a less severe cooling rate being required as the aluminum concentration of the alloy increases. The cooling rate also affects the morphology and amount of the transformed product phase [103]. In the composition range of 46.5-48 at.% Al, it has been observed that at low cooling rates the microstructure mainly consists of patches of γ_m in a background of lamellar grains. Increasing the cooling rate increases the amount of γ_m, and at sufficiently high cooling rate (when optimum undercooling rate is achieved) the structure is completely γ_m. At still higher cooling rates massive transformation is suppressed by $\alpha \rightarrow \alpha_2$ ordering reaction. This results in a decrease in the amount of transformed γ_m and an increase in α_2 with increasing cooling rate. Increase in cooling rate is also reported to cause a decrease in the rate of massive transformation [116].

2.3.4.4 Effect of Aluminum and Other Alloying Element Concentration: In the binary Ti-Al system, massive transformation has been observed in alloys with aluminum concentration higher than 45 at.%. It has been also suggested [23,105] that massive

transformation occurs if the alloy composition is close to the equilibrium aluminum concentration of the γ-phase. Higher overall concentration of Al in the alloy produces a microstructure consisting of γ_m and lamellar, whereas a lower Al concentration produces a microstructure consisting of γ_m and α_2 phases. According to Jones and Kaufman massive transformation cannot be obtained in binary Ti-45Al alloy. However, in the presence of small amounts of alloying elements such as Mn and Nb, massive transformation has been observed in Ti-45Al based alloys [108,109].

2.4. PROCESSING / MICROSTRUCTURAL CONTROL AND MECHANICAL PROPERTIES

The γ-based alloys are processed by casting, ingot metallurgy, powder metallurgy and sheet forming methods. The cast microstructures in the alloys produced by casting process are normally fully lamellar with occasional shrinkage pores and a small amount of pro-eutectoid γ phase. Hot isostatic pressing (HIP'ing) is employed to remove the porosity. The ingot metallurgy process starts with ingot casting, followed by HIP'ing and/or a homogenization treatment and then hot working. HIP'ing removes shrinkage pores and also begins to homogenize the as-cast microstructures. Hot working is conducted near the eutectoid temperature in the case of forging or at higher temperatures for extrusion. Forging generally results in a banded microstructure consisting of a fine, partially recrystallized γ-grain matrix, dispersed with fine α_2 particles and some original lamellar grains which have survived hot deformation [14]. Extrusion at temperatures near

the eutectoid temperature results in microstructures similar to, but less homogeneous than those produced by forging. Extrusion at higher temperature, where volume fractions of α and γ phases are almost equal, results in a fine duplex microstructure. Under certain conditions, high temperature extrusion yields fine randomly oriented fully lamellar grains with serrated boundaries.

The processed products are heat-treated under appropriate conditions to develop the desired properties. The post processing heat treatments can be grouped into three schemes: I, II and III (Figure 2.19) [5,14]. Schemes I and II consist of annealing treatments and subsequent aging treatments. Scheme III consists of aging treatment only. The two step heat treatments, scheme I and II are used for hot worked materials which have microstructure other than the fully lamellar microstructure. Scheme III heat treatments are used when the as processed microstructures are not to be altered or are stable, as in the case of fully lamellar microstructures. Several thermomechanical treatments have been identified to alter the microstructure of γ-based alloys by forging, extrusion or rolling followed by appropriate heat treatments [14,17,129-133]. All of these treatments result in refinement of the microstructure due to recrystallization. The volume fraction of different phases in the microstructure, however, varies depending upon the composition of the alloy, and temperature and time of heat treatment.

The mechanical properties of γ-based alloys are sensitive to the relative proportion of the constituent phases, α_2 and γ, in the microstructure. Figure 2.20 [11,34] schematically shows the variation of mechanical properties with microstructure. The fully lamellar

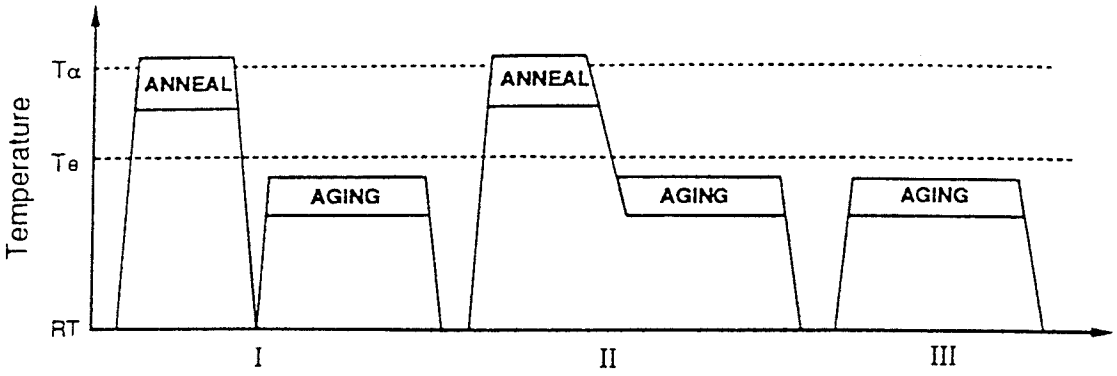

Figure 2.19: Three typical heat treatment schemes for gamma titanium aluminide alloys. All three can be used for wrought alloys, whereas cast products may need the scheme III treatment only. [5,14]

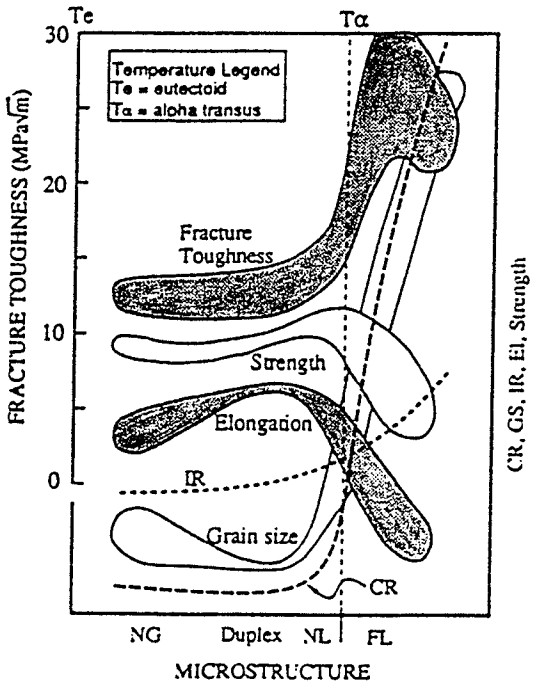

Figure 2.20: Schematic relationship between microstructure and grain size and mechanical properties, including fracture toughness, tensile strength and elongation (El), impact resistance (IR) and creep resistance (CR). [11,34]

microstructure exhibits low strength as compared to the duplex microstructure. However, it has better high temperature strength retention properties. On the contrary, the fully lamellar microstructure consisting of coarse lamellar grains produces improved fracture toughness and creep resistance but poor tensile properties. The fully lamellar structure also has poor room temperature ductility. The strength and ductility can be improved by reducing the amount of α_2-phase in the microstructure.

The tensile properties of the lamellar alloys are sensitive to lamellar grain size. With a decrease in grain size the strength and ductility exhibit an increasing trend (Figure 2.21) [15]. The yield strength and grain size of fully lamellar structure have been observed to obey the Hall-Petch relationship with a k_y value of ~4.5 MPa$(m)^{1/2}$ [17]. This relationship was later modified for a wide range of grain size versus gage diameter ratio and the value of $k_y \sim 2$ MPa$(m)^{1/2}$ was obtained for grain sizes varying from 230 – 2600 μm and interlamellar spacing of 1.5 – 0.3 μm, and yield strengths varying from 380 – 500 MPa [17,134]. The fully lamellar microstructure generally exhibits poor room temperature ductility with the ductility varying from 2 to 0.2 % as grain size increases from 250 to 2600 μm [17,135,136]. The tensile properties can thus be improved by reducing the lamellar grain size. The addition of boron or very small amounts of TiB_2 by XD technology can significantly refine the grain size [65-67, 137, 138]. It has also been found that extruding near the α-transus temperature can result in a fine-grained microstructure [139]. Recently, Wang and Xie [140] have reported a rapid heat treatment technique by which a Ti-48Al-2Cr alloy, with a coarse fully lamellar structure of ~500 μm grain size was refined to a fine one of ~10 μm. This resulted in a significant increase

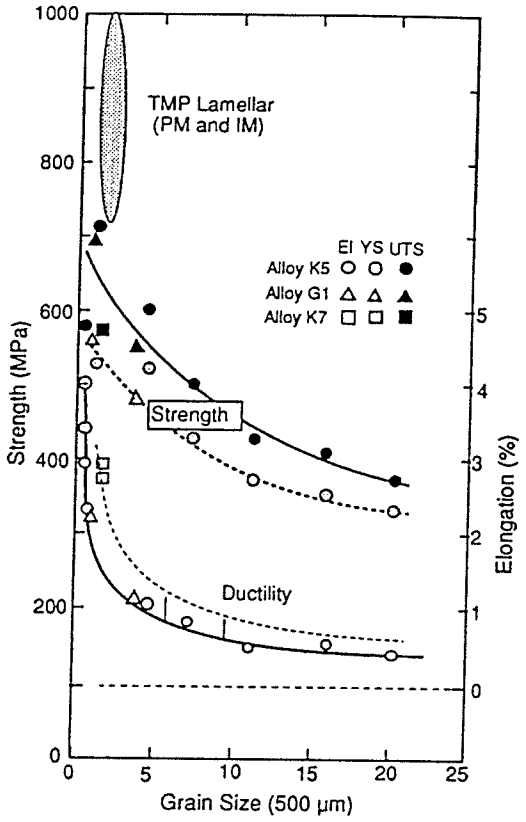

Figure 2.21: Effect of microstructure on room-temperature tensile properties in gamma alloys. [15]

in room-temperature yield strength, RT ductility and fracture strength. Several other methods have also been reported to significantly refine the grain size by two step heat treatments [141-144]. Time and temperature of heat treatment have also been reported to affect the microstructural development during a heat treatment. Higher temperatures and longer times of heat treatment result in coarse-grained microstructure. While grain refinement results in improved tensile properties, it has deleterious effect on the fracture toughness and creep resistance. However, the grain size effect on these properties is not very well established.

In addition to the decrease in lamellar grain size, a reduction in interlamellar spacing is also beneficial to the tensile properties, especially yield strength, of fully lamellar γ-based alloys (Figure 2.22) [122]. The value of Hall-Petch constant, ky, was observed to vary with the interlamellar spacing. It was ~2.5 $MPa(m)^{1/2}$ for the ultra fine lamellar microstructure and ~1 $MPa(m)^{1/2}$ for the coarse lamellar microstructure (Figure 2.23) [12]. The yield strength of alloys with lamellar microstructure was thus observed to increase with a decrease in interlamellar spacing with the strength exceeding that of the duplex microstructure for ultra fine lamellar microstructure. Interlamellar spacing of fully lamellar microstructure also affects the fracture toughness and creep properties. Fracture toughness of the lamellar alloy has been observed to increase considerably by decreasing the interlamellar spacing in the materials with grain sizes larger than the plastic zone size [134,145]. However, when the grain size is smaller than the plastic zone size, the effect of lamellar spacing becomes less significant. A reduction in interlamellar spacing also improves the creep resistance of the alloy with a fully lamellar microstructure. It has been

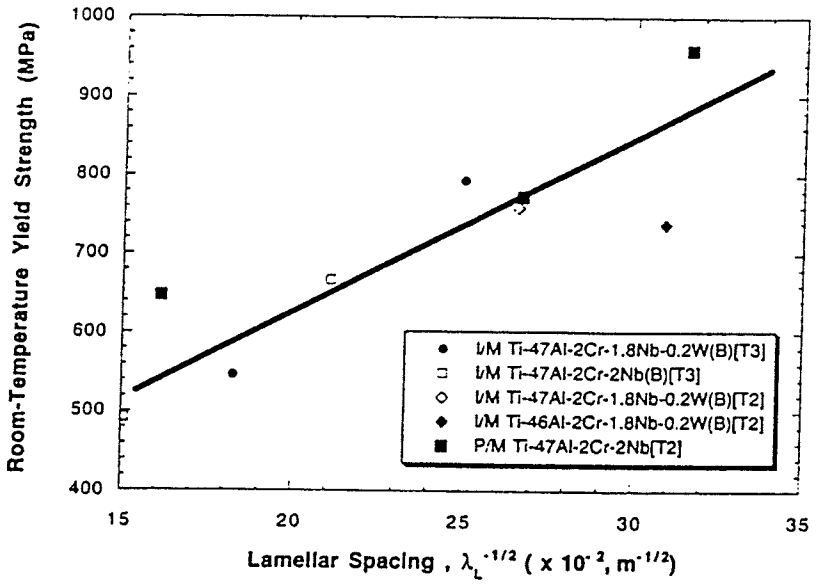

Figure 2.22: Effect of lamellar spacing on yield strength. [122]

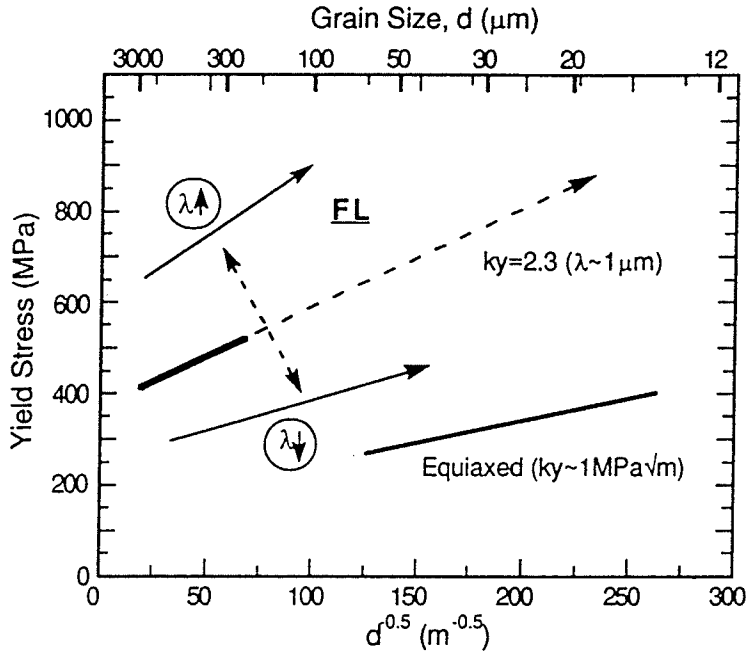

Figure 2.23: Relationship between grain size and yield strength in fully lamellar (FL) materials, showing the HP constant for FL material may vary from 1 MPa$(m)^{1/2}$ to > 2 MPa$(m)^{1/2}$ with decrease in lamellar spacing. [12]

suggested that the α_2 plates act as reinforcement in the lamellar microstructure resulting in the formation of a composite like structure that improves the creep resistance of the alloy [146]. The nature of lamellar interface also affects the creep properties of the lamellar alloy with better creep properties being exhibited by lamellar microstructures having planar interfaces.

The lamellar spacing and nature of the lamellar interfaces can be controlled by controlling the cooling rate from the α-phase field. High cooling rates result in ordering of α to α_2 and subsequent precipitation of fine γ lamellae [86,146], thus refining the interlamellar spacing of the lamellar microstructure. The lamellar interfaces formed under such conditions are planar. On the other hand, slower cooling result in the formation of coarse lamellar microstructure with irregular lamellar interface [105,146]. The prior α grain size is also believed to have an influence on cooling rate dependence of the microstructure. Application of a certain amount of stress during rapid cooling from the α-phase field can also enhance the formation of fine lamellar microstructure. C.T.Liu *et al* [139,147] have reported that in a Ti-47Al-2Cr-2Nb alloy, a unique refined colony/ ultra fine lamellar microstructure was produced by extruding it above the α-transus temperature. Very high cooling rates from the α-phase field result in suppression of the lamellar transformation either by $\alpha \rightarrow \alpha_2$ ordering reaction or by $\alpha \rightarrow \gamma_m$ massive type reaction, depending upon the alloy composition [23,105]. In the latter case, isothermal aging of the massive γ in the $\alpha_2+\gamma$ phase field results in the precipitation of α_2 plates and/or α_2 particles in γ matrix as well as at γ grain boundaries [141-144]. A more detailed

study is, however, required to fully explore the potential of massive transformation in refinement of the lamellar microstructure.

Beddoes *et al.* [148] reported that heat treatment for short times, in the α-phase field, results in the formation of serrated grain boundaries whereas longer times result in planar grain boundaries. Discontinuous coarsening and formation of serrated grain boundaries has been also reported elsewhere [101,102,105]. However, a more detailed investigation is required to better understand the mechanism of discontinuous coarsening and formation of serrated grain boundaries. Serrated or interlocked grain boundaries are believed to enhance creep rupture life and fracture resistance of an alloy with a fully lamellar microstructure [75,149,150]. Effect of grain boundary morphology on other mechanical properties has been not yet documented.

TiAl based titanium aluminides are structural materials that are being developed for use at high temperatures. It is thus very important to design an alloy that has reasonably good creep properties and whose microstructure is stable when exposed to high temperatures for prolonged time periods. As discussed in section 2.2.2, addition of Si, W, Ta and/or B stabilize the lamellar structure, which in turn enhances the creep resistance.

The mechanical properties of the lamellar microstructure are also extremely sensitive to lamellar orientation. The yield strength and elongation are strongly dependent on the angle between the lamellar boundaries and the loading axis. The yield strength is high when the lamellar boundaries are parallel or perpendicular to the loading axis, but is low

for intermediate orientations. The fracture toughness of lamellar microstructure also depends on the orientation of the lamellae relative to the crack plane. Highest toughness values were obtained when the crack was forced to traverse across the lamellar interfaces than when the crack growth was along the lamellar interfaces. Thus it appears that preferential lamellar orientation is beneficial for some specific applications. The lamellar microstructure with preferential orientation of the lamellae can be produced by directional solidification processing [151] and by thermo-mechanical treatments [14,15]

In summary, fully lamellar γ-based alloys are the most promising alloys for high temperature structural applications. They provide a promising avenue for microstructural control. By varying the temperature of transformation and cooling rate, and the amount of alloying elements, the microstructural features of the lamellar microstructure such as grain size, grain boundary morphology, lamellar spacing and the nature of lamellar interface can be considerably altered. Hence the mechanical properties can also be modified/improved. Also since the alloys of engineering importance contain ternary and quaternary alloying elements, it is important to investigate and establish the effect of alloying elements on phase transformations and microstructural response of the TiAl based alloys to various heat treatments. Though many attempts have been made to modify the microstructure of γ-based titanium aluminides, each attempt is limited to a specific property. The microstructural evolution and its optimization for obtaining balanced properties demands meticulous investigation in order to design an alloy with desired properties for specific applications.

2.5 SCOPE AND OBJECTIVES OF THE PRESENT INVESTIGATION

As discussed in the preceding sections of the literature review, the mechanical properties of γ-based titanium aluminides are a strong function of microstructure. A good balance of the mechanical properties can be achieved by carefully tailoring the microstructure. However, in order to obtain desired microstructure and properties, one needs to have a comprehensive understanding of the phase transformations that take place in the Ti-Al system. Numerous researches have been conducted to understand the binary phase equilibria. Various phase transformations have also been identified in the binary Ti-Al system and their tentative mechanisms have been proposed. However, there is a dearth of information regarding the phase transformations in the ternary and quaternary alloy systems. The addition of third and fourth alloying elements to the Ti-Al binary system brings new phases into existence and, also changes the relative stability of the equilibrium phases, thus, modifying the transformation modes. Hence, a more comprehensive and meticulous investigation of the effect of these alloying elements and various other parameters such as stress, temperature, and heating and cooling rate on phase transformations and microstructural evolution is required. Keeping this background in view, the objectives of this research were to:

1. Qualitatively study the effect of alloying elements, such as Nb and Mn, on phase transformations in γ-based titanium aluminide alloys.
2. Study the effect of cooling rate on microstructural evolution in TiAl-based alloys with varying compositions.

3. Explore the transformation paths, by innovative heat treatments, for optimizing the microstructure so as to achieve a balance between the mechanical properties.

The binary alloy used in this study had a nominal composition of Ti-45 at.% Al. The other ternary and quaternary alloying elements were Nb and Mn in varying proportions. Nb concentration in the ternary and quaternary alloys was constant whereas, Mn concentration was varied from 0.4 to 2 at.%. The effect of cooling rate induced by water quenching, oil quenching, air cooling, and furnace cooling from 1350°C in the alpha phase field on microstructural evolution in various Ti-45Al based alloys was studied. The effect of environment during heating at 1350°C was also established.

Chapter 3

EXPERIMENTAL PROCEDURE

3.1 MATERIALS

This study involved four TiAl based alloys, namely Ti-45Al (alloy I), Ti-45Al-2Nb (alloy II), Ti-45Al-2Nb-0.4Mn (alloy III), and Ti-45Al-2Nb-2Mn (alloy IV) (all compositions in at.%). Ti-45Al and Ti-45Al-2Nb alloys were prepared at the University of Birmingham, UK and supplied in the form of ~ 1kg buttons. Ti-45Al-2Nb-0.4Mn and Ti-45Al-2Nb-2Mn alloys were supplied by Howmet Corporation, USA, in the form of 10-12 mm thick slabs. The alloys were prepared by plasma arc melting process and were hot isostatically pressed (HIPped) for 4 hours at 1275°C and 172 MPa pressure. The measured chemical compositions of the four alloys are given in Table 3.1. Figure 3.1 shows a binary Ti-Al phase diagram. The composition marked in the diagram corresponds to the Al concentration of the alloys used in this investigation. Table 3.2 lists the hardness values of the as-received alloys.

3.2 SPECIMEN PREPARATION AND HEAT TREATMENTS

Specimens of 12mm x 6mm x 6mm size were cut by electro-discharge machining (EDM) from the buttons of alloys I and II and from slabs of alloys III and IV for various heat treatments. These specimens were cleaned with alcohol in an ultrasonic cleaning bath and then encapsulated in vycor capsules that were evacuated to 10^{-6} torr and subsequently back-filled with argon. The encapsulated specimens were heat treated at 1350°C (α-phase

Table 3.1. Nominal and actual measured compositions of the alloys.

Alloys	Compositions, at.%							
	Al		Nb		Mn		Ti	oxygen, ppm
	nominal	actual	nominal	actual	nominal	actual		
Alloy I	45	45.5	-	-	-	-	balance	450
Alloy II	45	45.2	2	1.85	-	-	balance	550
Alloy III	45	44.9	2	2.15	0.4	0.4	balance	510
Alloy IV	45	45.16	2	2.06	2	1.72	balance	650

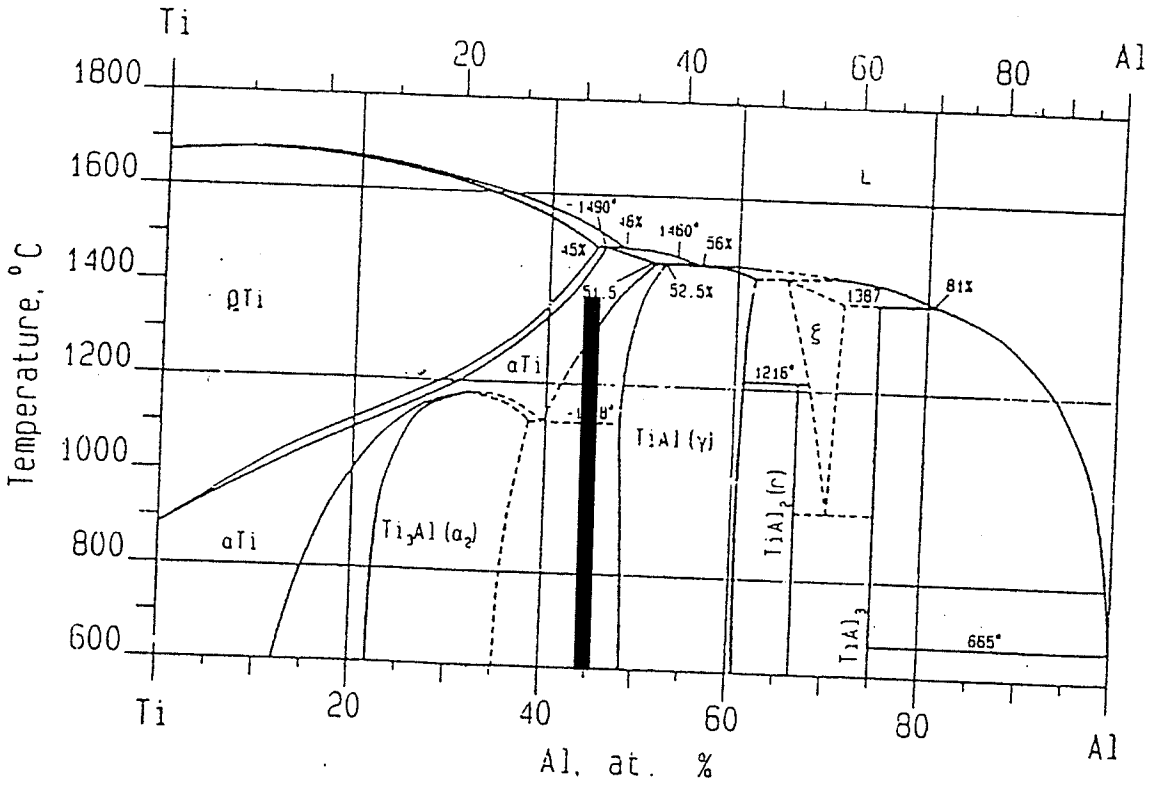

Figure 3.1: Binary Ti-Al phase diagram. The composition marked corresponds to the Al concentration of the alloys used in this study.

Table 3.2 Hardness of the as-received alloys

Alloys	Hardness, (VPH)
Alloy I	300
Alloy II	315
Alloy III	280
Alloy IV	302

field) in a box furnace for various time periods. Subsequently, the samples were cooled at various cooling rates, namely, furnace cooling (FC), air-cooling (AC), oil quenching (OQ), and water quenching (WQ). For investigating the effect of grain size on phase transformations (lamellar and massive), the samples were wrapped in Ta-foils before sealing them in vycor capsules. The sealed samples were heat treated at 1350°C for various time periods ranging from 15 minutes to 4 hours and subsequently furnace cooled and ice water quenched. The details of all the heat treatments are given in Table 3.3.

***Measurement of cooling rates*:** Samples of 12mm x 6mm x 6mm size were used for quantification of cooling rates. A Pt/Pt-13%Rh (type R) thermocouple was spot welded to the samples. The thermocouple wires were 0.01 inch (0.25 mm) in diameter. Since the thermocouple reacts with aluminide, a 2mm x 2mm piece of 0.005 inch (~0.127 mm) thick Ta foil was first spot welded to the sample and then the fused thermocouple bead was spot welded on to the foil. The samples were then placed in a furnace maintained at 1350°C, held for 3-5 minutes to homogenize the temperature and then cooled to room temperature in air, oil and water. It was assumed that the small piece of Ta-foil and the sample cool at same rate during cooling from 1350°C.

The cold junction of the thermocouple was connected to a National Instruments AT-MIO-16 data acquisition board, through a linearizing circuit for type-R thermocouple, provided by Analog Devices. The linearizing circuit was capable of amplifying and linearizing the millivolts signal of the thermocouple and give a linear output in the range of 0-5 VDC over the temperature range of 500 – 1750°C. The linearized output was

Table 3.3: Details of heat treatment schemes

Alloy	Temperature (°C)	Time (min)	Cooling Rate
Ti-45Al (alloy I)	1350 (without Ta-wrapping)	30	FC, AC, OQ, WQ
Ti-45Al-2Nb (alloy II)	1350 (without Ta-wrapping)	30	FC, AC, OQ, WQ
	1350 (with Ta-wrapping)	15 30 60 90 120 150 240	FC FC FC FC FC FC FC
Ti-45Al-2Nb-0.4Mn (alloy III)	1350 (without Ta-wrapping)	30	FC, AC, OQ, WQ
	1350 (with Ta-wrapping)	15 30 60 90 120 150 240	FC FC and IWQ FC FC and IWQ FC FC and IWQ FC
Ti-45Al-2Nb-2Mn (alloy IV)	1350 (without Ta-wrapping)	30	FC, AC, OQ, WQ

acquired and interpreted using a data acquisition software and, stored and analyzed in a Pentium 133 MHz PC. Figure 3.2 shows a schematic block diagram of the setup used for measuring the cooling rates. The temperature data were plotted against time and the cooing rates were determined as the slope of the best-fit line over the temperature range of 1250 to 800°C. The measured cooling rates are given in Table 3.4. These values of cooling rates were also corroborated using a chart recorder.

3.3 OPTICAL AND SCANNING ELECTRON MICROSCOPY

The heat-treated specimens were sectioned by EDM as shown in Figure 3.3 for examination by scanning electron microscopy (SEM) and by optical metallography. The samples for optical metallography were prepared by standard metallography technique and the etchant used was a modified Kroll's reagent (7% HF, 21% HNO_3 and 72% H_2O). ZEISS Axiovert 25 CA inverted reflected-light microscope equipped with CLEMEX vision^{TM} 3.0 image analysis system was used for qualitative and quantitative optical metallography. JEOL 840 equipped with NORAN energy dispersive spectrometer (EDS), and JSM-5900LV scanning electron microscope, equipped with an OXFORD energy dispersive spectrometer (EDS) and Inca analytical software were used for the examination of the polished cross-section samples.

3.3.1 Grain size measurement

Lamellar grain size (colony size) in the samples was measured by using the CLEMEX vision image analysis software. The lamellar structure consisted of alternating dark and white phase platelets and the software was unable/incapable of distinguishing the grain

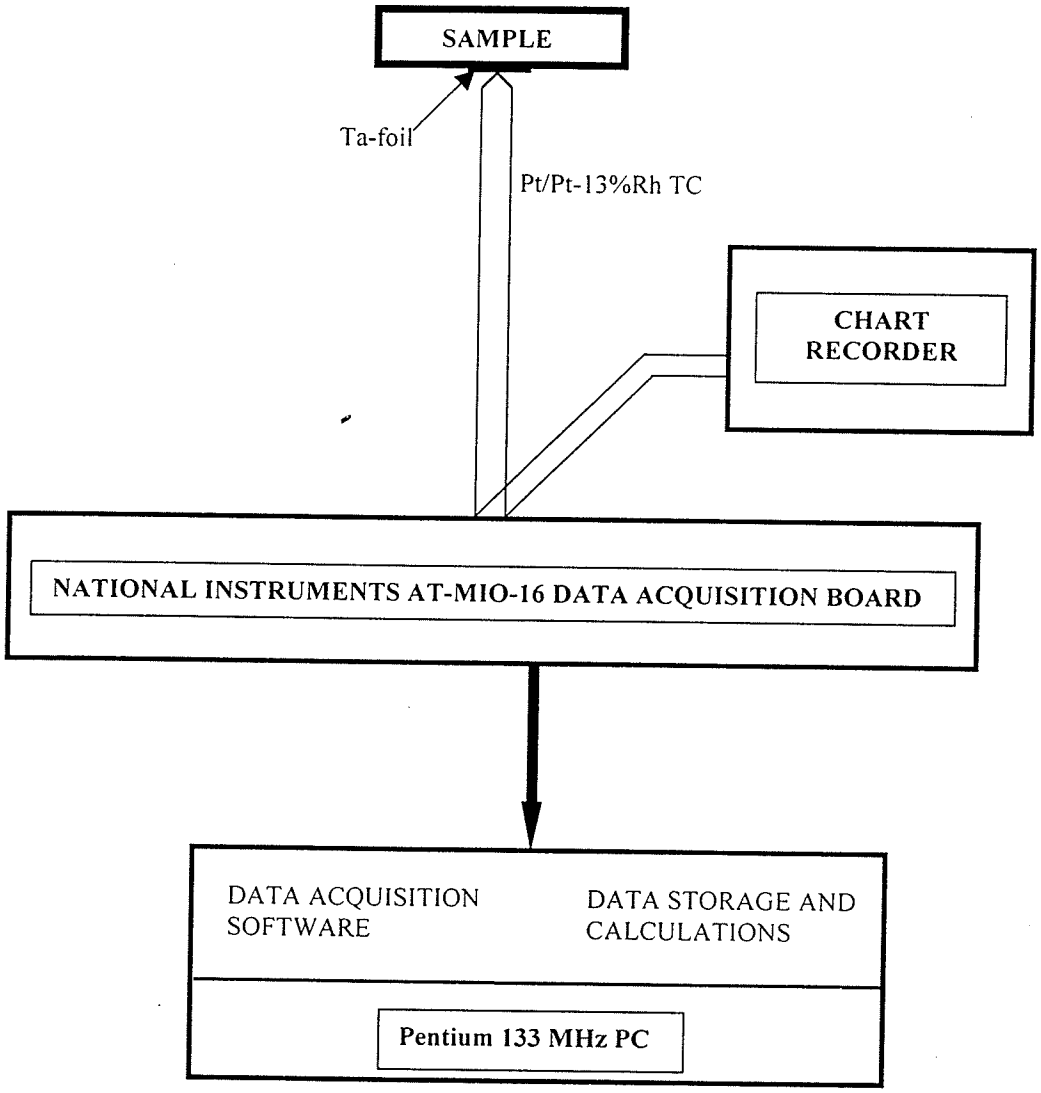

Figure 3.2: Block diagram of the experimental setup used to measure cooling rates

Table 3.4 Measured values of cooling rates

Water quenching ~ 1000 °C/sec
Oil quenching ~ 155 °C/sec
Air cooling ~ 25 °C/sec
Furnace cooling ~ 2 – 3 °C/min

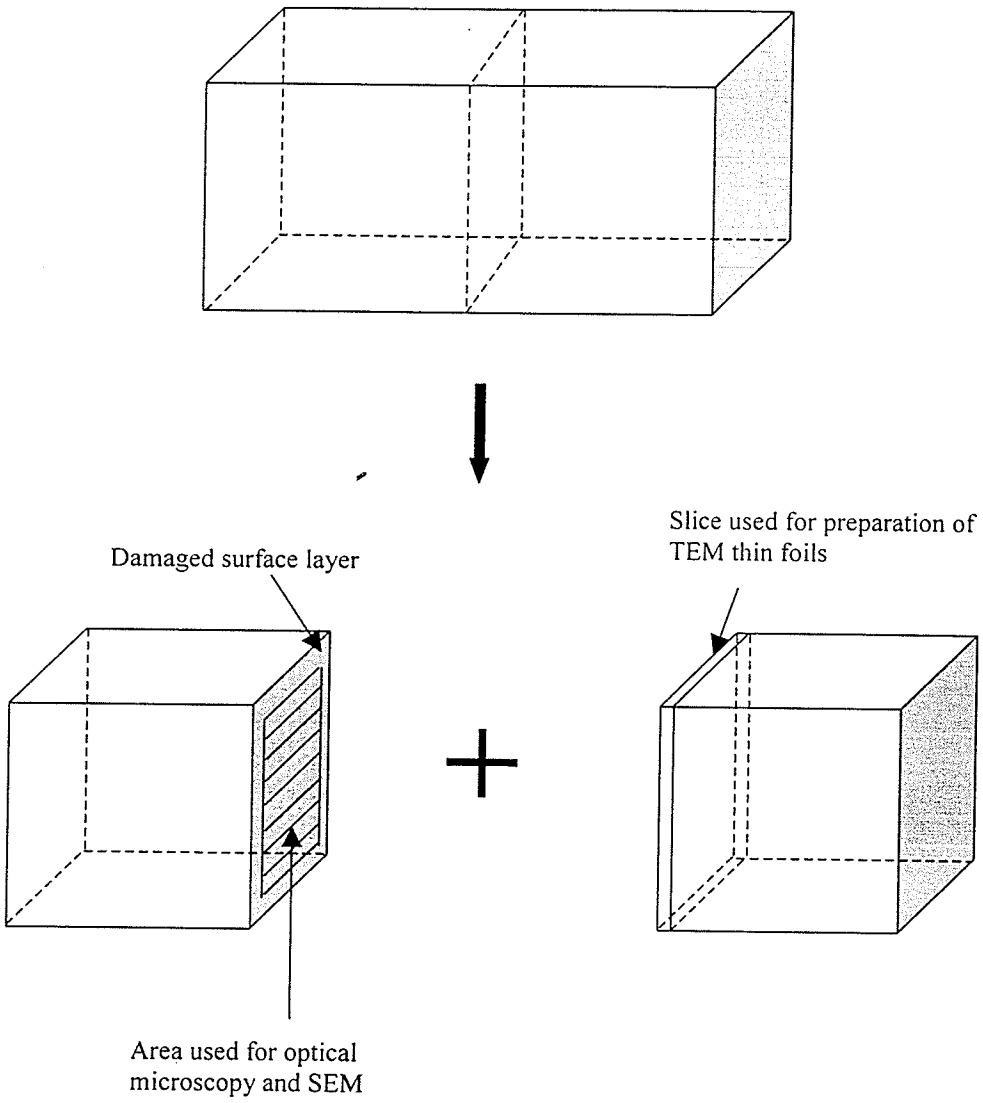

Figure 3.3: Schematic drawing of the sample used for heat treatment and the sections used for the preparation of samples for optical microscopy, SEM and TEM.

boundaries based on the gray level. A square grid of known dimensions was, therefore, superimposed on the micrographs and the grain size (lamellar colony size) was measured as the mean intercept length ($\bar{l}$). As many as 50 to 80 lines were used to measure the mean intercept length in one area. A representative micrograph with superimposed square grid is shown in Figure 3.4.

3.3.2 Measurement of volume fraction of massively transformed gamma

The massively transformed gamma etched dark and the untransformed α_2-phase etched white in metallographic specimens. The volume fraction of the transformed product was determined by measuring the area of the dark phase in the metallographic section as a percentage of the total area analyzed. This was done based on the difference in gray level between the two phases. Figure 3.5 shows a typical micrograph used during the analysis.

3.4 TRANSMISSION ELECTRON MICROSCOPY

Thin foils were prepared to characterize the microstructure of bulk and sub-surface layer of the heat-treated samples by transmission electron microscopy (TEM). 0.5 mm thick slices were cut from the cross section and from the surface of the specimens using electric discharge machining. These were then reduced to ~100μm in thickness using 600 grit abrasive paper. 3mm diameter discs were punched out by EDM and were further thinned using a Tenupol twin-jet polishing unit. The electrolyte used for twin-jet polishing was a solution of 5% perchloric acid, 30% butan-1-ol and 65% methanol. Twin-jet polishing was carried out at -30 to -35°C and at 30-32 volt. The thin foils were examined in JEOL-2000FX TEM/STEM operated at 200kV.

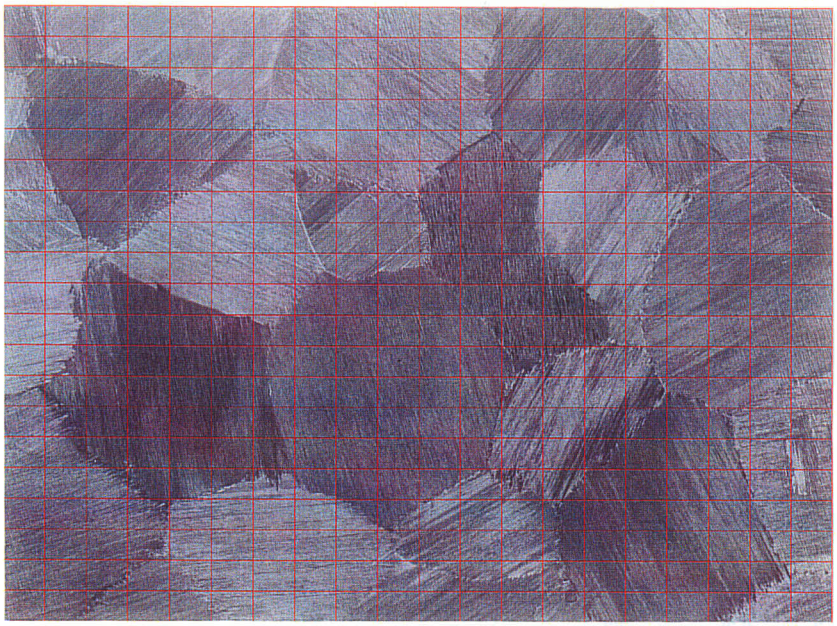

Figure 3.4: An optical micrograph superimposed with a square grid used to measure grain size.

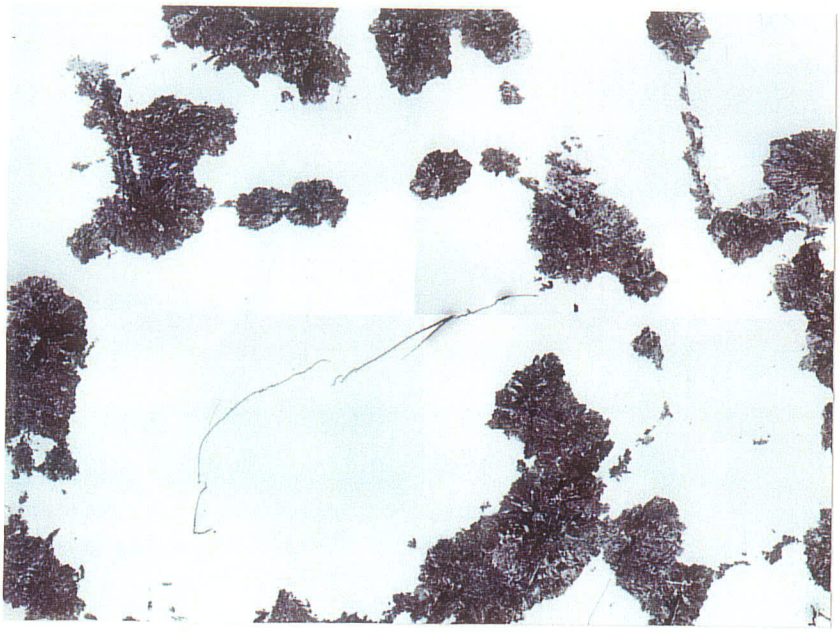

(a)

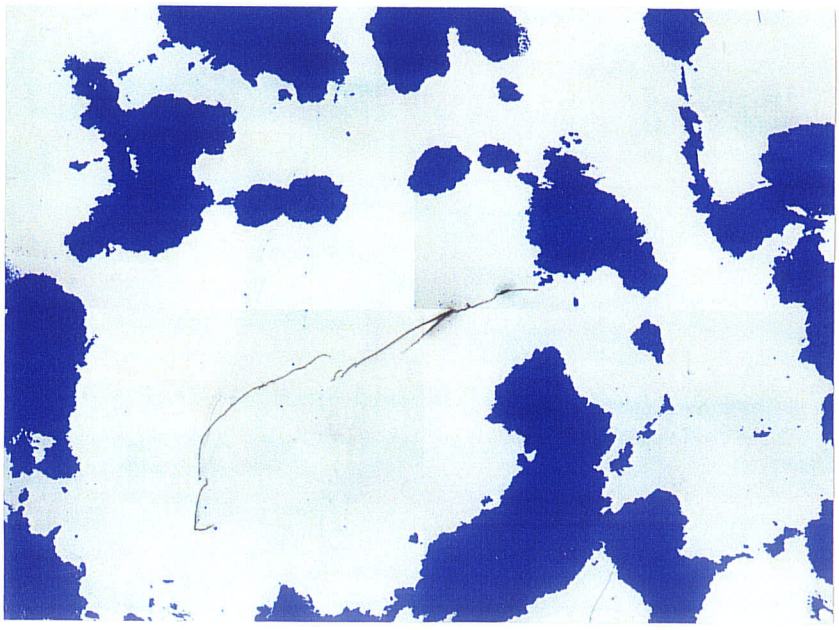

(b)

Figure 3.5: (a) An optical micrograph showing massively transformed gamma (dark) and alpha-2 phase (white). (b) micrograph shown in (a) after analysis. The volume fraction was measured by measuring the blue area as a fraction of the total area of the micrograph.

Chapter 4

RESULTS

The results obtained from microstructural characterization of as-received alloys and those of the specimens heat-treated under various conditions, and their hardness values are presented in this chapter.

4.1 MICROSTRUCTURE OF THE AS-RECEIVED MATERIAL

Figures 4.1 (a-d) are optical micrographs showing microstructure of the as-received samples of alloys I, II, III, and IV, respectively. As seen from the figures, the microstructures were coarse grained and consisted primarily of lamellar microconstituents. The lamellar colony boundaries in the as-received samples were not well defined and hence the as-received grain size could not be measured. The microconstituents of fully lamellar structure are known to be gamma and alpha-2 phase and they were indeed observed, by TEM analysis of the thin foils, to be present in the as received materials. Figure 4.2 is a representative TEM bright field (BF) image showing the α_2 and γ lamellae in the as-received sample of alloy III. Figure 4.3a is the SADP corresponding to [110] zone axis of γ-phase overlapped with the SADP of $[1\bar{2}10]$ zone axis of α_2 phase, and Figure 4.3b is a schematic drawing of the diffraction pattern showing the orientation relationship between α_2 and γ phase in the lamellar structure. The orientation relationship was found to be $[110]\gamma//[1\bar{2}10]\alpha_2$ and $(1\bar{1}1)\gamma//(0001)\alpha_2$.

(a)

(b)

Figure 4.1 (continued...)

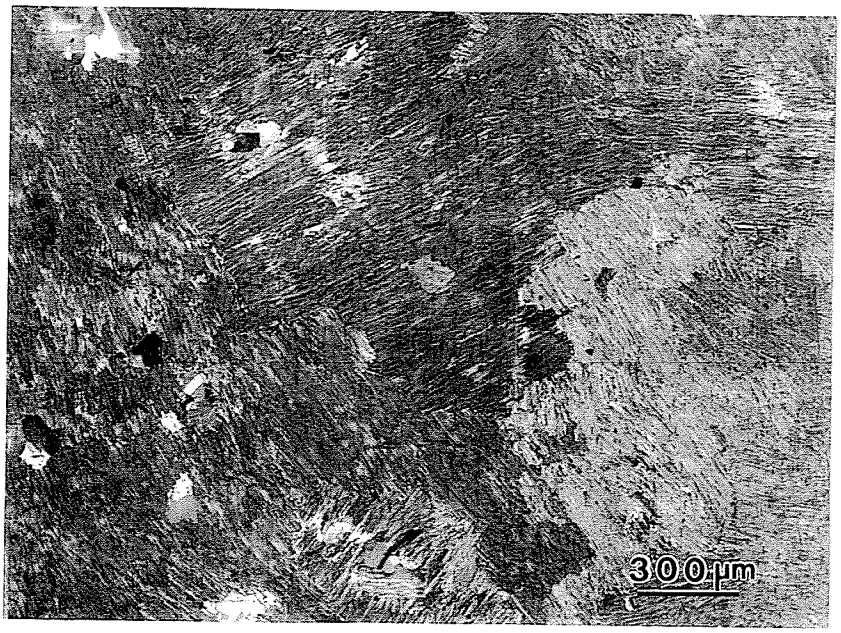

(c)

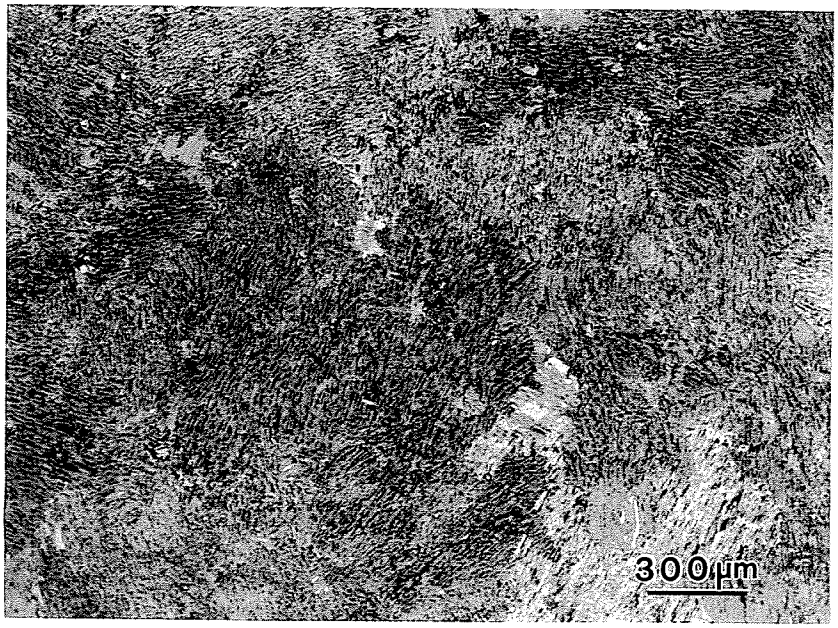

(d)

Figure 4.1: As-received microstructure of (a) alloy I (Ti-45Al), (b) alloy II (Ti-45Al-2Nb), (c) alloy III (Ti-45Al-2Nb-0.4Mn), and (d) alloy IV (Ti-45Al-2Nb-2Mn).

Figure 4.2:TEM bright field image showing fully lamellar microstructure in as-received sample of alloy III.

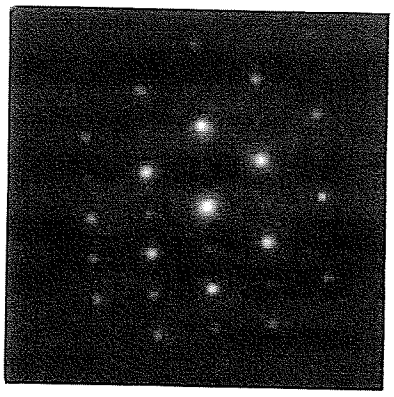

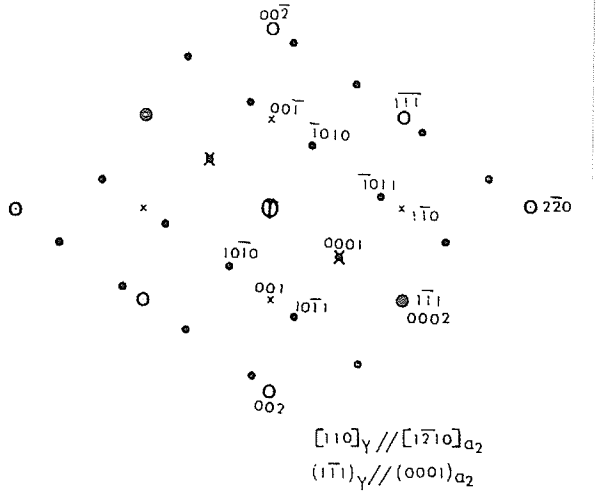

Figure 4.3: (a) SADP corresponding to $[110]_\gamma$ zone axis showing orientation relationship between α_2 and γ phase in the lamellar microstructure. (b) Schematic diagram of the SADP shown in (a).

4.2 SURFACE DAMAGE OF SAMPLES DURING ANNEALING AT 1350°C

To study the phase transformation behavior of various alloys during cooling from the α-phase field, specimens of size 12mm x 6mm x 6mm were heated at 1350°C for 30 minutes. The specimens were encapsulated in vycor capsules prior to heat treatment, which were evacuated and back-filled with commercial purity argon in order to maintain inert atmosphere during heat treatment at 1350°C. Examination of quartz capsules after heat treatment revealed discoloration of the capsule wall in the vicinity of the alloy specimens. The specimens were also weighed before and after the heat treatment at 1350°C. The weight measurement data of air-cooled sample of alloy III, given in Table 4.1, suggest a gain in weight following the heat treatment.

It was therefore, decided to analyze and understand the changes that the surface of the specimens underwent during high temperature annealing. The air-cooled specimen of alloy III was examined in detail with particular emphasis on the transformations that take place in the surface and sub-surface region of the specimens during heat treatment. Figure 4.4 shows a back-scattered electron (BSE)-SEM image revealing three distinct regions in the cross section of the specimen heat treated for 30 minutes at 1350°C and subsequently, air-cooled to room temperature. The outer-most layer appears bright and the region below this bright layer appears darker, whereas the bulk appears gray. This contrast in the back-scattered image indicates a difference in composition between the three regions. The compositions of the three regions measured by EDS/SEM using the pure metal standard MICRO-Q software, by NORAN, are given in Table 4.2. It is seen from the chemical

Table 4.1 Weight of the specimen before and after the heat treatment

weight before HT (gm)	weight after HT (gm)	Gain in weight (gm)
1.6700	1.6737	0.0037

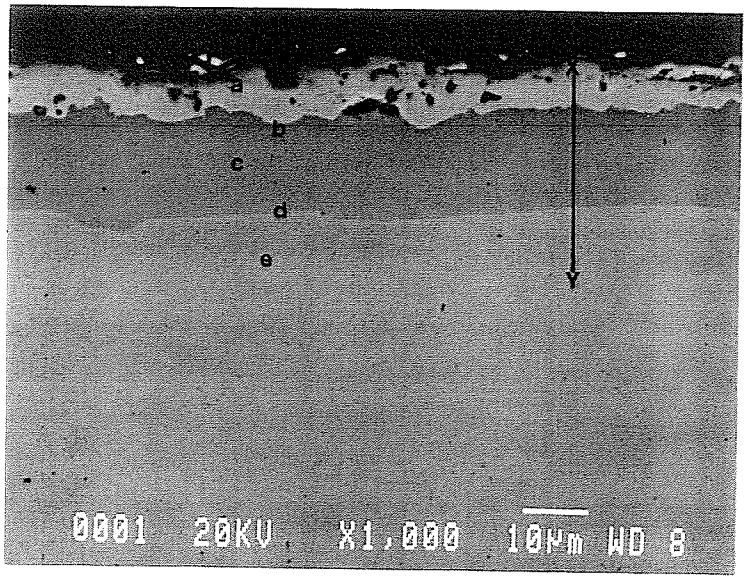

Figure 4.4: Back scattered electron image of the cross section of the air-cooled sample of alloy III showing three distinct regions.

Table 4.2 Composition at various locations in the cross section of the heat treated specimen

Location	Concentration, at.%				
	Ti	Al	Nb	Mn	Si
a	58.90	2.38	1.61	0.70	36.40
b	43.26	53.72	1.95	0.35	0.72
c	44.76	52.58	2.29	0.37	-
d	48.96	48.52	2.17	0.35	-
e	52.5	44.98	2.15	0.37	-

analysis that the outer-most bright layer has higher concentrations of silicon and titanium, and contains very small amounts of aluminum. The darker layer was found to be richer in Al with the aluminum concentration varying from 53 at.% near the Si rich layer to 48 at.% at the dark/gray interface. The thickness of this darker layer was found to be approximately 17 μm. The gray region had 45 at.% Al in it, which is similar to the composition of the as- received material.

An X-ray line scan was also conducted to show the distribution of various elements, namely Al, Si and Ti, in the cross section of the heat treated specimen. The line scan along the line XY marked in Figure 4.4 is shown in Figure 4.5. As seen in this figure, the Al concentration is seen to be the smallest in the outermost surface layer and increases steeply as the distance from the surface increased into the silicon-rich deposited layer. A sudden change in slope was observed at the interface between the deposited layer and the region of the specimen just below this layer, beyond which the profile became almost flat. This is because of the indiscernible difference in aluminum concentration across the Al-rich layer. The Si and Ti concentrations were highest at the surface and gradually decreased as the distance from the surface increased. The Si concentration dropped to zero below the bright outer layer. The presence of high concentration of Si was also confirmed by Si X-ray mapping. An example is given in Figure 4.6, which shows high silicon concentration in the surface layer and virtually no silicon below this layer.

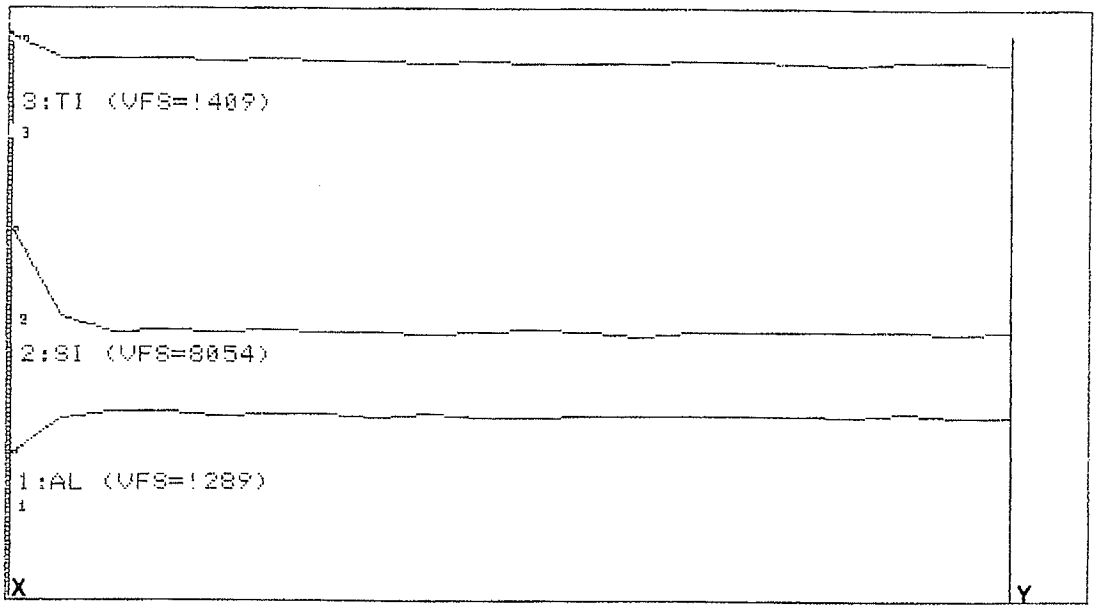

Figure 4.5: X-ray line scan showing distribution of Ti, Si, and Al along the line XY marked in Figure 4.4.

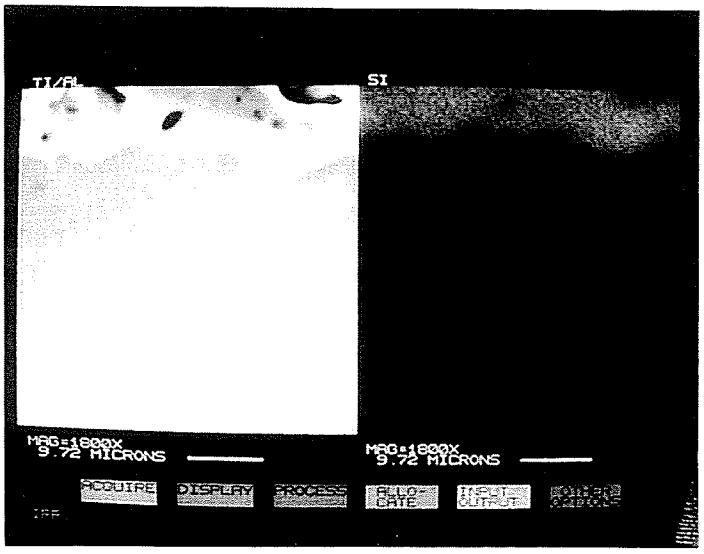

Figure 4.6: Si X-ray mapping showing high concentration of Si in the bright surface layer.

4.3 MICROSTRUCTURE OF THE SURFACE AND SUB-SURFACE REGION

The interior of the specimen underwent a "massive-type" transformation whereas the region near the surface of the specimen had lamellar structure. Secondary electron image of the cross section of the specimen after the heat treatment at 1350°C for 30 minutes is shown in Figure 4.7. It is seen that the outer-most white layer, marked A and about 5-7 μm thick, is the deposited Si-rich layer. The layer just below the deposited layer, marked B and about 17 μm thick, consists of primary single-phase gamma grains. This layer corresponds to the aluminum-rich dark layer observed in Figure 4.4. The interior bulk, marked D, is observed to be a transformed, possibly massive gamma, phase. The region between the Al-rich layer and the massively transformed bulk, about 300 μm thick and marked C, was observed to have a fully lamellar structure.

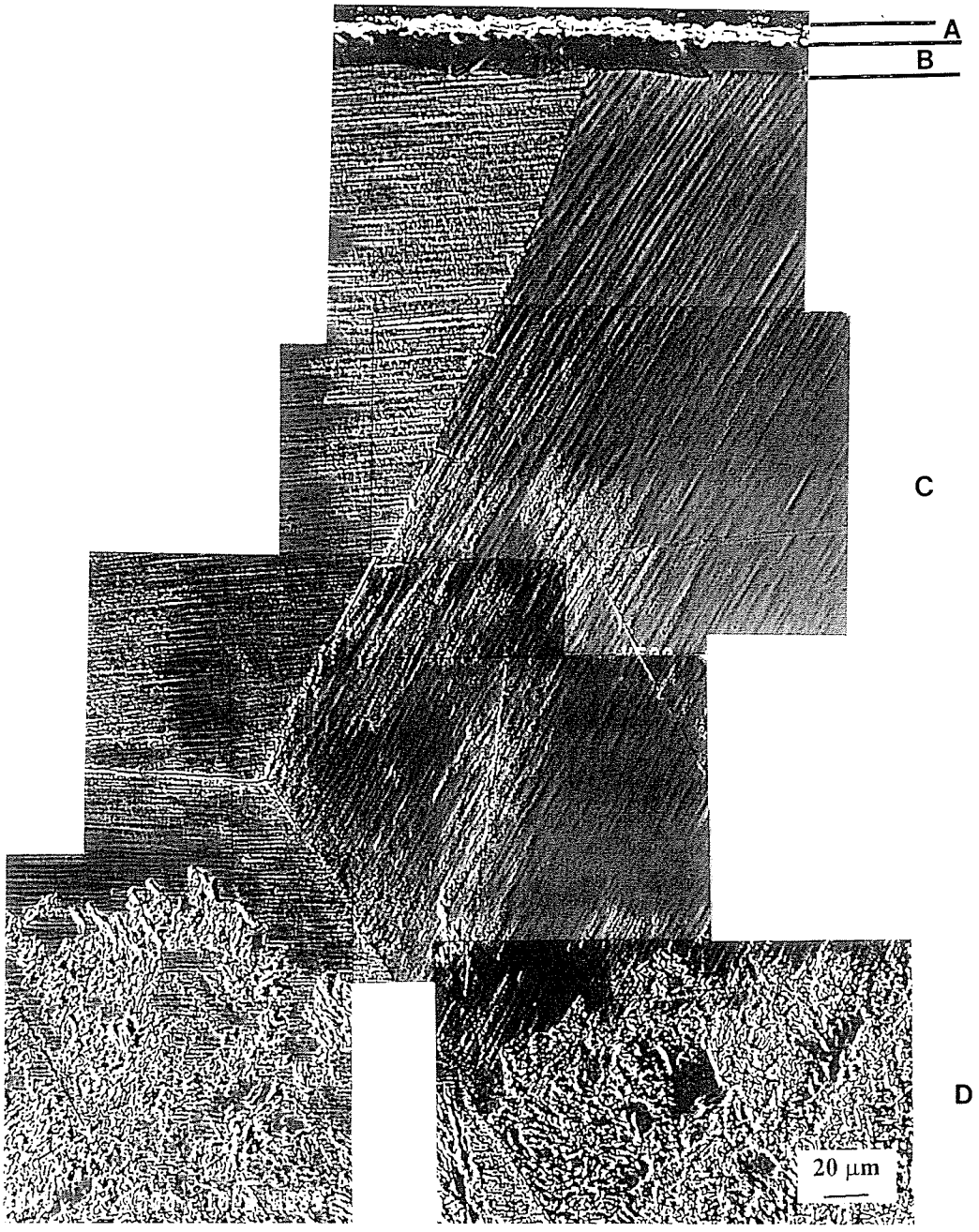

Figure 4.7: Secondary electron image of the cross section of the air-cooled specimen of alloy III.

4.4 MICROSTRUCTURAL CHARACTERIZATION OF THE BULK OF HEAT-TREATED SPECIMENS

Phase transformation behavior of Ti-45Al based alloys with nominal composition of Ti-45Al, Ti-45Al-2Nb, Ti-45Al-2Nb-0.4Mn and Ti-45Al-2Nb-2Mn during cooling was studied by microstructural examination of the heat-treated specimens by optical microscopy, SEM and TEM. The heat treatments consisted of heating the alloy samples of dimensions 12mm x 6mm x 6mm in the α-phase field (1350°C), followed by cooling by furnace cooling (FC), air cooling (AC), oil quenching (OQ) and water quenching (WQ). The measured cooling rates corresponding to these cooling processes were as follows: FC ~ 2.5 °C/min; AC ~ 25 °C/sec; OQ ~ 155 °C/sec; and WQ ~ 1000 °C/sec. The experimental setup used to measure the cooling rates has been already discussed in Chapter 3.

As described in sections 4.2 and 4.3, Si deposited on the surface of the specimens during heat treatment and affected the microstructural evolution in the sub-surface region of the heat-treated specimens. Therefore, necessary precautions were taken during microstructural examination of the heat-treated specimens. Optical microscopy and SEM imaging was done on the interior of the cross-section of the heat-treated specimens. Specimens for TEM analysis were also prepared from the center of the specimens. The results of microstructural characterization are presented in the following sub-sections.

4.4.1 Alloy I (45-0-0)

Furnace cooling of alloy I to room temperature after annealing at 1350°C for 30 minutes resulted in a complete decomposition of the high temperature alpha phase and in the formation of a fully lamellar microstructure (Figure 4.8a). The average lamellar colony size (grain size), measured by the technique described in section 3.3.1, was observed to be ~ 980 microns. Figure 4.8b shows a bright field (BF) image representing the lamellae in the furnace-cooled sample. Figure 4.8c shows a selected area diffraction pattern (SADP) corresponding to [110] zone axis of the γ-phase illustrating the orientation relationship between α_2 and γ phase. Coarsened γ lamellae were also observed near the grain boundaries (Figure 4.9).

Increasing the cooling rate to air cooling (AC) from 1350°C resulted in a microstructure consisting of fine lamellae with relatively planar grain boundaries (Figure 4.10(a,b)). The grain size (lamellar colony size) was observed to be the same as that in FC samples. Also observed, was the occasional presence of dark patches of gamma phase near the grain boundaries, which were identified to be massively transformed gamma phase, as will be shown later. The volume fraction of this phase was approximately 5 %. TEM analysis confirmed the dark phase to be massively transformed gamma (γ_m). Figures 4.11 (a-b) show diffraction patterns conforming well to [111] and [121] zone axes of gamma phase. Figures 4.12 (a-b) are a pair of TEM bright field and dark field images confirming the presence of massively transformed gamma in the air-cooled samples. The massive gamma domains existed in clusters (Figure 4.13). No specific low index orientation relationship was observed between the massively transformed γ and the parent matrix and

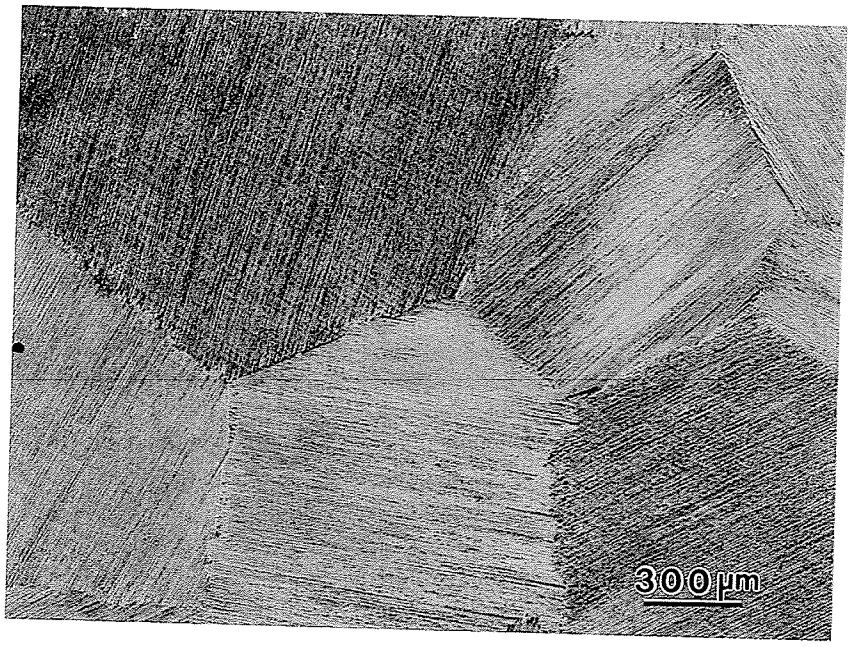

(a)

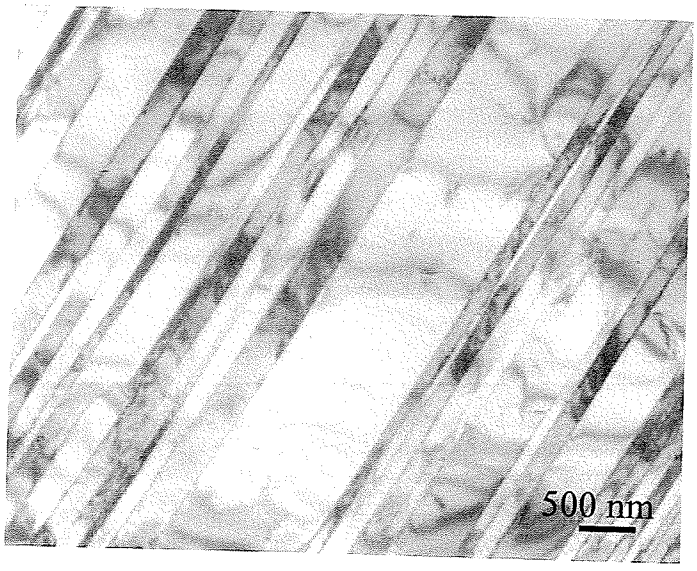

(b)

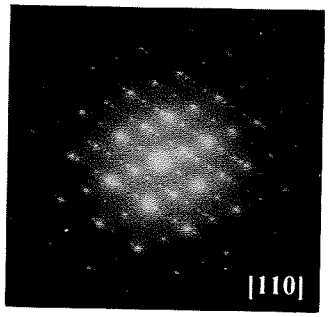

(c)

Figure 4.8: (a) Optical micrograph showing microstructure obtained in alloy I after annealing at 1350°C for 30 minutes followed by furnace cooling; (b)TEM bright field image showing lamellar microstructure in FC sample of alloy I; (c) SADP showing orientation relationship between α_2 and γ phase in lamellar microstructure.

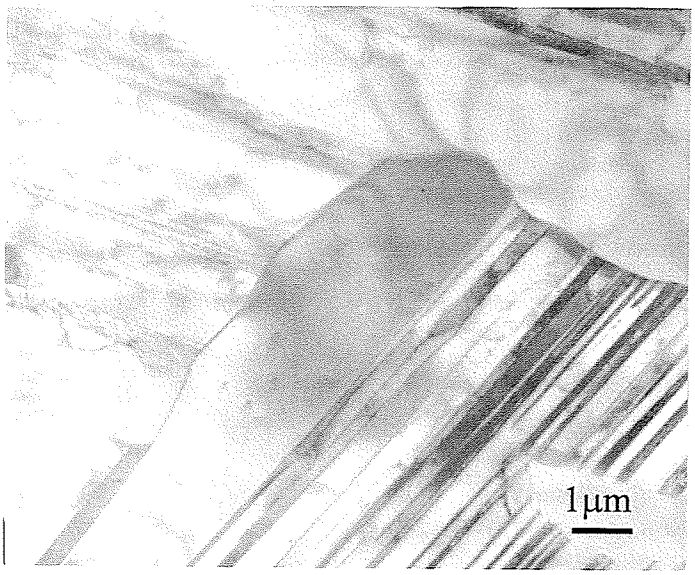

Figure 4.9: TEM bright field image showing coarsened lamellae near lamellar colony boundary in FC specimen of alloy I.

(a)

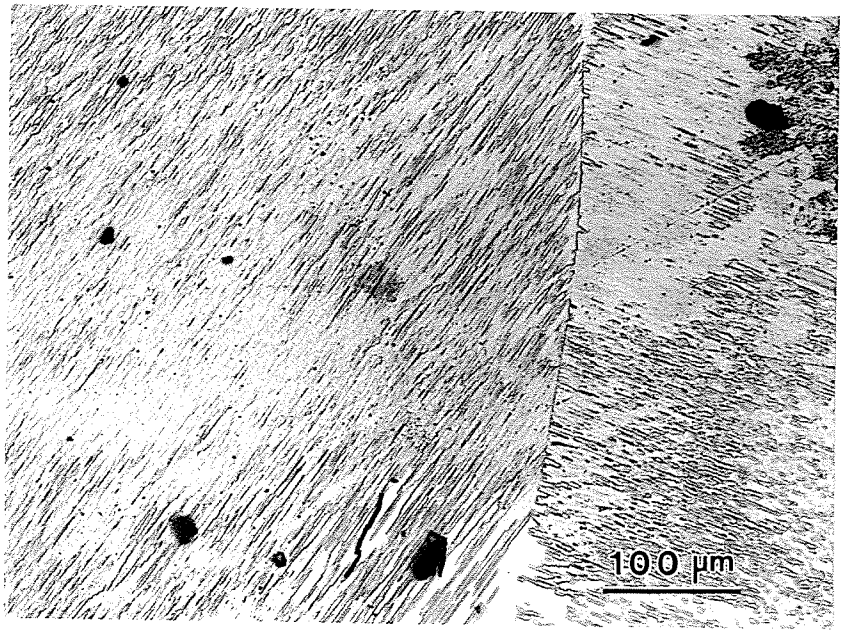

(b)

Figure 4.10: Optical micrograph showing microstructure of air-cooled specimen of alloy I ((a) 50 X and (b) 200 X).

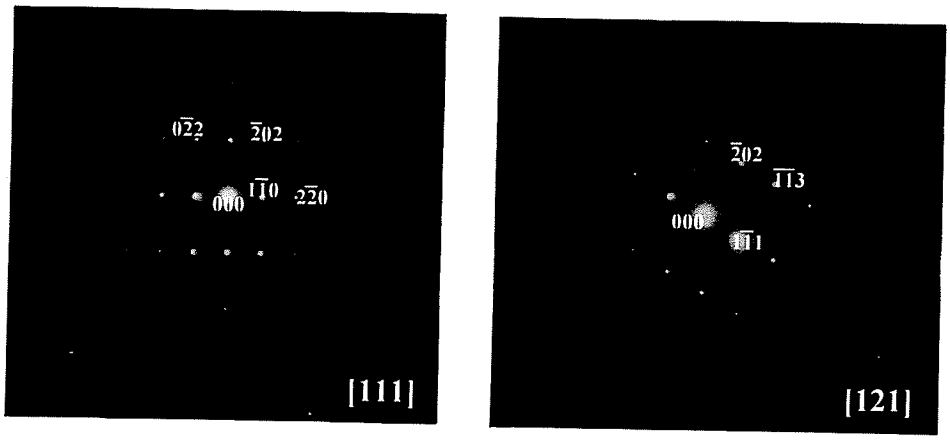

(a) (b)

Figure 4.11: SADP's corresponding to (a) [111] and (b) [121] zone axes of gamma phase.

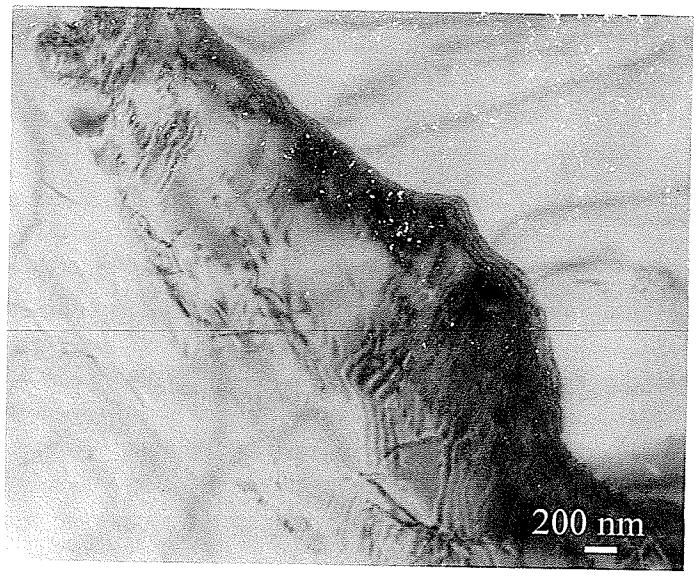

(a)

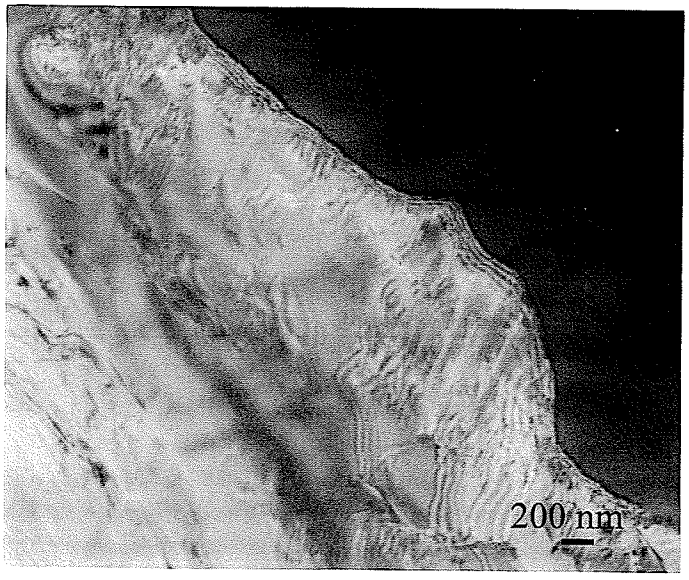

(b)

Figure 4.12: TEM bright field (a) and dark field (b) image confirming the presence of massively transformed gamma in the air-cooled sample of alloy I.

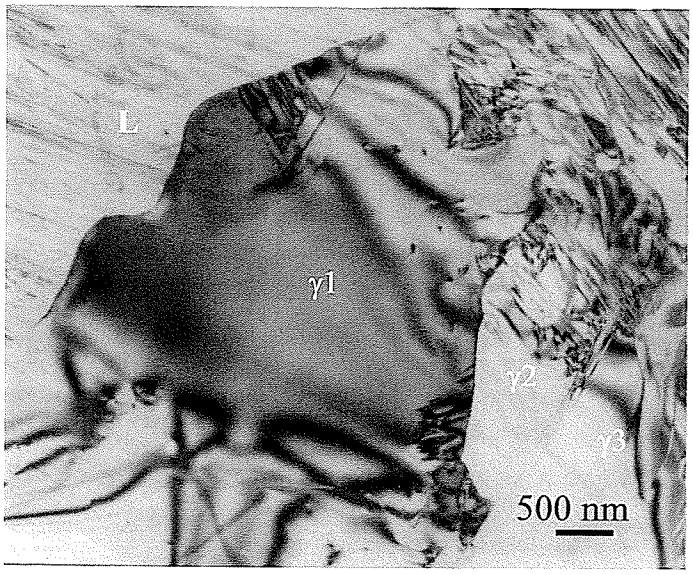

Figure 4.13: TEM bright field image showing three different γ_m grains in a cluster in the air-cooled sample of alloy I.

between the neighboring γ_m domains. α_2 phase was also observed along with γ_m and fine lamellae (Figure 4.14 (a-b)). Gamma phase was also found to be present along the grain boundaries (Figure 4.14a and Figure 4.15), suggesting that γ_m nucleates at the grain boundaries and subsequently propagates into the neighboring grains, when the conditions are favorable.

Further increase in cooling rate to oil quenching (OQ) resulted in an increase in the volume fraction of massively transformed gamma to ~20 %. The resulting microstructure consisted primarily of α_2 and γ_m (Figure 4.16a). Fine lamellae were also observed in some regions (Figure 4.16b). Figure 4.17 is a TEM bright field image showing the microstructure of a representative area of the sample that consisted of large areas of γ_m with small patches of fine lamellae between the γ_m domains. The presence of massive gamma phase was confirmed by bright field and dark field images and SADP's, as shown in Figure 4.18 (a-c). It was also observed that within one grain, all the massive gamma domains had almost the same orientation. Some of the γ_m domains were also observed to have stepped growth front (Figure 4.19).

Water quenching the specimens resulted in almost complete suppression of the massive transformation by the competing $\alpha \rightarrow \alpha_2$ ordering reaction. The resulting microstructure (Figure 4.20) consisted of 8-10 % γ_m in α_2 matrix. TEM analysis confirmed the matrix to be α_2 phase. Figure 4.21a is a bright field image showing α_2 phase. Figure 4.21b is an SADP corresponding to $[0001]_{\alpha 2}$ zone axis. No γ_m could be observed in the TEM thin foils. Back scattered electron image of the polished section of the WQ sample revealed a

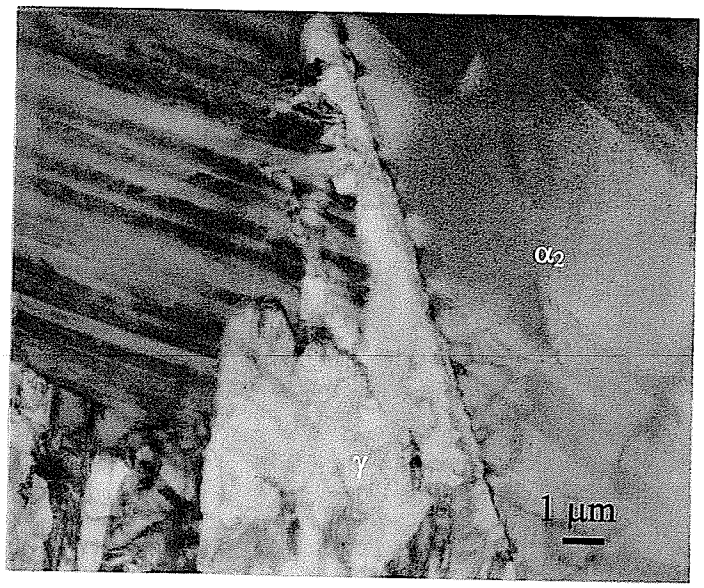

(a)

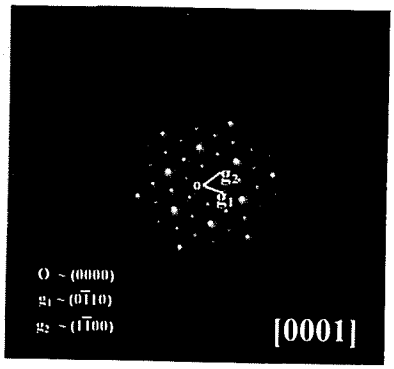

(b)

Figure 4.14: (a) TEM bright field image showing the presence of α_2 phase along with γ_m and fine lamellae in the air-cooled sample of alloy I. (b) SADP corresponding to [0001] zone axis of alpha-2.

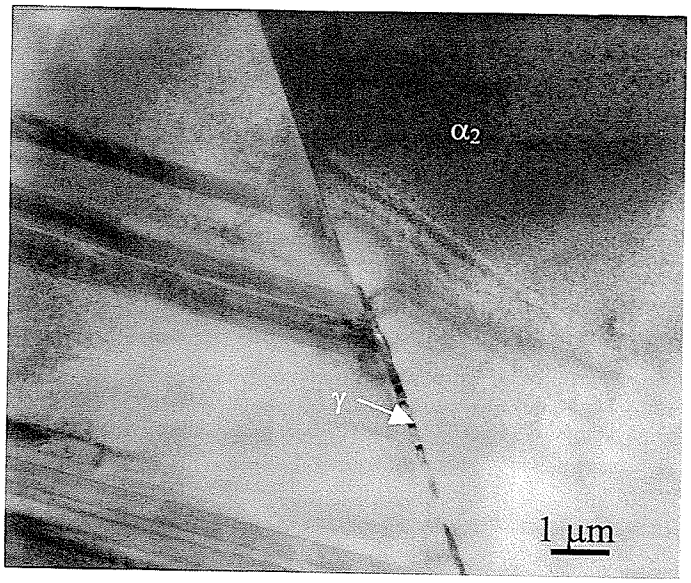

Figure 4.15: TEM bright field image showing the presence of gamma phase at grain boundary in the air-cooled sample of alloy I.

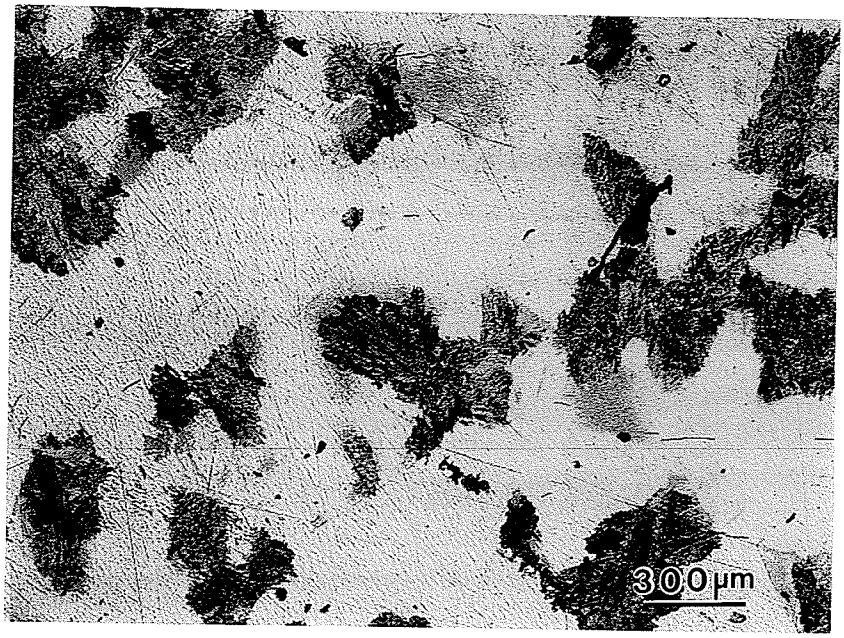

(a)

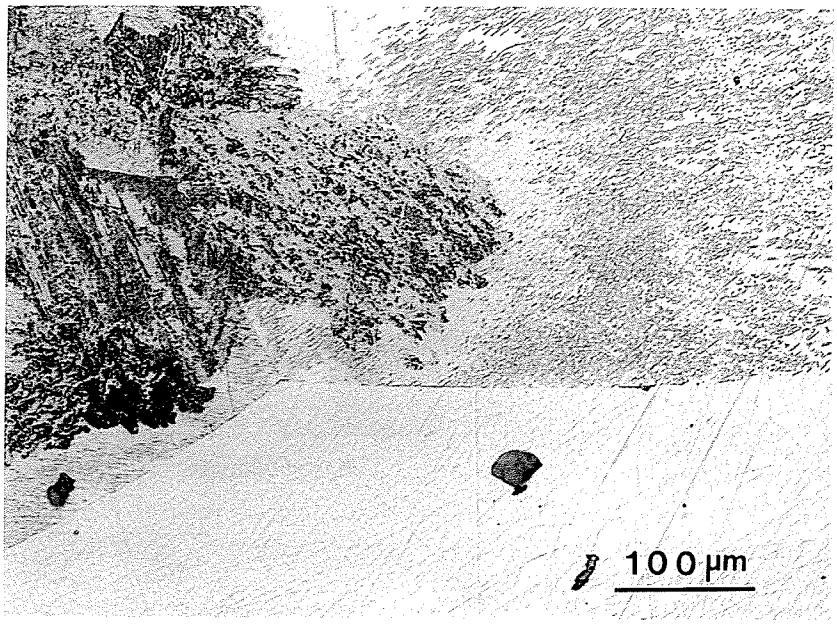

(b)

Figure 4.16: Optical micrograph showing the microstructure of the oil-quenched sample of alloy I. ((a) 50 X and (b) 200 X)

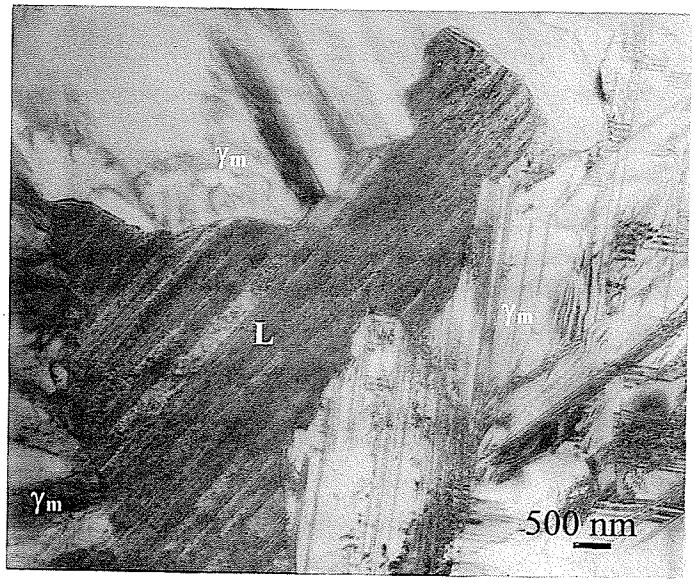

Figure 4.17: TEM bright field image showing fine lamellae along with massively transformed gamma phase in the oil-quenched sample of alloy I.

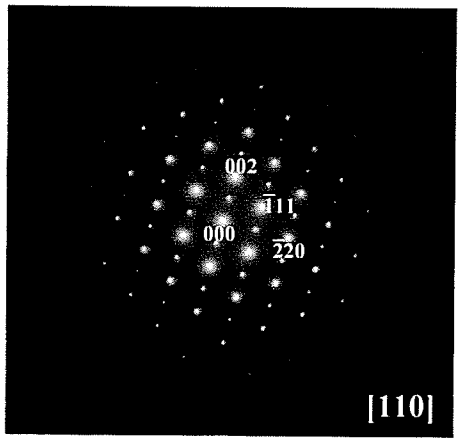

(a)

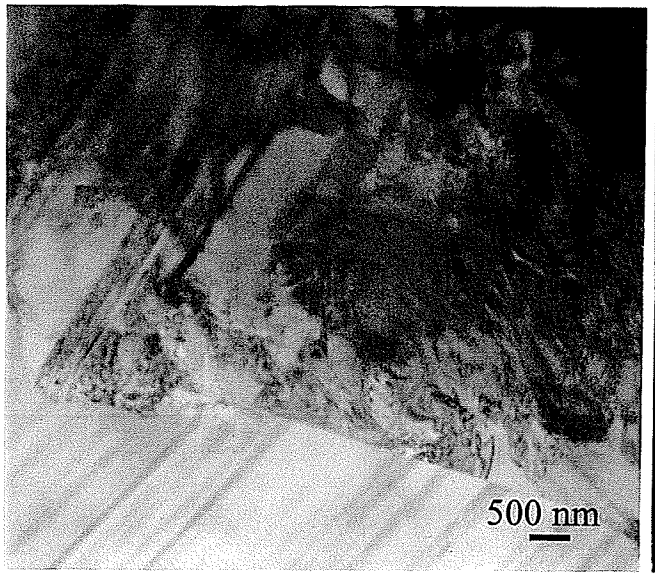

(b)

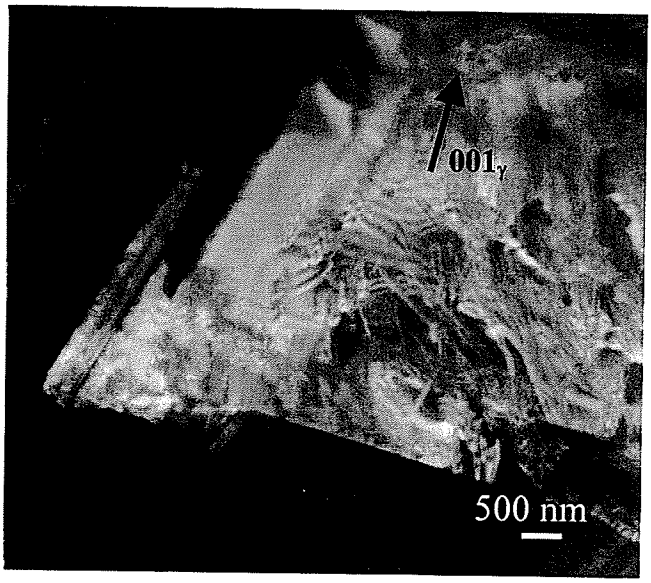

(c)

Figure 4.18: (a) SADP corresponding to $[110]_\gamma$ zone axis; (b) bright field image and (c) dark image confirming the presence of massively transformed gamma in the oil quenched sample of alloy I.

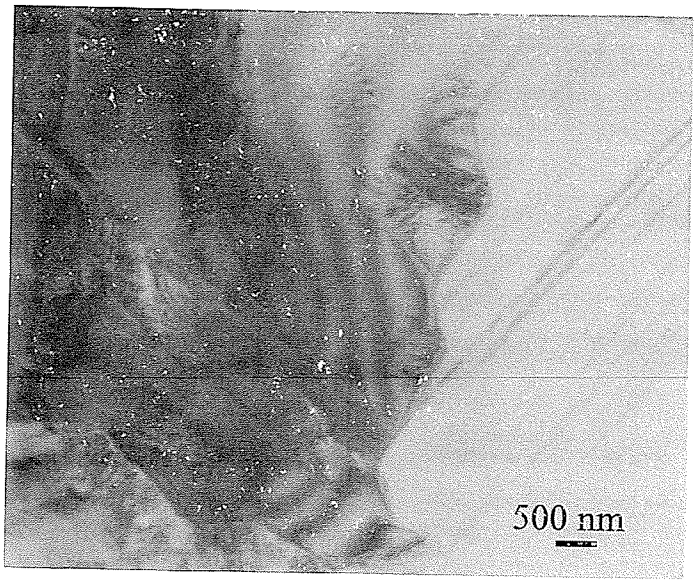

Figure 4.19: Bright field image showing stepped interface.

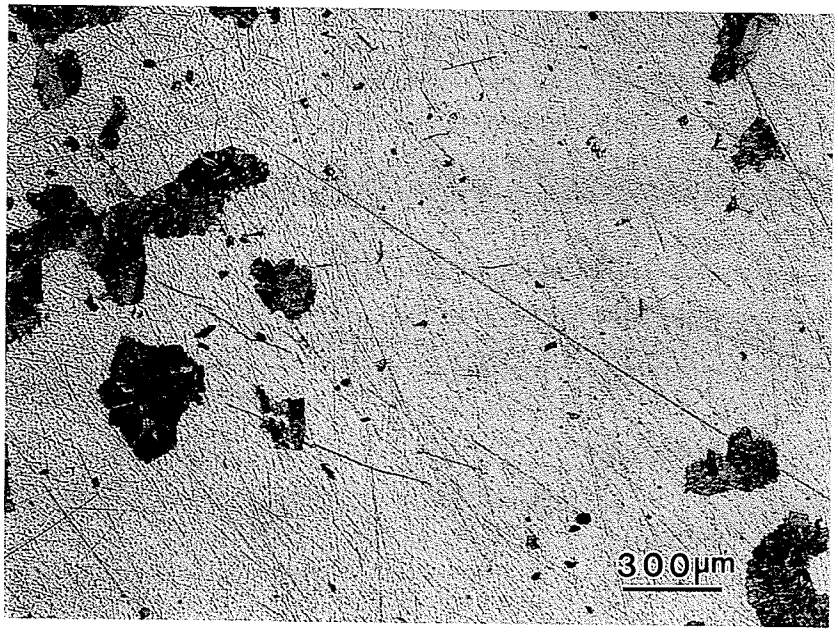

Figure 4.20: Optical micrograph showing the microstructure of the water-quenched sample of alloy I.

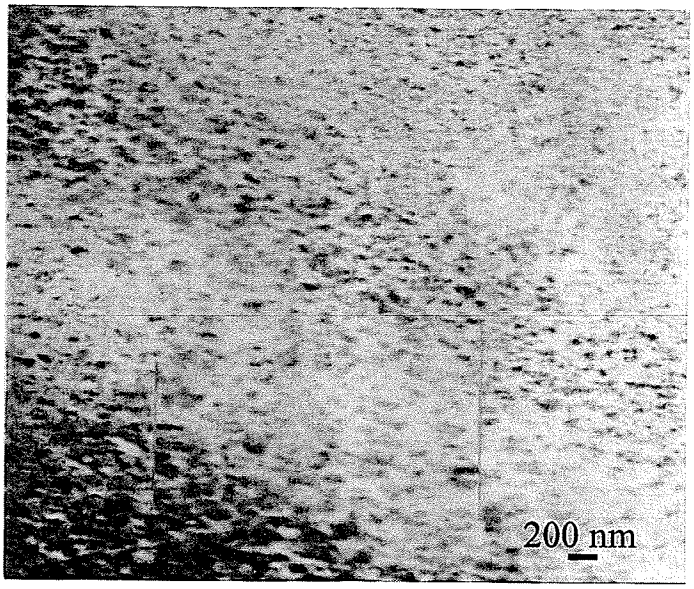

(a)

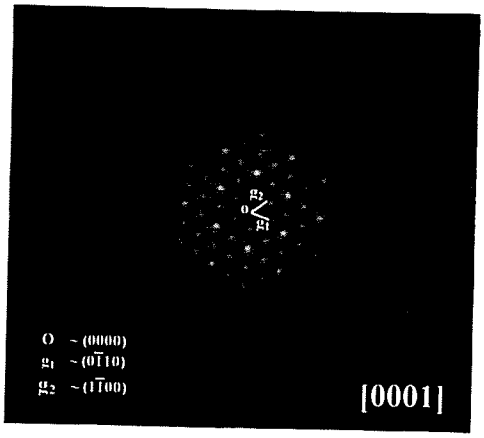

(b)

Figure 4.21: (a) TEM bright field image and (b) SADP corresponding to $[0001]_{\alpha 2}$ zone axis confirming the presence of alpha-2 phase in the water-quenched sample of alloy I.

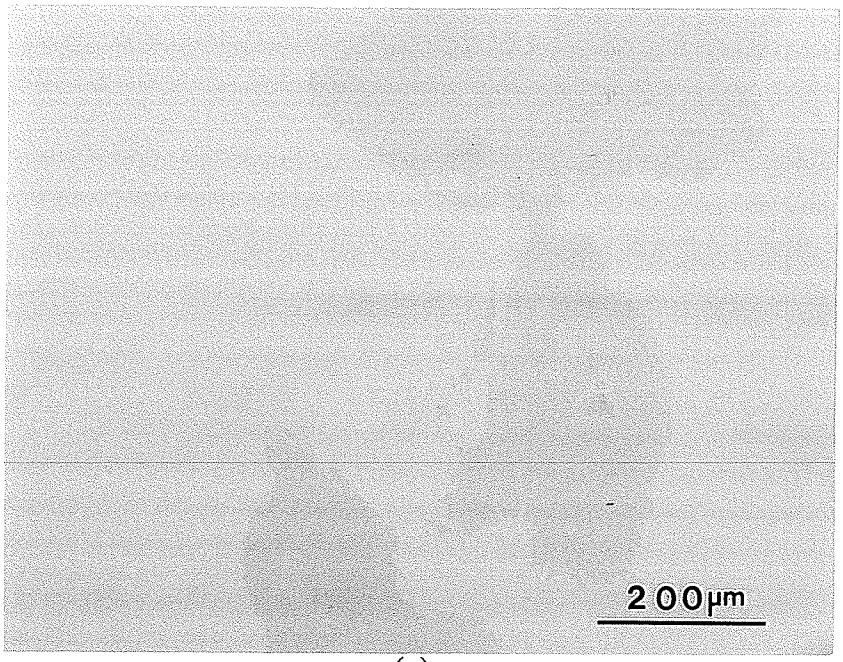

(a)

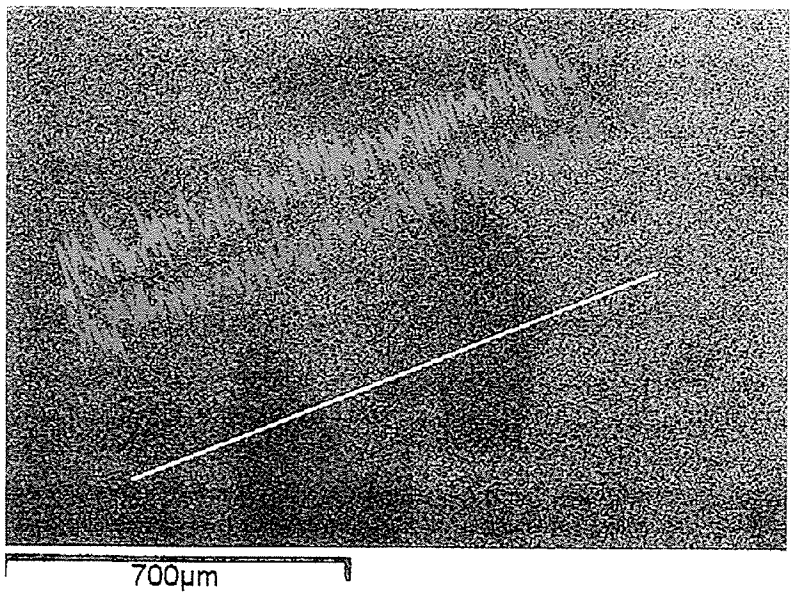

(b)

Figure 4.22: (a) SEM back scattered image of the water-quenched sample of alloy I showing weak composition contrast. (b) Ti and Al X-ray line scan showing the distribution of the two elements in the product and parent phases.

Table 4.3 Composition of different phases in water-quenched samples of alloy I

Phases	Composition, at.%	
	Al	Ti
α_2	44.43	55.57
γ_m	45.56	54.44

Table 4.4 Volume fraction of massively transformed gamma in heat-treated samples of alloy I

Cooling rate	V_f of massive γ_m, (%)
AC	5
OQ	20
WQ	8-10

weak contrast between the two product phases, α_2 and γ_m (Figure 4.22a). Table 4.3 shows the composition of the two phases. As seen, there is no significant difference in the composition of the two phases. The dark gamma phase has a slightly higher concentration of Al, which accounts for the weak contrast in Figure 4.22a. Al and Ti X-ray line scan (Figure 4.22b), however, did not show any perceivable difference in composition between the two phases. Table 4.4 shows the variation of volume fraction of massively transformed gamma with cooling rate in the microstructure of the heat-treated samples.

4.4.2 Alloy II (45-2-0)

Furnace cooling (FC) of alloy II after annealing at 1350°C for 30 minutes also resulted in a complete decomposition of the high temperature alpha phase and the formation of a fully lamellar microstructure (Figure 4.23), with an average colony size of 1125 microns. Figure 4.24a is a BF image showing α_2 and γ lamellae in the FC samples. Figure 4.24b is a SADP corresponding to the [110] zone axis of γ-phase showing orientation relationship between the two microconstituents of the lamellar microstructure.

Increasing the cooling rate to air cooling (AC) resulted in a conspicuous change in the microstructure (Figure 4.25(a-b)). As seen in the figure, air cooled sample exhibited a microstructure consisting primarily of alpha-2 phase with some dark patches of massively transformed gamma regions near the grain boundaries ($V_f \sim 8$ %). However, no γ_m domains could be observed in TEM thin foils because of very low percentage of the transformation product present in the microstructure. Figure 4.26(a-b) show SADP's corresponding to $[1\bar{2}13]$ and $[1\bar{2}10]$ zone axes of α_2 phase obtained from the matrix

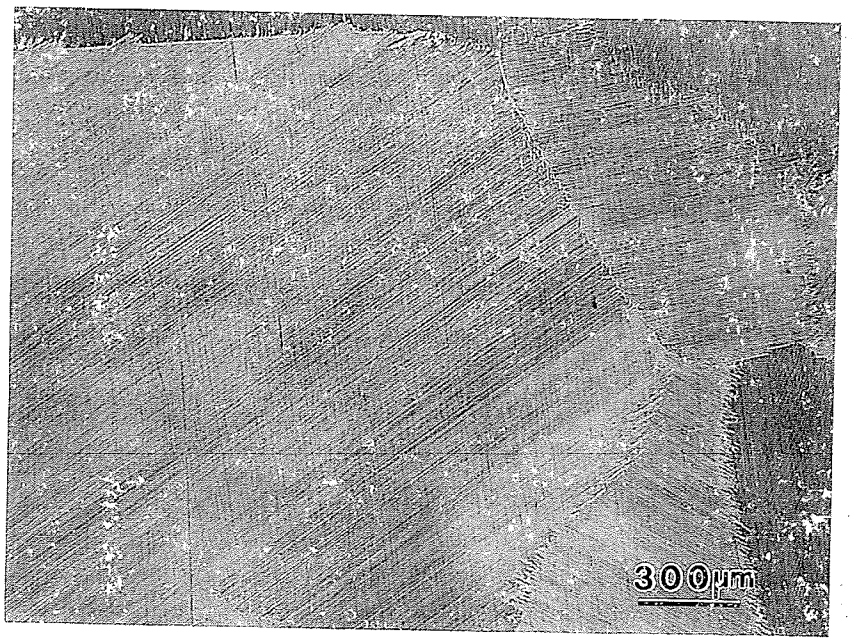

Figure 4.23: Optical micrograph showing microstructure obtained in alloy II after annealing at 1350°C for 30 minutes followed by furnace cooling.

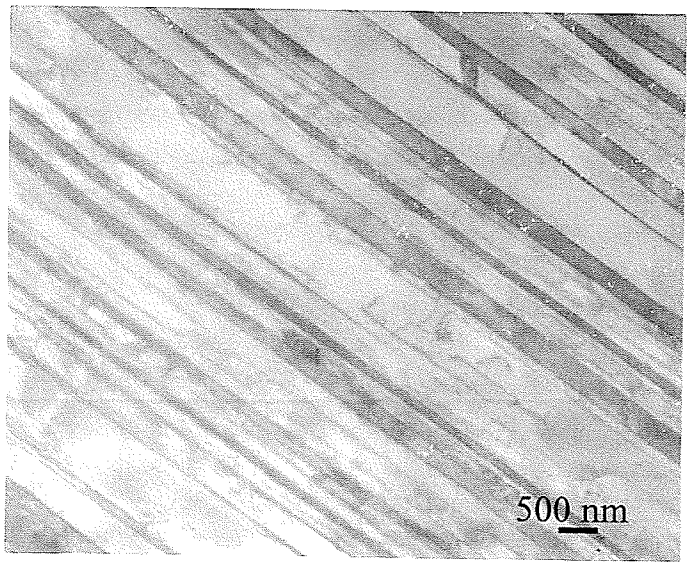

(b)

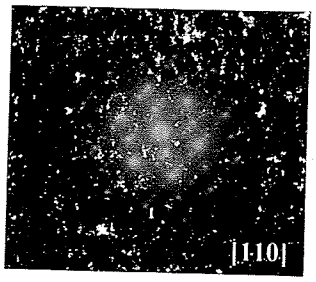

(c)

Figure 4.24: (a) TEM bright field image showing α_2 and γ lamellae in the FC sample of alloy II. (b) SADP showing orientation relationship between the lamellar micro-constituents.

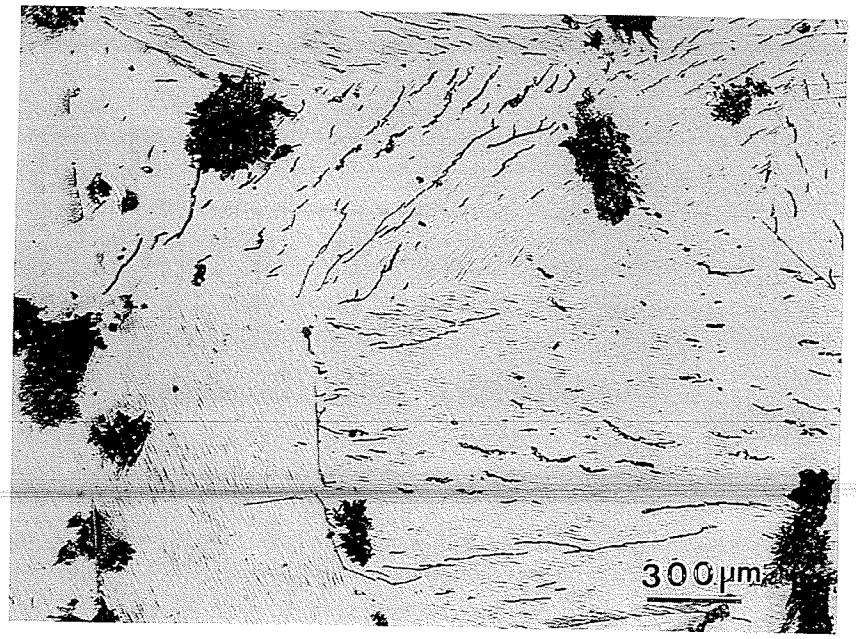

(a)

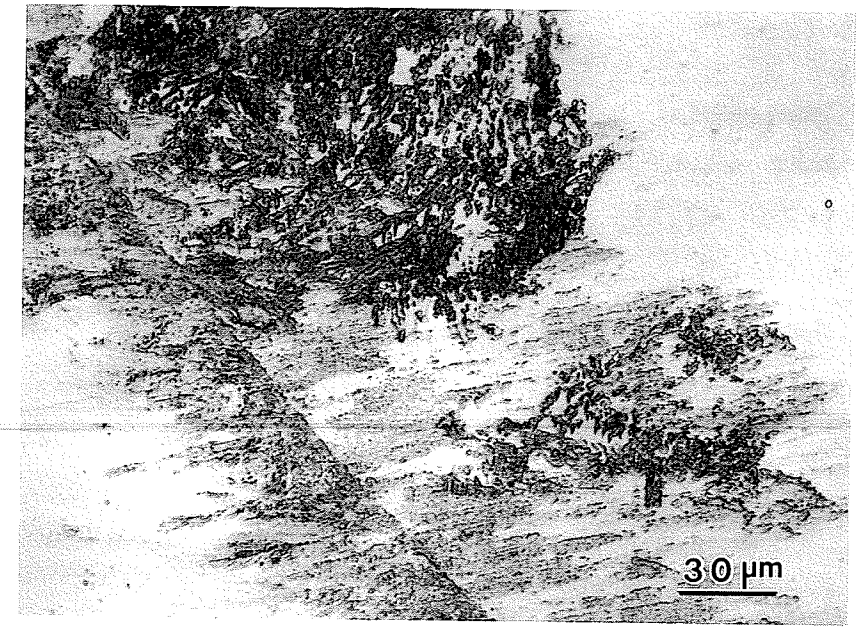

(b)

Figure 4.25: Optical micrograph showing microstructure of the air-cooled specimen of alloy II. ((a) 50 X and (b) 500 X)

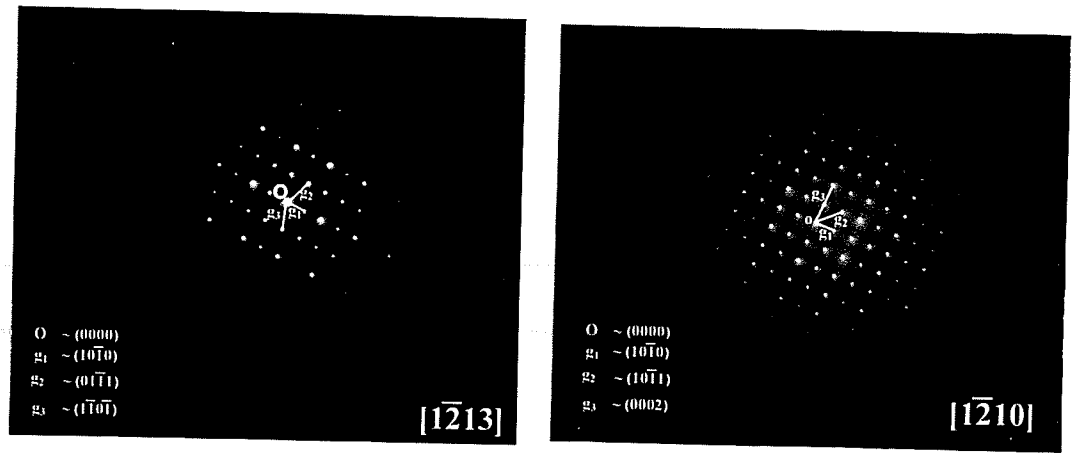

(a) (b)

Figure 4.26: SADP's corresponding to (a) [1$\bar{2}$13] and (b) [1$\bar{2}$10] zone axes of alpha-2 phase.

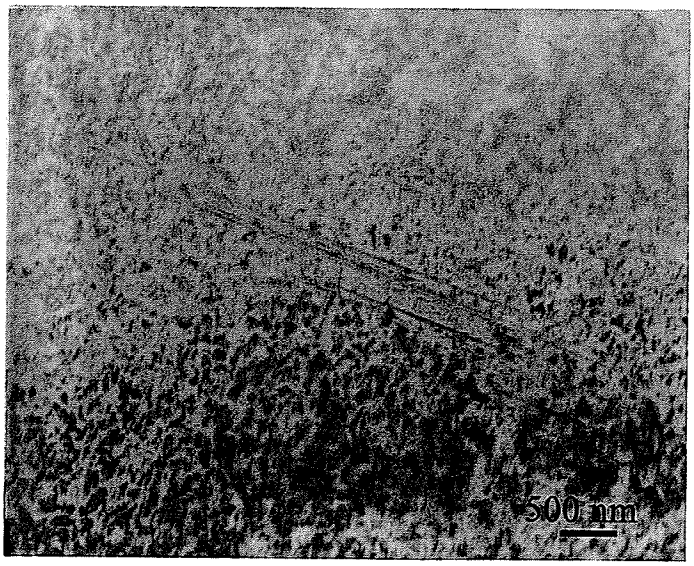

Figure 4.27: TEM bright field image showing the presence of alpha-2 phase as the matrix in the air-cooled sample of alloy II.

confirming the matrix to be α_2. Figure 4.27 is the TEM bright field image of the thin foil prepared from AC sample showing α_2 phase. As seen from Figure 4.25, fine lamellae were also observed in some grains, originating from the grain boundaries. Numerous cracks were also found to exist in the alpha-2 grains and these cracks appear to be oriented along one specific direction in a particular grain.

Further increase in cooling rate to oil quenching (OQ) resulted in almost complete suppression of massive transformation (Vf ~ 3 %). This is in contrast to the microstructural response observed in alloy I, where increase in cooling rate from AC to OQ resulted in an increase in the volume fraction of the massively transformed gamma. The microstructure (Figure 4.28) consisted mainly of α_2 phase with occasional presence of small patches of massively transformed gamma. Figure 4.29a shows a TEM bright field image of the α_2 phase and Figure 4.29b is an SADP corresponding to $[1\bar{2}10]_{\alpha 2}$ zone axis. Back scattered electron image of polished section of OQ sample showed a weak composition contrast between the $\alpha_2$and γ phase (Figure 4.30). Quantitative EDS analysis of the two phases, however, did not indicate any difference in composition (Table 4.5).

Water quenching resulted in complete suppression of the massive transformation by the $\alpha \rightarrow \alpha_2$ ordering reaction and the microstructure consisted entirely of α_2 phase (Figure 4.31). TEM thin foils could not be prepared because the quenched sample was too brittle to slice thin sections. Table 4.6 shows the variation in the volume fraction of massively transformed gamma in the microstructure of the heat-treated samples with cooling rate.

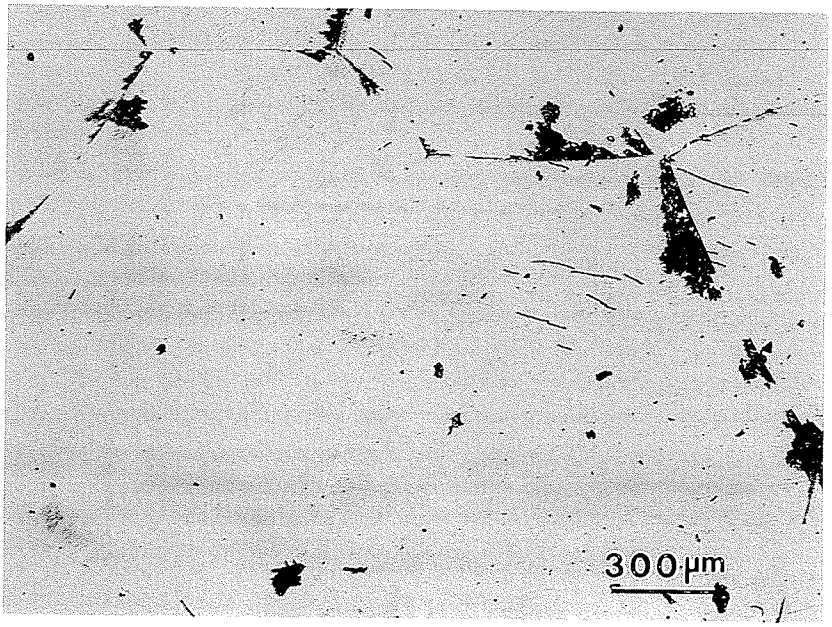

Figure 4.28: Optical micrograph showing the microstructure of the oil-quenched sample of alloy II.

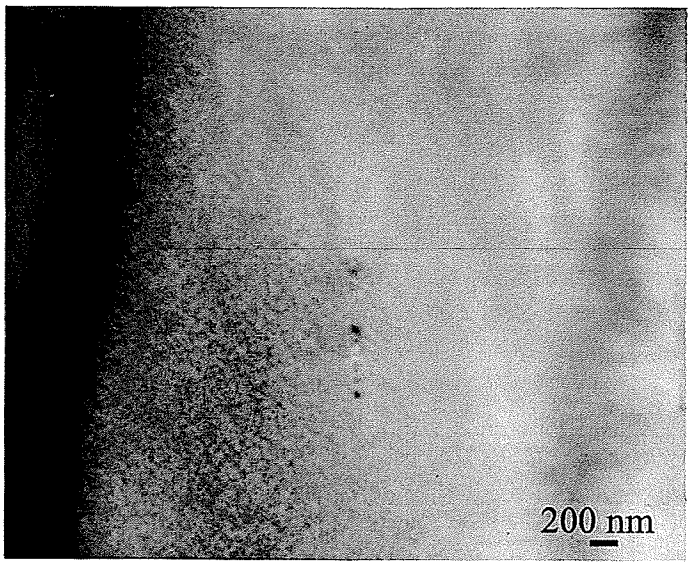

(a)

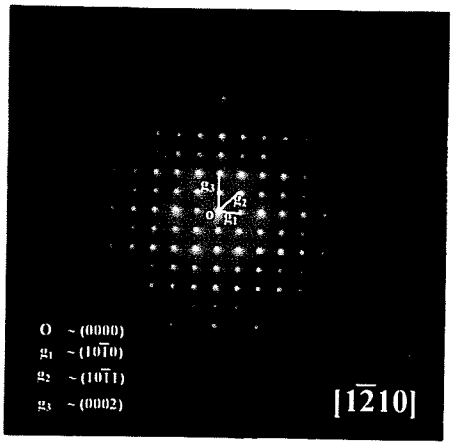

(b)

Figure 4.29: (a) TEM bright field image taken from the matrix of the oil-quenched sample of alloy II; (b) SADP corresponding to $[1\bar{2}10]_{\alpha 2}$ zone axis.

Figure 4.30: SEM back scattered image of the oil-quenched sample of alloy II showing weak composition contrast.

Table 4.5 Composition of different phases in oil-quenched samples of alloy II

Phases	Composition, at.%		
	Al	Nb	Ti
α_2	45.12	1.85	Balance
γ_m	45.02	1.84	Balance

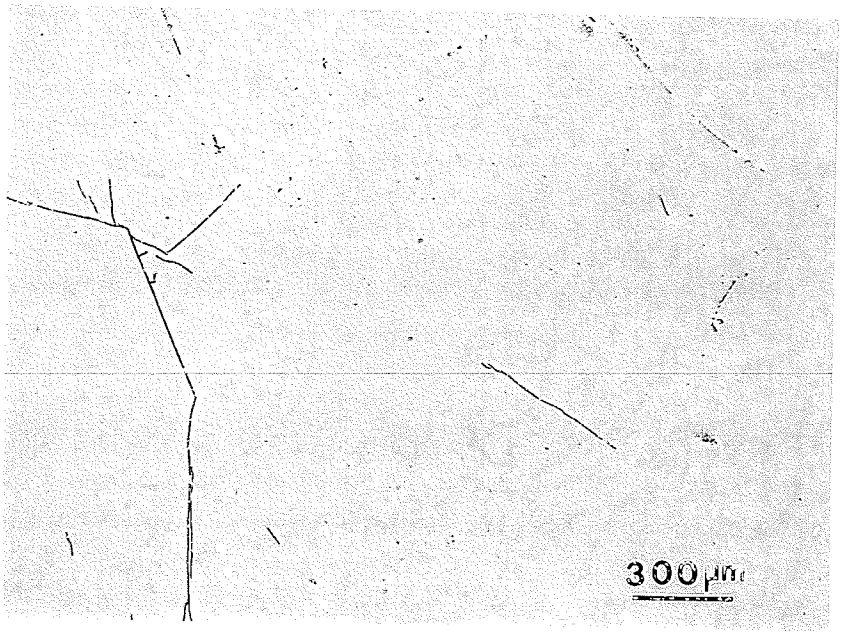

Figure 4.31: Optical micrograph showing the microstructure of the water-quenched sample of alloy II.

Table 4.6 Volume fraction of massively transformed gamma in heat-treated samples of alloy II

Cooling rate	V_f of massive γ_m, (%)
AC	8
OQ	3
WQ	~0

4.4.3 Alloy III (45-2-0.4)

Furnace cooling (FC) of alloy III to room temperature after annealing at 1350°C for 30 minutes once again resulted in a complete decomposition of the high temperature alpha phase and in the formation of a fully lamellar microstructure (Figure 4.32a). The average lamellar colony size was observed to be 850 microns. Figure 4.32b shows a bright field (BF) image representing the lamellae in the furnace-cooled sample.

Increasing the cooling rate to air cooling (AC) led to a massive-type transformation. As shown in Figure 4.33, the microstructure consisted mainly of dark etched regions with very small amounts of white regions. The TEM analysis of thin foils confirmed the presence of massively transformed gamma (γ_m) in the air-cooled sample. Figures 4.34 (a-b) show the selected area electron diffraction patterns (SADP's) corresponding to the [100] and [110] zone axes of the gamma phase, respectively. Figures 4.35 (a-b) are a pair of TEM bright field and dark field images revealing the presence of massively transformed gamma.

A further increase in cooling rate to oil quenching (OQ) resulted in partial suppression of massive transformation by the much faster $\alpha \rightarrow \alpha_2$ ordering reaction. The optical microstructure of the oil quenched specimen, shown in Figure 4.36, indicates the presence of dark etched gamma phase and white alpha-2 phase. The volume fraction of the dark phase was observed to be ~ 90 %. TEM analysis revealed that the dark etched

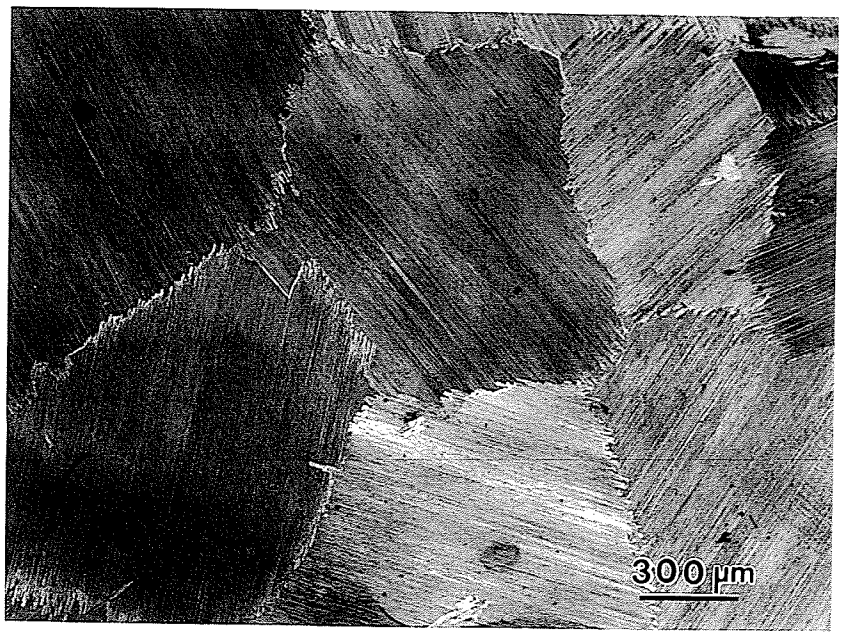

(a)

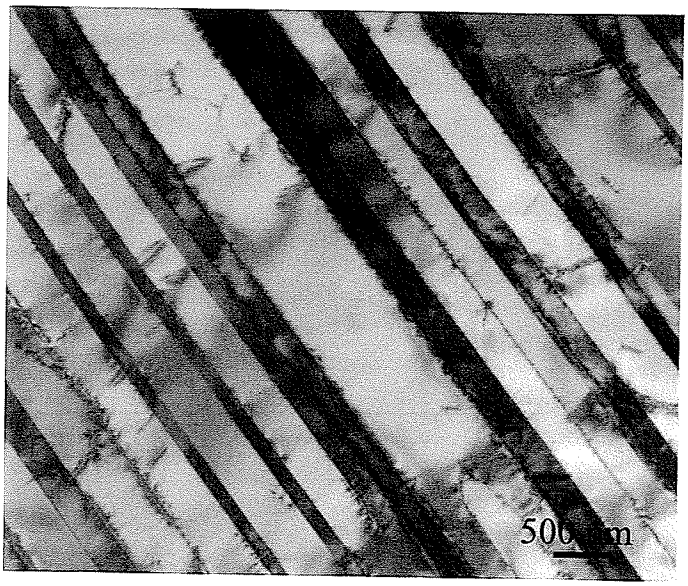

(b)

Figure 4.32: (a) Optical micrograph showing microstructure obtained in alloy III after annealing at 1350°C for 30 minutes followed by furnace cooling; (b) TEM bright field image showing lamellar microstructure in FC sample of alloy III.

Figure 4.33: Optical micrograph showing microstructure of the air-cooled specimen of alloy III.

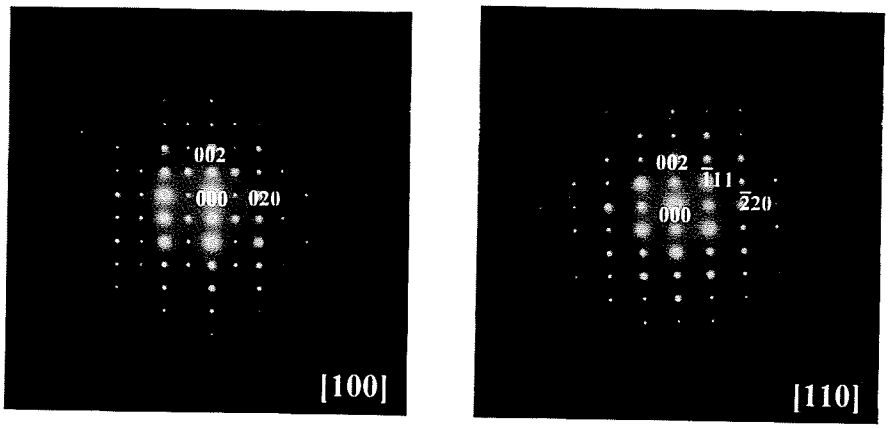

(a) (b)

Figure 4.34: SADP corresponding to the (a) [100] and (b) [110] zone axes of gamma in the air-cooled sample of alloy III.

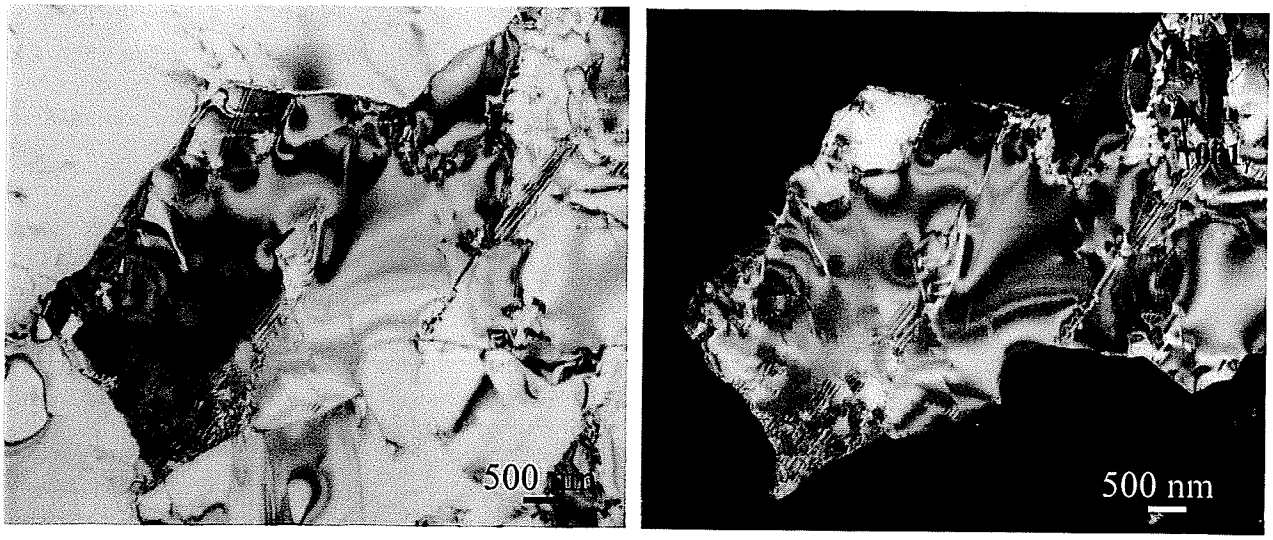

(a) (b)

Figure 4.35: TEM bright field (a) and dark field (b) images revealing the presence of massively transformed gamma in the air-cooled sample of alloy III.

Figure 4.36: Optical micrograph showing the microstructure of the oil-quenched sample of alloy III.

phase was a mixture of mainly γ_m with minor amount of γ_l (Figures 4.37 (a-b)). Figures 4.38 (a-b) show the selected area diffraction patterns (SADP's) corresponding to [101] and [100] zone axes of gamma phase in Figure 4.37b.

Finally, the increase in cooling rate to water quenching (WQ) resulted in a further suppression of the massive transformation by the $\alpha \rightarrow \alpha_2$ transformation. The microstructure consisted of occasional patches of massive gamma in a featureless matrix of alpha-2 phase (Figure 4.39). The volume fraction of the massively transformed gamma was observed to be ~25 %. TEM analysis of thin foils confirmed the presence of massively transformed gamma phase and alpha-2 phase. Figure 4.40a is the bright field image of a representative region showing α_2 and γ_m phase. Figure 4.40b shows an SADP corresponding to $[110]_\gamma$ zone axis. Back-scattered electron imaging of polished section of the WQ sample (Figure 4.41) showed weak contrast between the product phases. The measured compositions of α_2 and γ phase in AC, OQ and WQ samples are given in Table 4.7. As seen, there was no significant difference in the compositions of the two product phases, except for a slightly higher Mn and Al concentrations in γ_m. Nb did not partition between the two phases. Table 4.8 shows the variation in the volume fraction of massively transformed gamma in the microstructure of heat-treated samples with cooling rate.

(a)

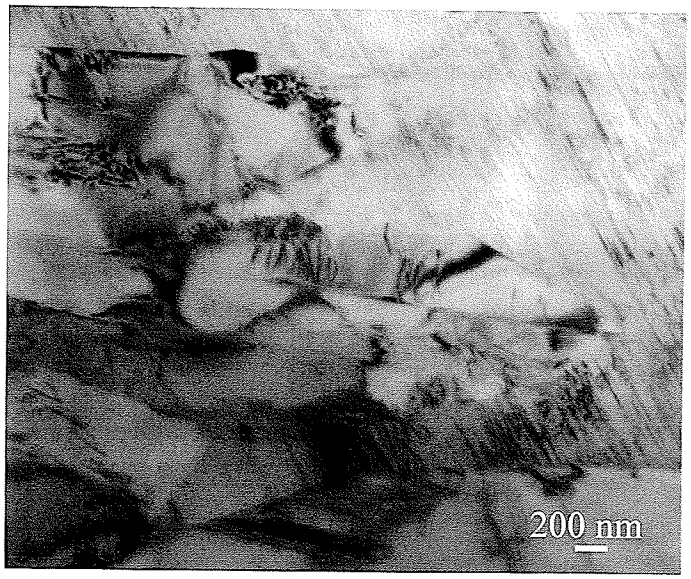

(b)

Figure 4.37 (a-b): TEM bright field images showing the microstructure of the oil quenched sample of alloy III.

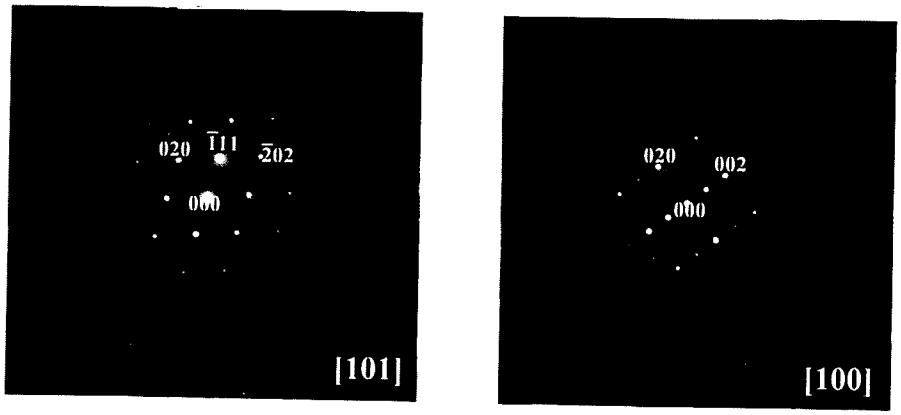

(a) (b)

Figure 4.38: SADP's corresponding to (a) [101] and (b) [100] zone axes of gamma phase.

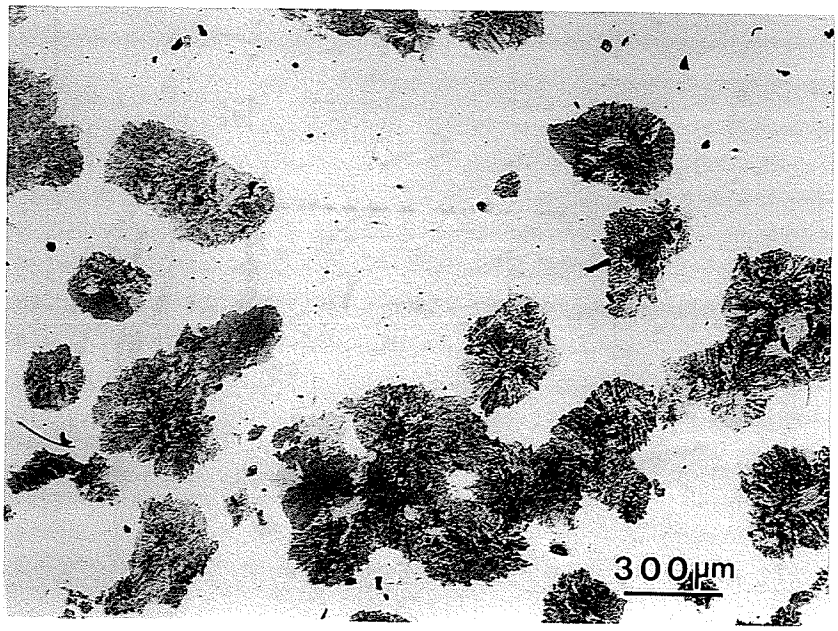

Figure 4.39: Optical micrograph showing the microstructure of the water-quenched sample of alloy III.

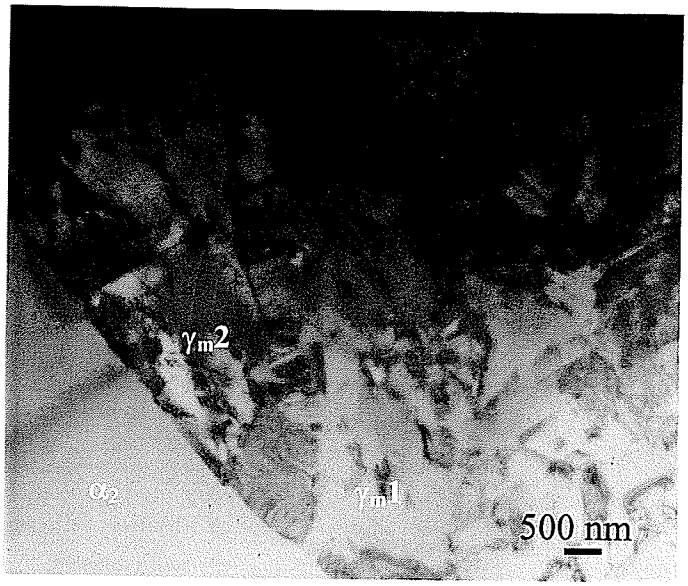

(a)

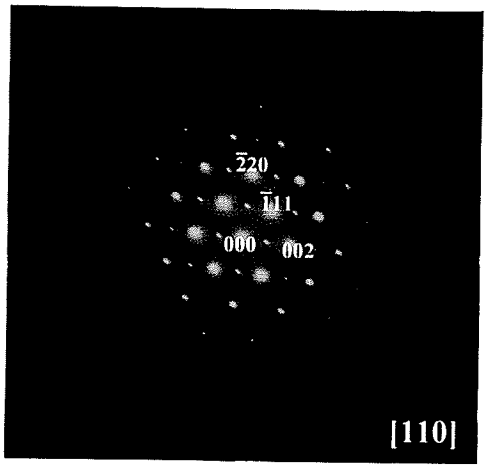

(b)

Figure 4.40: (a) TEM bright field image showing the presence massively transformed gamma and alpha-2 phase. (b) SADP corresponding to [110] zone axis of $\gamma_m 2$.

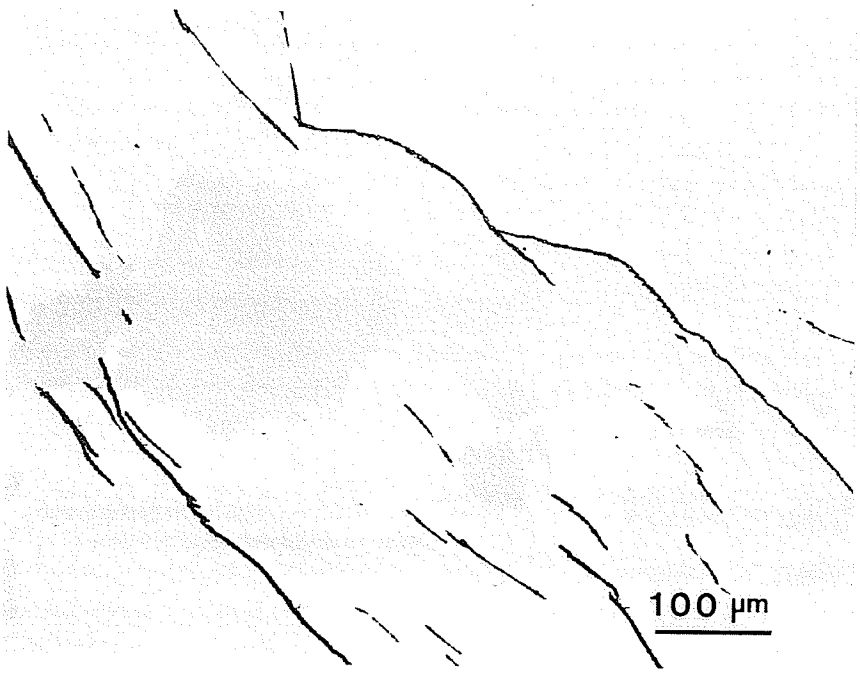

Figure 4.41: SEM back-scattered image of the water-quenched sample of alloy III showing weak composition contrast.

Table 4.7 Composition of different phases in heat treated samples of alloy III

Cooling Rate	Phases	Composition, at.%			
		Al	Mn	Nb	Ti
AC	α_2	45.0	0	2.1	Balance
	γ_m	45.5	0.4	1.9	Balance
OQ	α_2	45.2	0	2.2	Balance
	γ_m	45.4	0.4	2	Balance
WQ	α_2	45.4	0	2.1	Balance
	γ_m	45.4	0.4	1.9	Balance

Table 4.8 Volume fraction of massively transformed gamma in heat-treated samples of alloy III

Cooling rate	V_f of massive γ_m, (%)
AC	100
OQ	90-93
WQ	20-25

4.4.4 Alloy IV (45-2-2)

Furnace cooling (FC) of alloy II to room temperature after annealing at 1350°C for 30 minutes also resulted in a complete decomposition of the high temperature alpha phase and formation of fully transformed lamellar microstructure (Figure 4.42) with an average lamellar colony size of ~ 500 microns.

Increasing the cooling rate to air cooling (AC) from the α-phase field resulted in the formation of a relatively fine lamellar microstructure with dark patches, as shown in Figure 4.43. Figure 4.44a is a TEM bright field image of the air-cooled sample that shows the presence of single-phase region along with the lamellar microstructure. The selected area diffraction patterns (SADP) from the single-phase region, shown in Figure 4.44(b-c), conformed well to [111] and [101] zone axis, respectively, of the ordered tetragonal crystal structure. Figure 4.44d is a dark field image confirming the presence of gamma phase along with lamellar region. The dark patches in Figure 4.43 were therefore identified to be of γ-phase.

A further increase in the cooling rate to oil quenching (OQ) caused the occurrence of massive type transformation in the bulk of the specimen (Figure 4.45a). Thus, the cooling rate required for the initiation of massive transformation in alloy IV was observed to be higher as compared to the other three alloys. Some fine lamellae were also found along with γ_m and an occasional presence of untransformed α_2-phase (Figure 4.45b). TEM analysis of thin foils of OQ samples revealed the microstructure to consist of clusters of massively transformed gamma along with fine lamellae and small amounts of α_2-phase

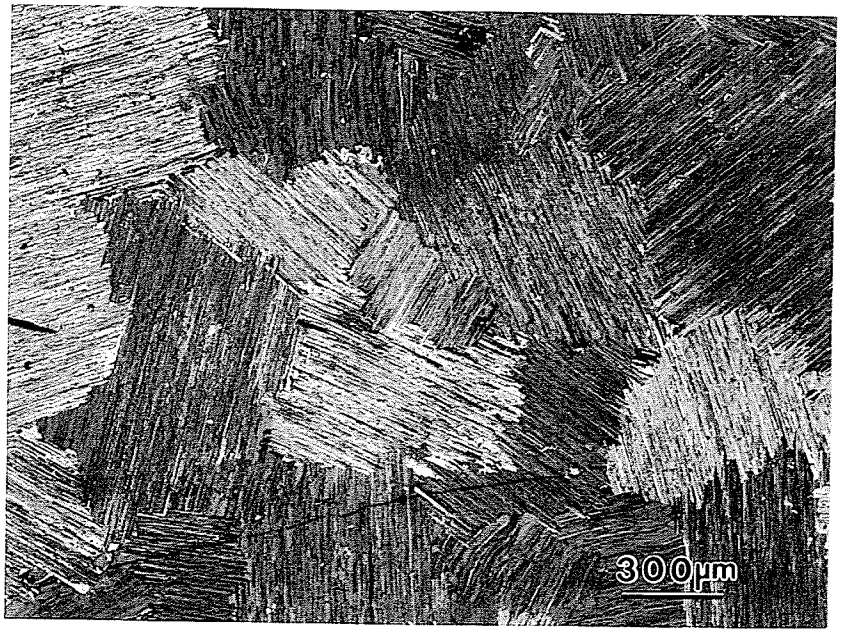

Figure 4.42: Optical micrograph showing microstructure obtained in alloy IV after annealing at 1350°C for 30 minutes followed by furnace cooling.

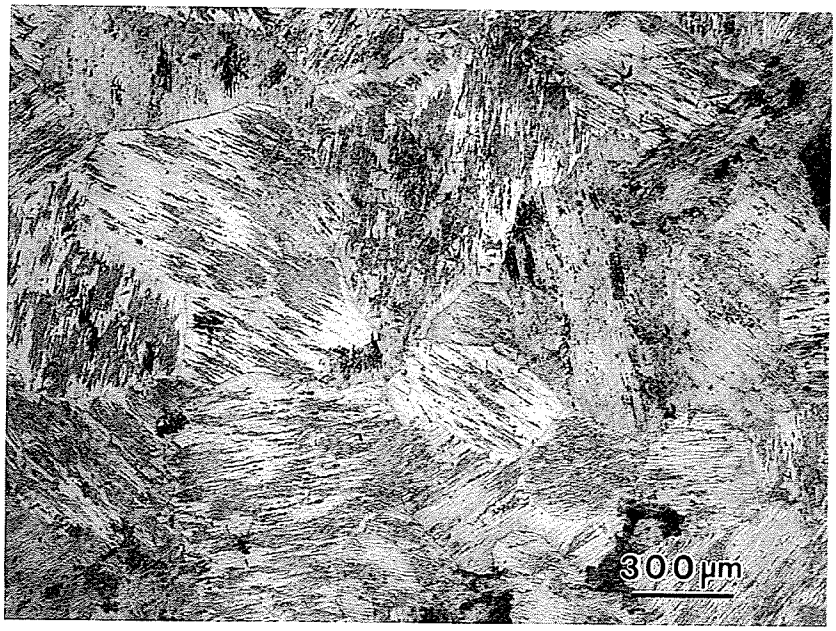

Figure 4.43: Optical micrograph showing microstructure of the air-cooled specimen of alloy IV.

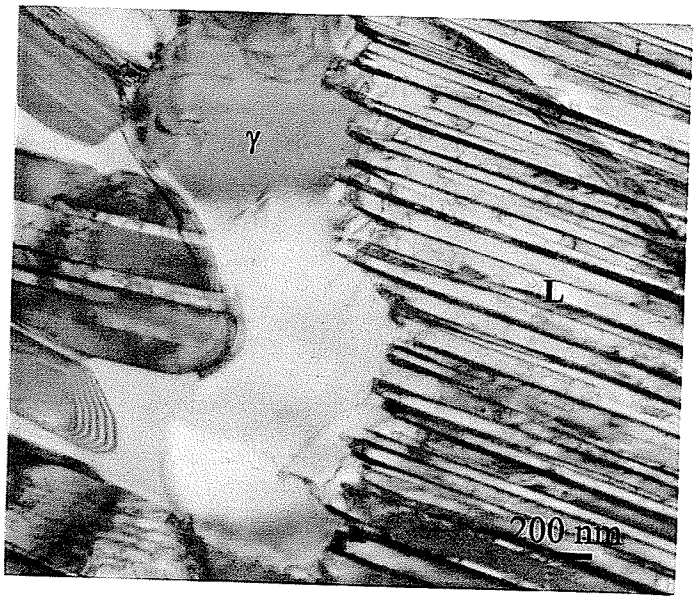

(a)

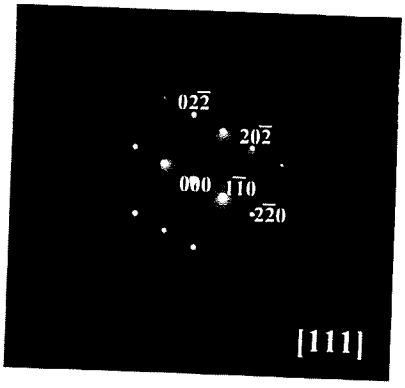

(b)

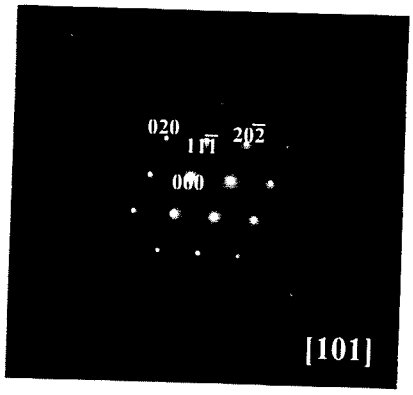

(c)

Figure 4.44 (continued...)

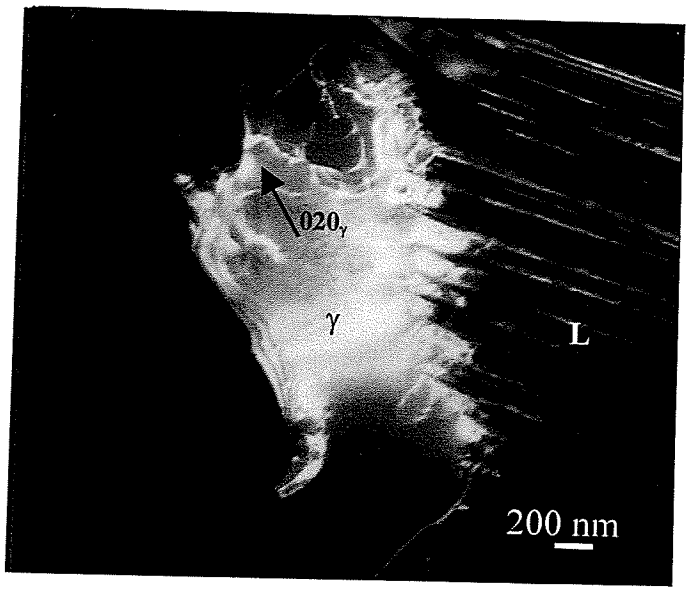

(d)

Figure 4.44: (a) TEM bright field image showing fine lamellae and blocky gamma phase in air-cooled sample of alloy IV. SADP's corresponding to (b) [111] and (c) [101] zone axes of the gamma phase. (d) TEM dark field image taken with g ~ (020) and B ~ [101] confirming the presence of gamma phase.

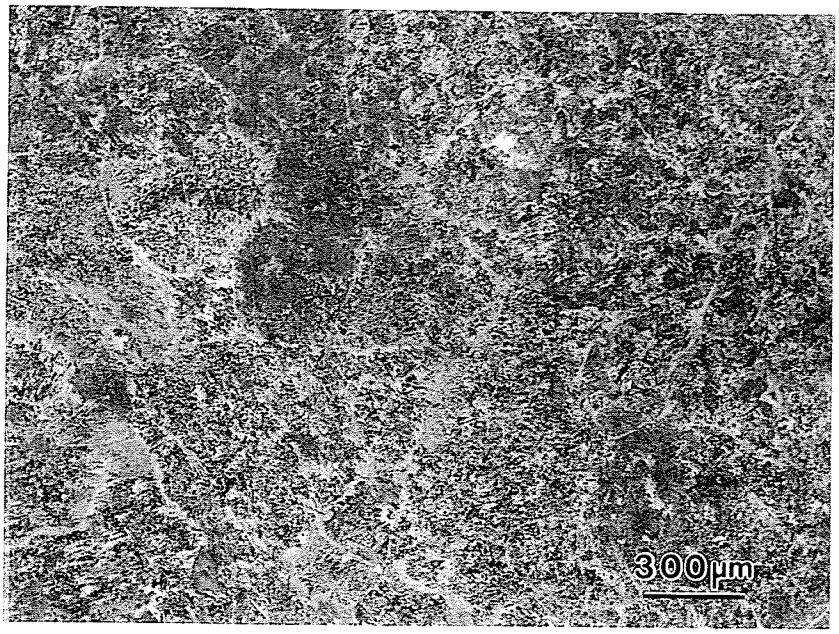

(a)

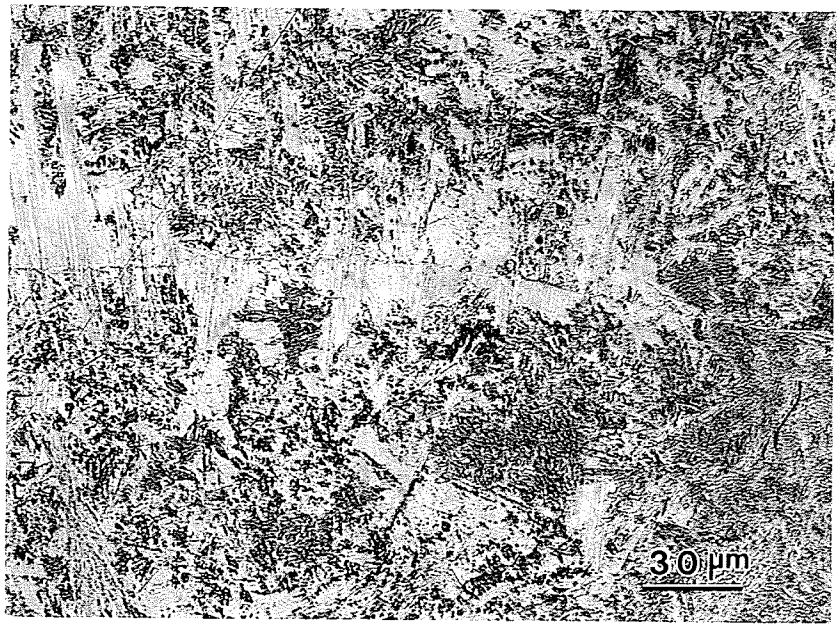

(b)

Figure 4.45: Optical micrographs showing the microstructure of the oil-quenched sample of alloy IV ((a) 50X and (b) 500X).

(Figure 4.46). Figure 4.47a is a bright field image showing cluster of γ_m grains in OQ sample. Figure 4.47b is an SADP taken from one of the γ_m grain ($\gamma_m 1$) in Figure 4.47a, conforming well to $[110]_\gamma$ zone axis.

At a very high cooling rate, viz. WQ, the microstructure consisted primarily of massively transformed gamma (dark etched regions) and patches of α_2-phase (white regions), as shown in Figure 4.48(a-b). γ_m phase was found near the grain boundaries as well as inside the prior α-grains. The $\alpha \rightarrow \gamma_m$ transformation was only partially suppressed by the $\alpha \rightarrow \alpha_2$ ordering reaction and the volume fraction of massively transformed gamma was observed to be ~70 %. Figure 4.49 shows an SADP corresponding to $[110]_\gamma$ zone axis. Figures 4.50 (a-b) show a pair of TEM bright field and dark field image confirming the presence of massively transformed gamma. The microstructure consisted of large patches of γ_m grains along with α_2 phase, as shown in the collage in Figure 4.51. No fine lamellae were observed. Back-scattered electron imaging of polished section of the WQ sample (Figure 4.52) showed weak contrast between the product phases. The measured compositions of α_2 and γ phase in AC, OQ and WQ samples are given in Table 4.9. As seen, there was no significant difference in the compositions of the two product phases, except for a slightly higher Mn and Al concentrations in γ_m. Nb did not partition between the two phases. Table 4.10 lists the volume fraction of γ_m in the microstructure of heat-treated specimens as a function of cooling rate.

Figure 4.46: TEM bright field image showing the microstructure of oil-quenched specimen of alloy consisting of massively transformed gamma phase, fine lamellar region and alpha-2 phase.

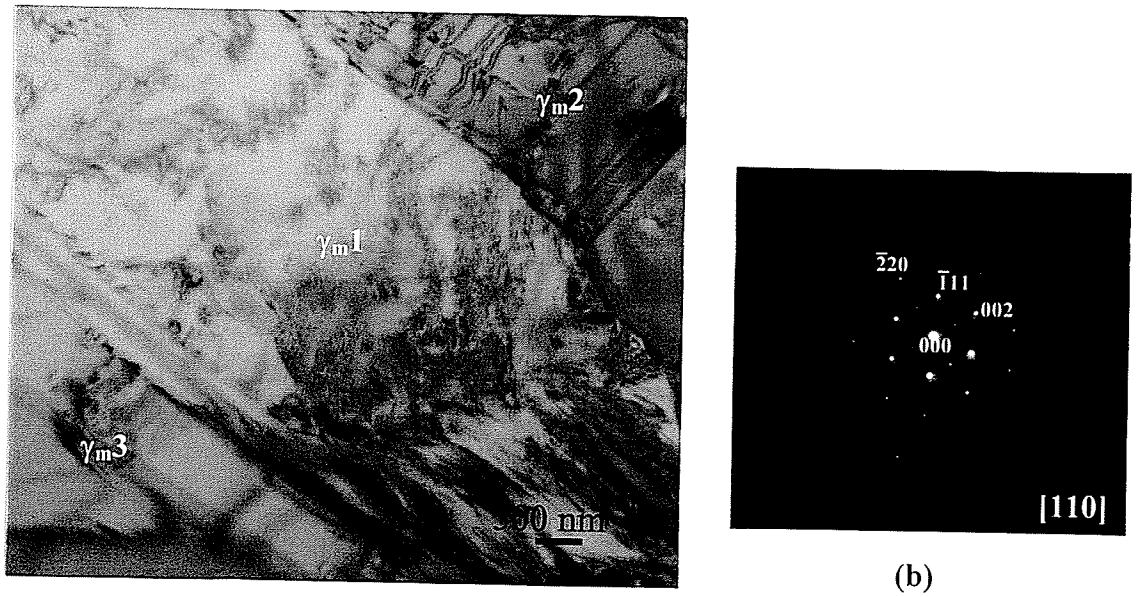

(a) (b)

Figure 4.47: (a) TEM bright field image showing a cluster of massively transformed grains in oil-quenched sample of alloy IV. (b) SADP corresponding to [110] zone axis of the gamma phase labeled γ_m1.

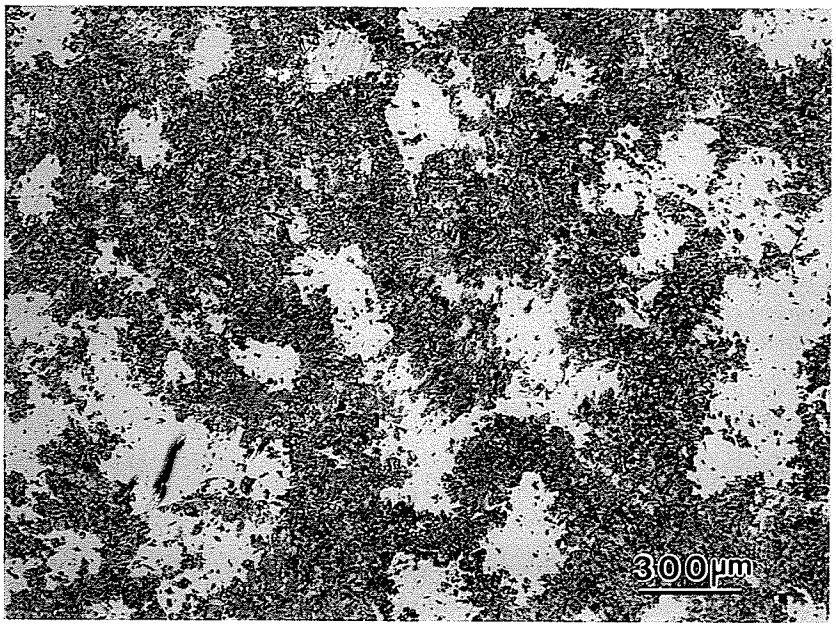

(a)

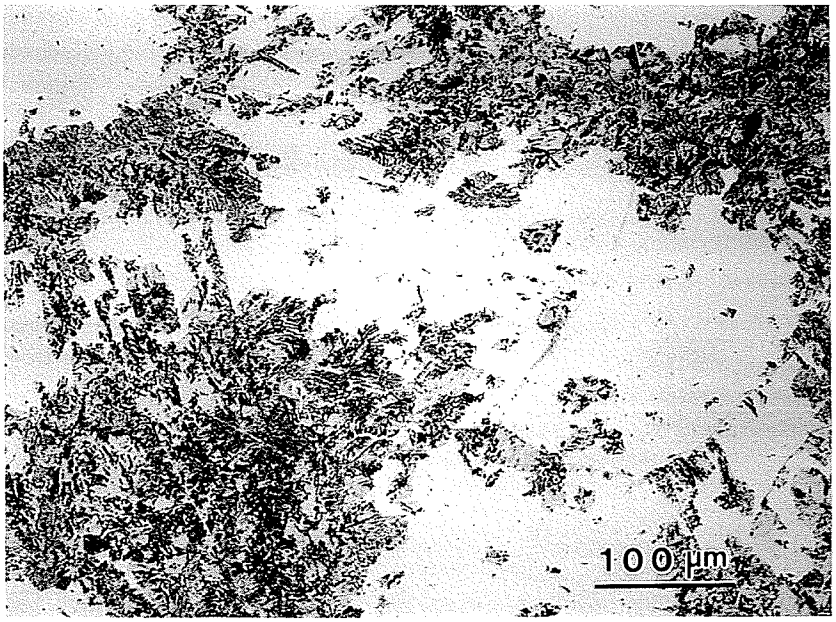

(b)

Figure 4.48: Optical micrographs showing the microstructure of the water-quenched sample of alloy IV ((a) 50X and (b) 200X).

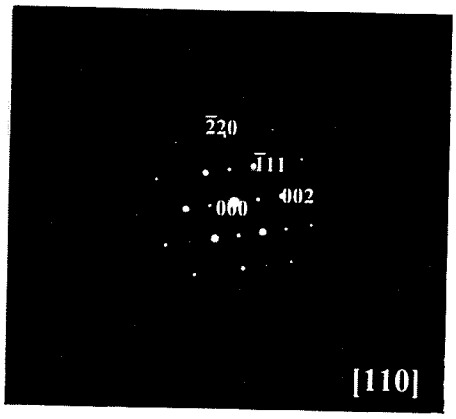

Figure 4.49: SADP corresponding to [110] zone axis of the massively transformed gamma phase in water-quenched sample of alloy IV.

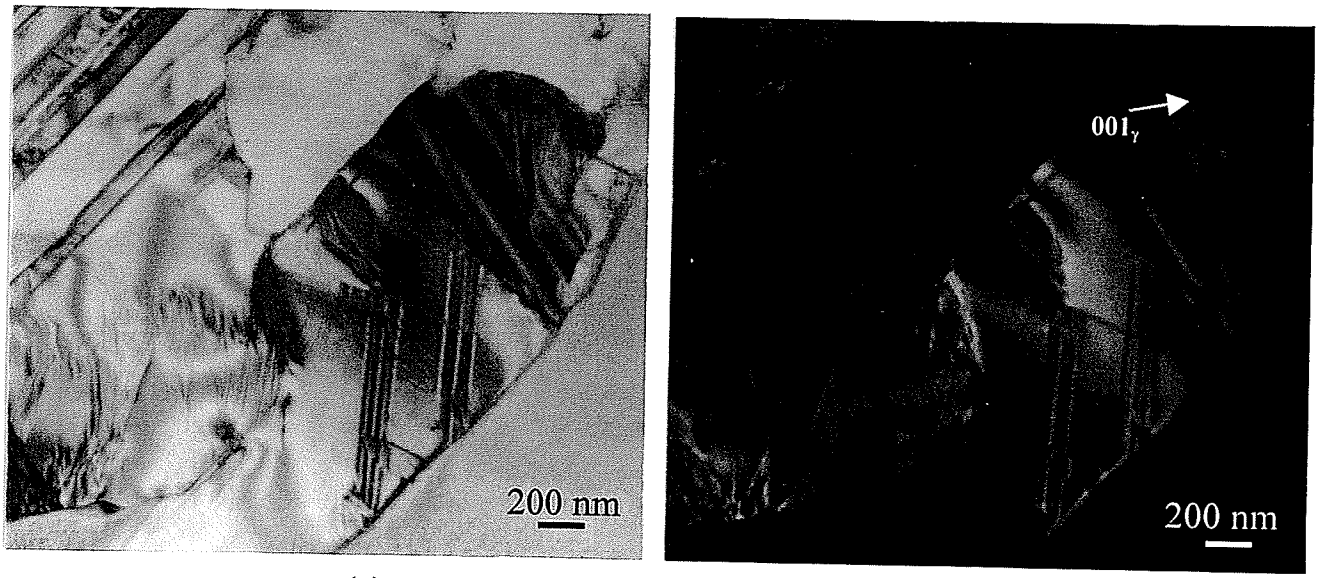

(a) (b)

Figure 4.50: TEM bright field (a) and dark field (b) image confirming the presence of massively transformed gamma in water-quenched sample of alloy IV. g ~ (001), B ~ [110].

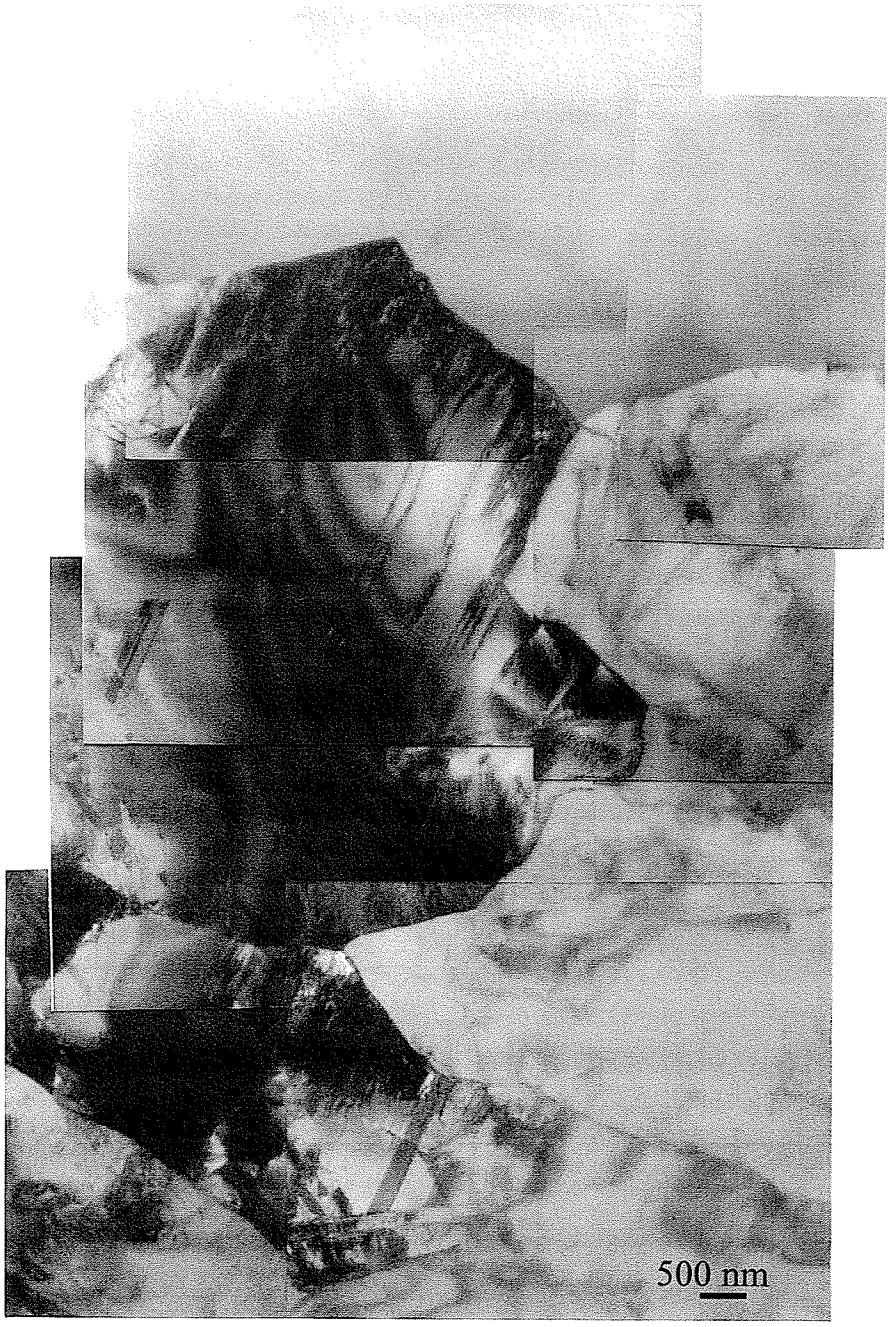

Figure 4.51: A collage of TEM bright field images revealing the overall microstructure of the water-quenched sample of alloy IV.

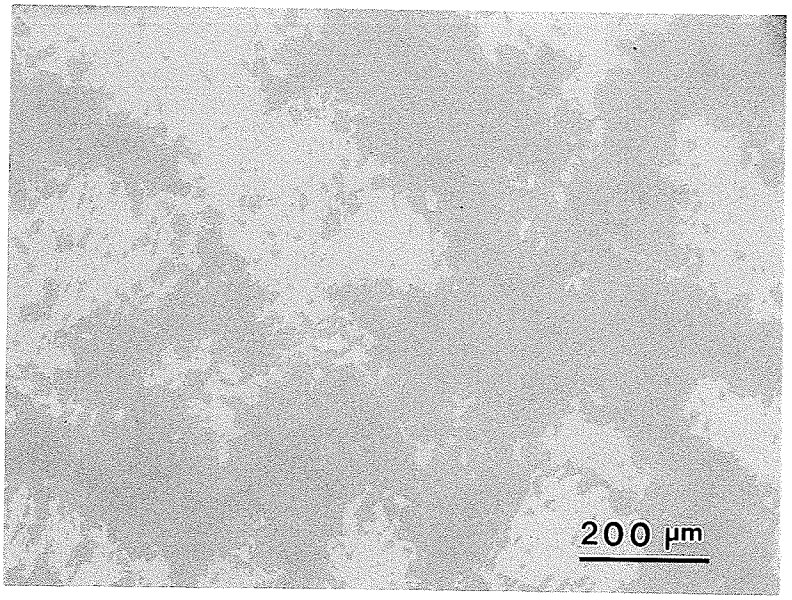

Figure 4.52: SEM back-scattered image of the water-quenched sample of alloy IV showing weak composition contrast.

Table 4.9 Composition of different phases in heat treated samples of alloy IV

Cooling Rate	Phases	Composition, at.%			
		Al	Mn	Nb	Ti
AC	L	45.3	1.5	2	Balance
	γ	45.5	1.6	2	Balance
OQ	$\alpha_2+\gamma(L)$	44.9	1.5	2	Balance
	γ_m	44.9	1.5	2	Balance
WQ	α_2	45	1.5	2	Balance
	γ_m	45.5	1.8	2	Balance

Table 4.10 Volume fraction of massively transformed gamma in heat-treated samples of alloy IV

Cooling rate	V_f of massive γ_m, (%)
AC	-
OQ	-
WQ	~70

4.5 GRAIN GROWTH AND MASSIVE TRANSFORMATION

The effect of grain size on massive transformation was studied using alloy III (Ti-45Al-2Nb-0.4Mn). Small samples of alloy III were annealed at 1350°C for 30, 90, and 150 minutes and were subsequently cooled by furnace cooling (FC) and by ice water quenching (IWQ). Figure 4.53 (a-c) shows the microstructures obtained upon furnace cooling. As seen, fully transformed lamellar microstructure was observed in all the three samples. The grain size, however, increased with increase in annealing time. Table 4.11 lists the grain size (lamellar colony size) as a function of annealing time. It was also observed that the grain boundaries become increasingly planar with increase in annealing time. Ice water quenching (IWQ) from 1350°C resulted in a significant change in microstructure. Figure 4.54 (a-c) show the optical micrographs of the ice water quenched samples in which the dark etched regions are massively transformed gamma and the white region is the alpha-2 phase. As seen in these micrographs, the volume fraction of the massively transformed gamma decreased as the annealing time increased. The volume fractions of γ_m in the IWQ samples were quantitatively measured by the technique described in section 3.3.2, and the values obtained are provided in Table 4.12. As seen, the volume fraction of massively transformed gamma decreased with increase in annealing time.

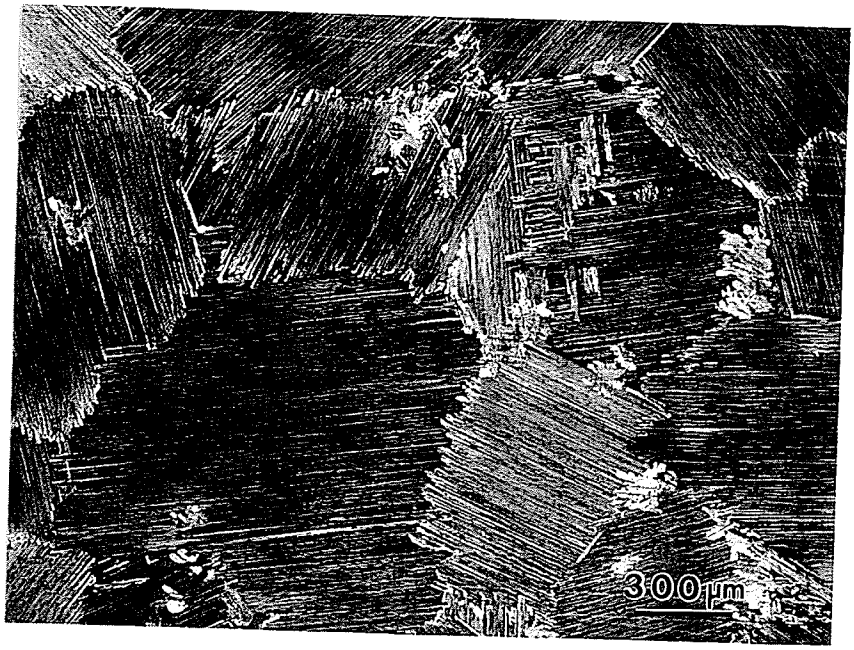

(a)

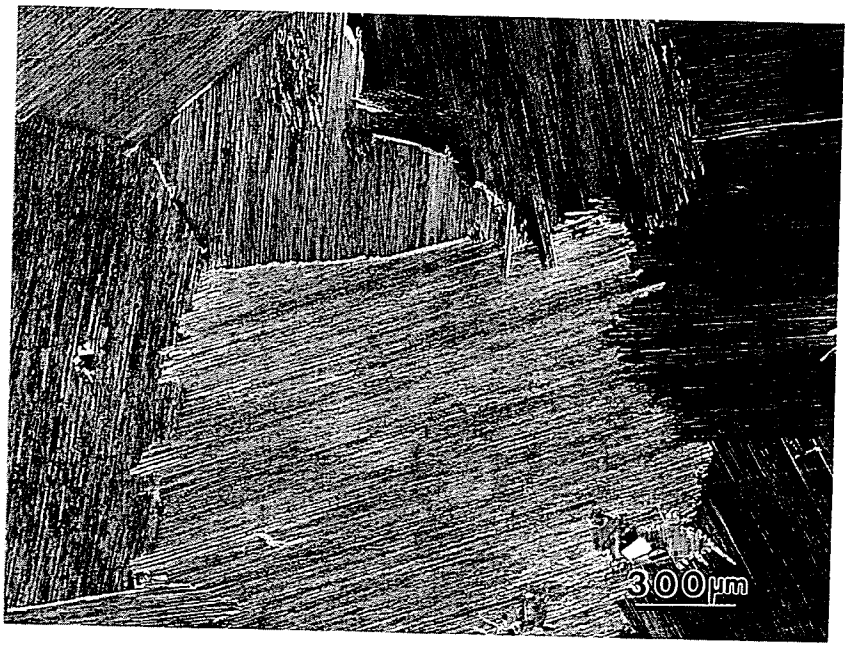

(b)

Figure 4.53 (continued...)

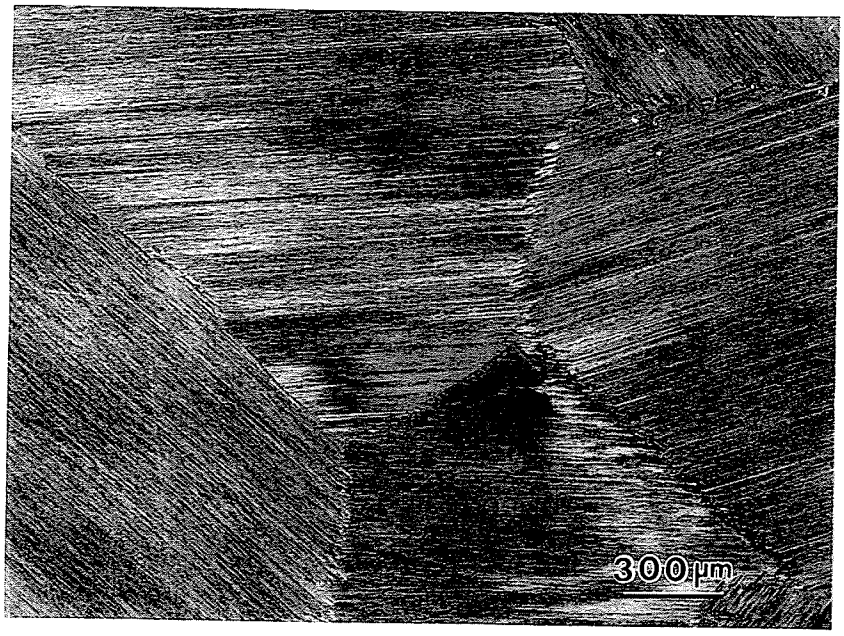

(c)

Figure 4.53: Optical micrographs showing the variation in grain size of alloy III with annealing time after annealing at 1350°C for (a) 30, (b) 90 and (c) 150 minutes.

Table 4.11 Variation of grain size (lamellar colony size) with annealing time at 1350°C

Annealing time, (min)	Grain size, (mm)	Standard deviation
30	0.761	0.159
90	1.186	0.35
150	1.7124	0.415

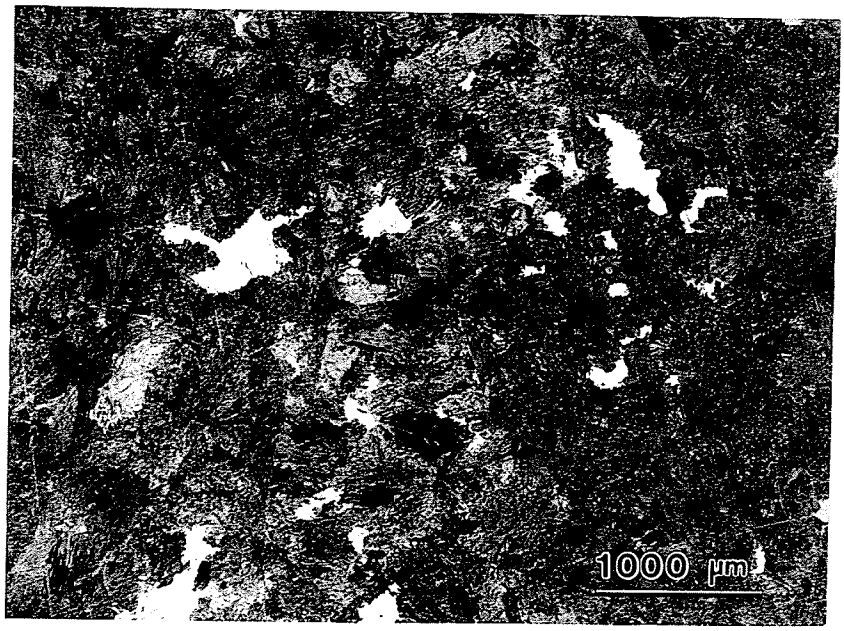

(a)

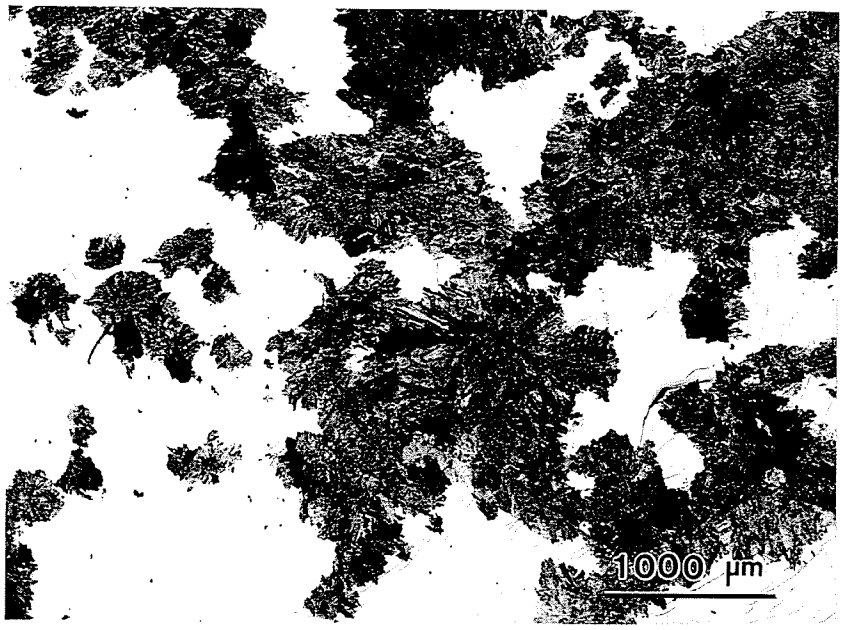

(b)

Figure 4.54 (continued...)

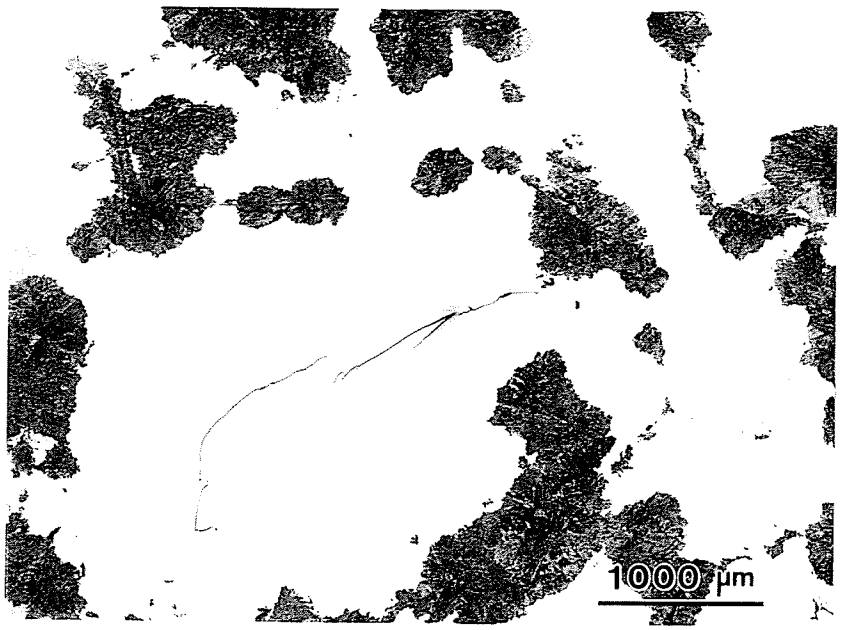

(c)

Figure 4.54: Optical micrographs of samples of alloy III wrapped in Ta-foil and heated at 1350°C for (a) 30, (b) 90 and (c) 150 minutes followed by ice water quenching (IWQ).

Table 4.12 Variation of volume fraction of massively transformed gamma with annealing time at 1350°C in alloy III

Annealing time, (min)	V_f of massive gamma, (%)
30	90-93
90	50-55
150	25-30

4.6 GRAIN GROWTH AT 1350°C AND SUBSEQUENT LAMELLAR STRUCTURE FORMATION

4.6.1 Alloy III

The phenomenon of grain growth and the effect of annealing time/prior grain size on subsequent lamellar structure formation was studied by annealing samples of alloy III at 1350°C for various time periods ranging from 15 minutes to 240 minutes. The samples were furnace cooled from 1350°C to ~800°C. Subsequently, the samples were withdrawn from the furnace and air-cooled to room temperature. Figures 4.55 (a-g) represent the microstructures of the furnace-cooled samples. As seen from the micrographs, the microstructures were fully lamellar and the lamellar colony size increased with increasing annealing time suggesting rapid grain growth in the alpha phase field. The average grain size (lamellar colony size) was measured by the technique/methodology illustrated in section 3.3.1. The variation of the lamellar colony size with annealing time is listed in Table 4.13. The average colony size was observed to vary from ~ 490 microns after 15 minutes annealing time to ~ 2500 microns after 240 minutes annealing time.

Higher magnification examination of the specimen annealed for 15 minutes (Figure 4.56a), also indicated the presence of remnant prior lamellae. This suggests that 15 minutes of annealing time is insufficient for a complete dissolution of prior lamellae i.e. for homogenization during annealing at 1350°C. However, increasing the annealing time

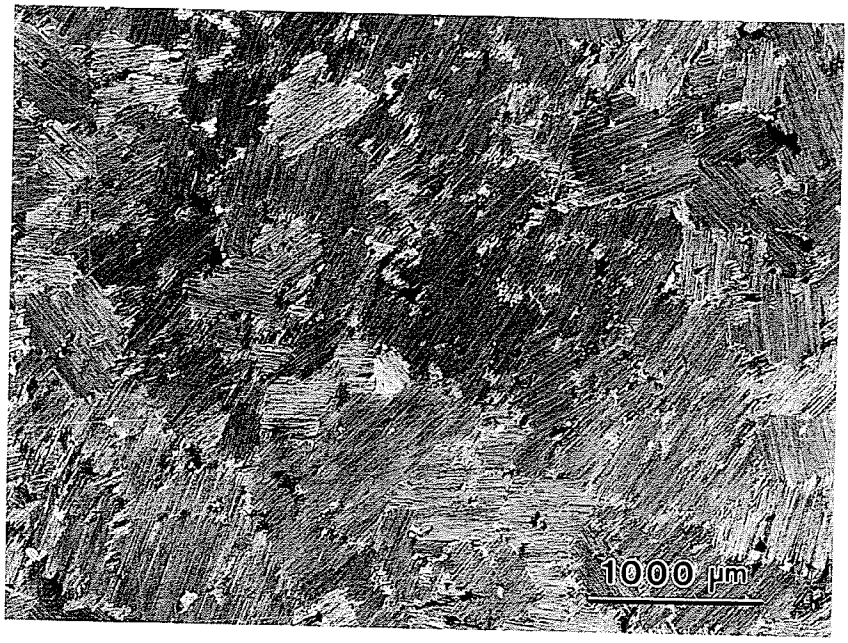

(a)

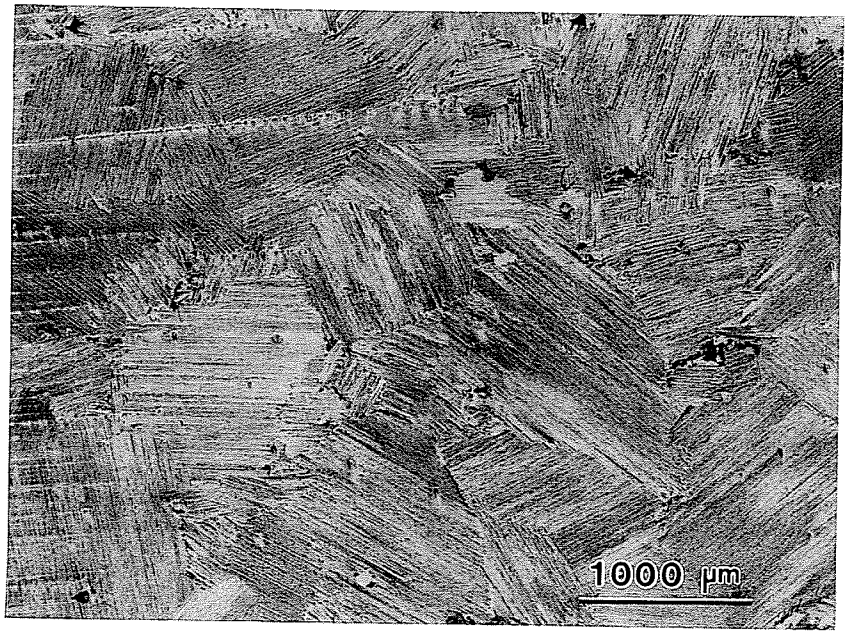

(b)

Figure 4.55 (continued...)

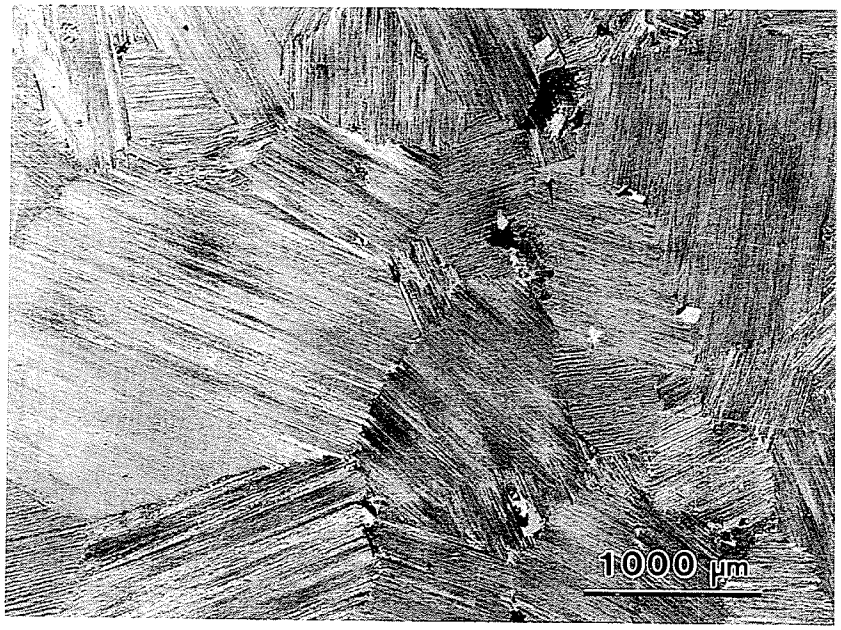

(c)

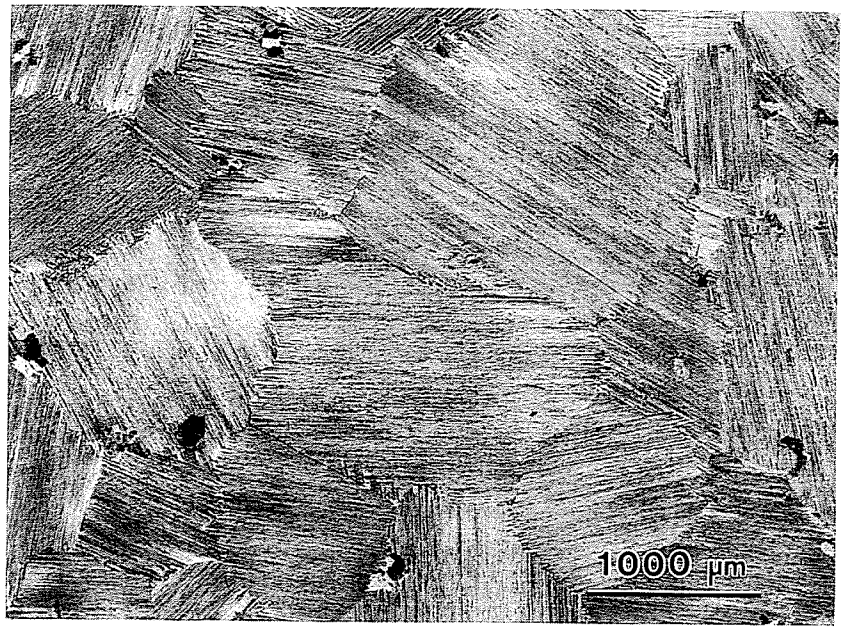

(d)

Figure 4.55 (continued...)

(e)

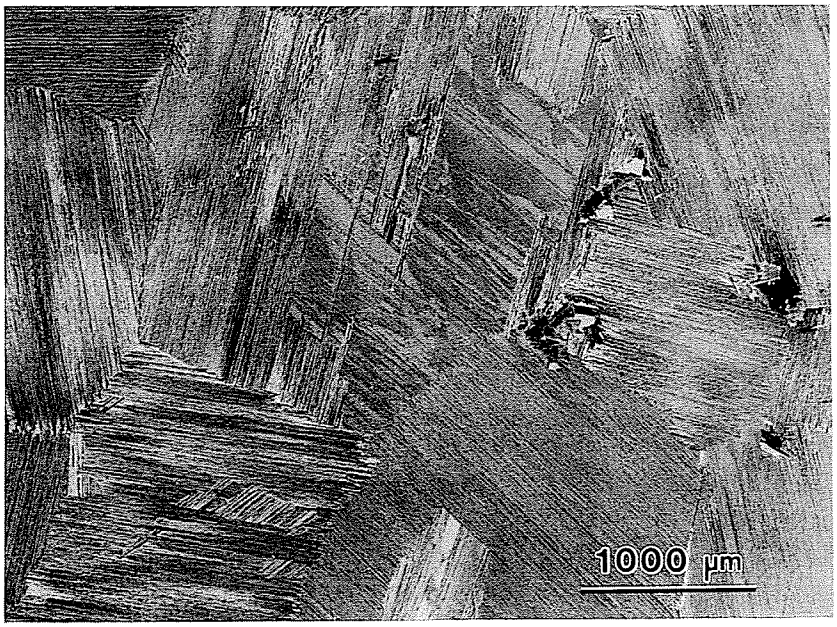

(f)

Figure 4.55 (continued...)

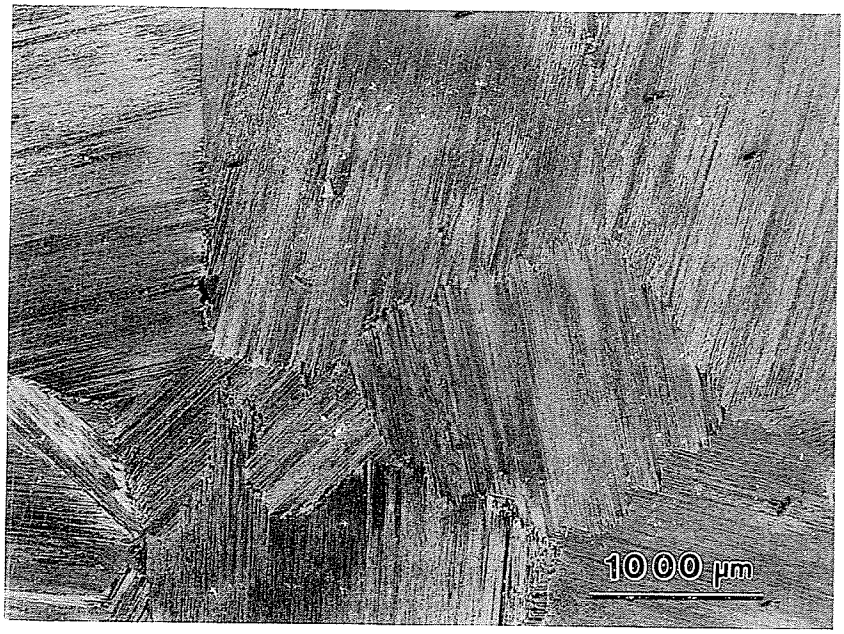

(g)

Figure 4.55: Optical micrographs showing the variation in grain size in the FC samples of alloy III with annealing time after annealing at 1350°C for (a) 15, (b) 30, (c) 60, (d) 90, (e) 120, (f) 150 and (g) 240 minutes.

Table 4.13 Grain size data of alloy III

Annealing time, min	Grain size, microns	Standard deviation
15	490	106
30	783	114
60	1061	188
90	1057	177
120	1587	440
150	1721	362
240	2347	940

to 30 minutes resulted in a profound reduction in remnant prior lamellae. All the prior lamellae were almost completely dissolved except for an occasional presence of prior lamellae near some grain boundaries (Figure 4.56b). Further increase in annealing time eliminated all the prior lamellae. The total time required for complete dissolution of prior lamellar grains and formation of single-phase alpha at 1350°C was estimated to be ~ 30 minutes for the present alloy. It was also observed that short annealing times resulted in interlocked lamellar grain boundaries. The grain boundaries/ lamellar colony boundaries, however, became increasingly planar with increasing annealing time (Figure 4.55).

The effect of annealing time/grain size on the interlamellar spacing was studied by TEM examination. Figures 4.57 (a-d) are the bright field images showing the lamellar microconstituents in samples annealed for 30, 90, 120 and 150 minutes. It is seen from the figures that the interlamellar spacing increased with annealing time. To determine the interlamellar spacing in specimens annealed at 1350°C for different lengths of time, the thin foils were carefully tilted to orient the lamellae edge-on ($[110]_\gamma$ parallel to the electron beam direction). The interlamellar spacing was then measured by linear intercept method. Table 4.14 lists the values of interlamellar spacing as a function of annealing time. This data are graphically represented in Figure 4.58. It is seen that with an increase in annealing time at 1350°C, the value of interlamellar spacing increases.

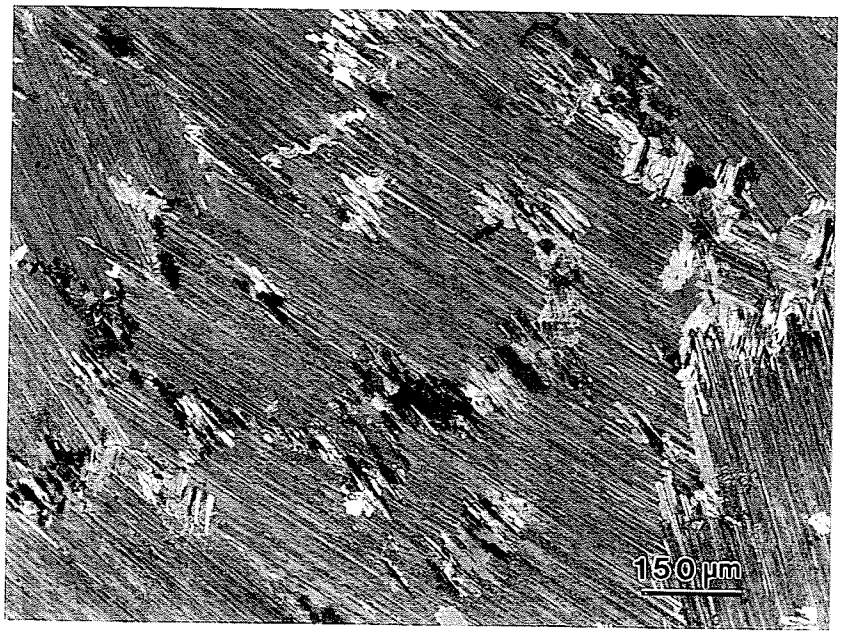

(a)

(b)

Figure 4.56: Higher magnification (100X) optical micrographs of samples of alloy III after annealing at 1350°C for (a) 15 and (b) 30 minutes.

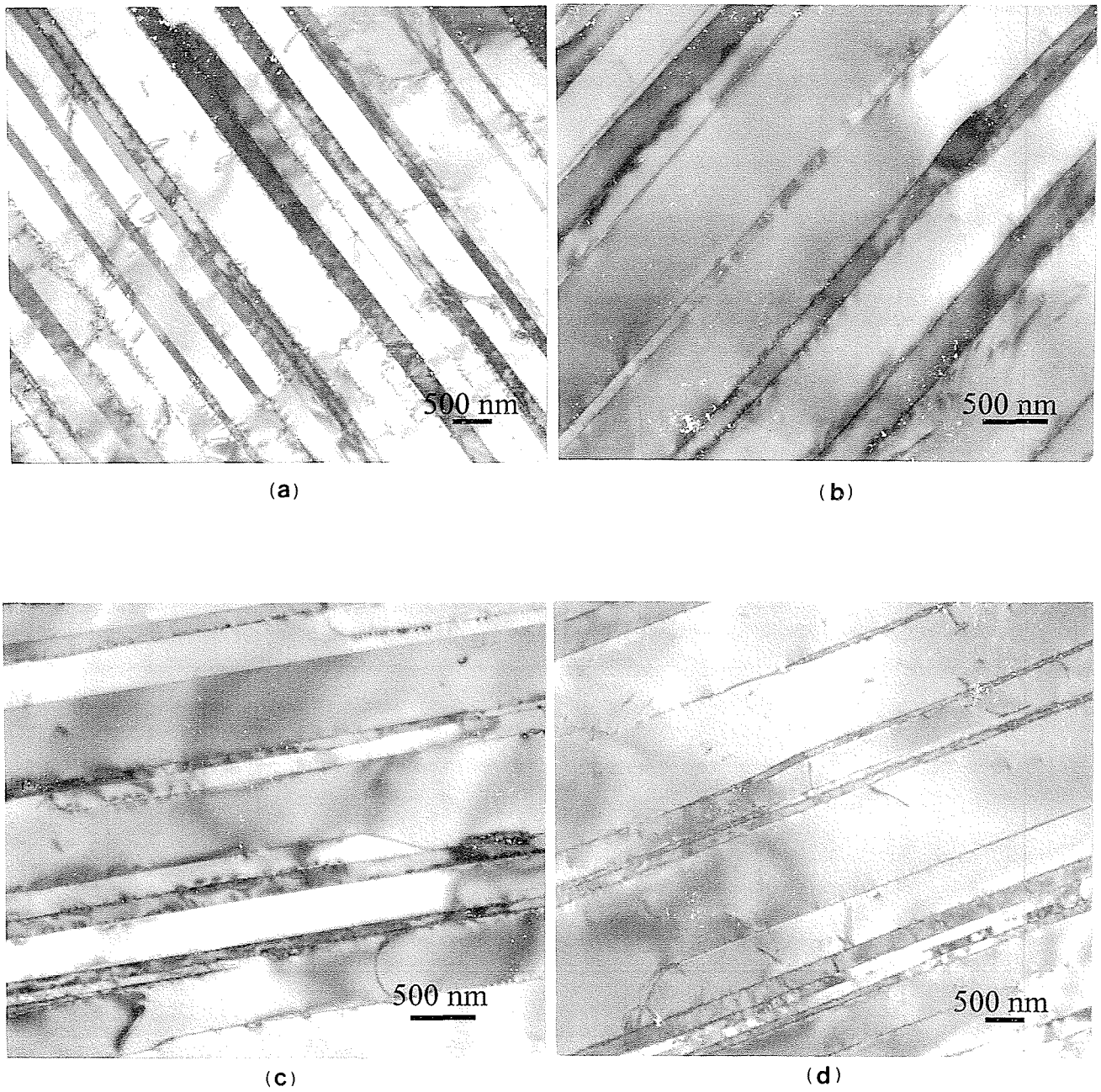

Figure 4.57: TEM bright images showing the variation in interlamellar spacing in the FC samples of alloy III with annealing time after annealing at 1350°C for (a) 30, (b) 90, (c) 120 and (d) 150 minutes. (B ~ [110])

Table 4.14 Variation of interlamellar spacing with annealing time.

Annealing time, (min)	Interlamellar spacing, (microns)
30	0.59
90	0.62
120	0.79
150	0.697
240	1.13

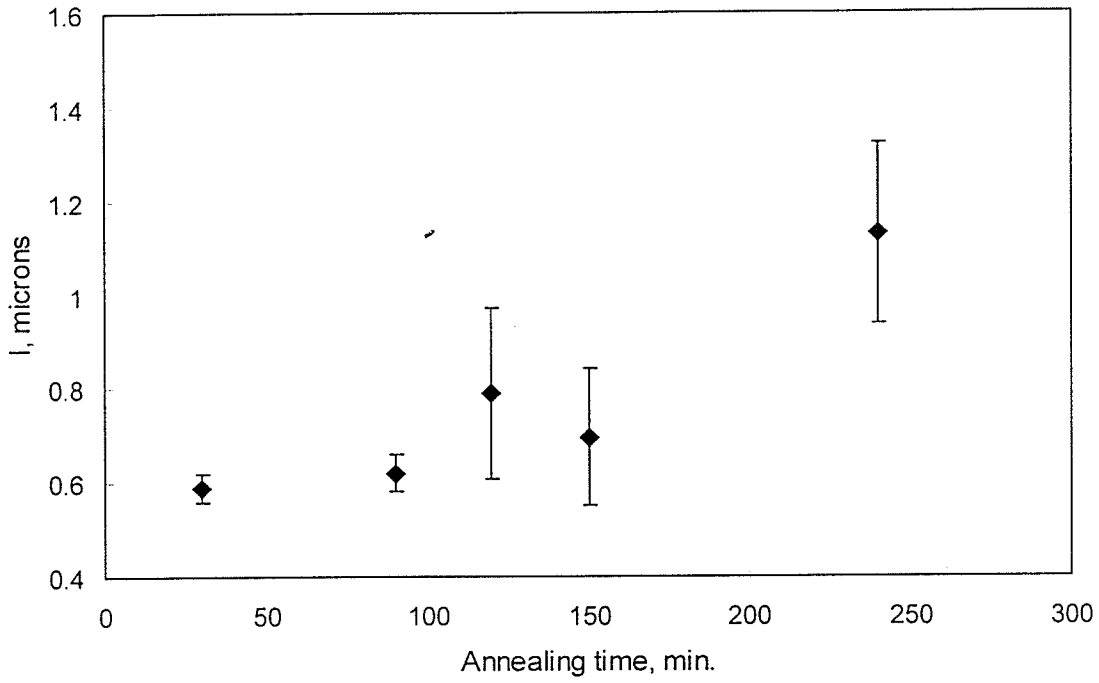

Figure 4.58: Graph of interlamellar spacing versus annealing time at 1350°C.

4.6.2 Alloy II

Small samples of alloy II were also annealed at 1350°C for various lengths of time ranging from 15 minutes to 240 minutes to study the phenomenon of grain growth in the alpha phase field in this alloy. The samples were furnace cooled from 1350°C to ~800°C and subsequently, air-cooled to room temperature. Figures 4.59 (a-g) show the optical micrographs of the cross section of the furnace-cooled samples. Once again, as seen from the figures, the microstructures obtained were fully lamellar and the lamellar colony size increased with increase in annealing time. Table 4.15 lists the measured average grain size (lamellar colony size) as a function of annealing time. The lamellar colony size increased from ~ 1000 microns for 15 minutes to ~ 2800 microns for 240 minutes.

4.7 MICROSTRUCTURAL EVOLUTION DURING CONTROLLED COOLING FROM 1350°C

In one of the experiments, small sample (10mm x 6mm x 6 mm) of alloy IV (Ti-45Al-2Nb-2Mn) was heated in the α-phase field (1350°C) for 30 minutes and subsequently cooled to room temperature by a two step cooling process. The sample was furnace cooled from 1350°C to 1150°C and then rapidly air-cooled to room temperature. The resulting microstructure was fully lamellar with a grain size of ~150 microns (Figure 4.60). As described in section 4.4.4, furnace cooling of similar sample resulted in a fully lamellar microstructure with an average colony size of ~ 500 microns.

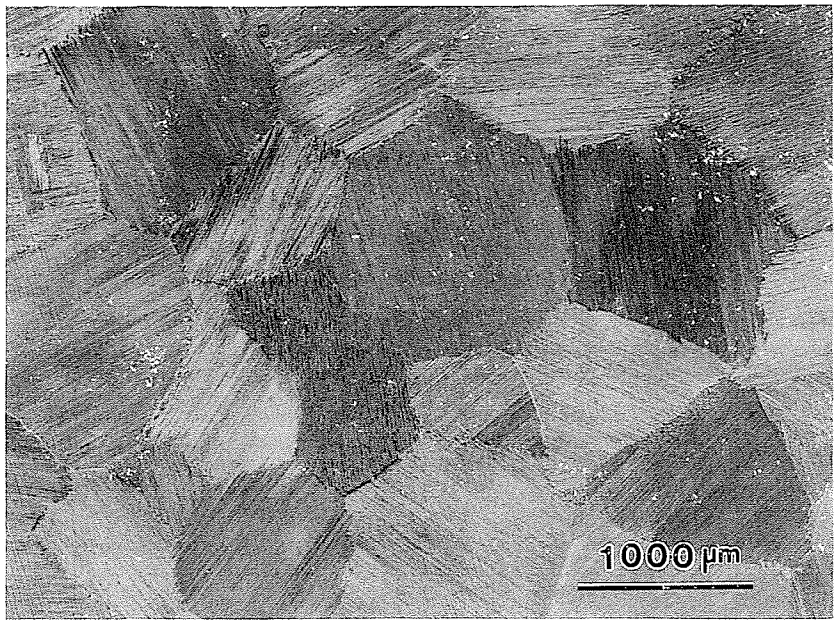

(a)

(b)

Figure 4.59 (continued...)

(c)

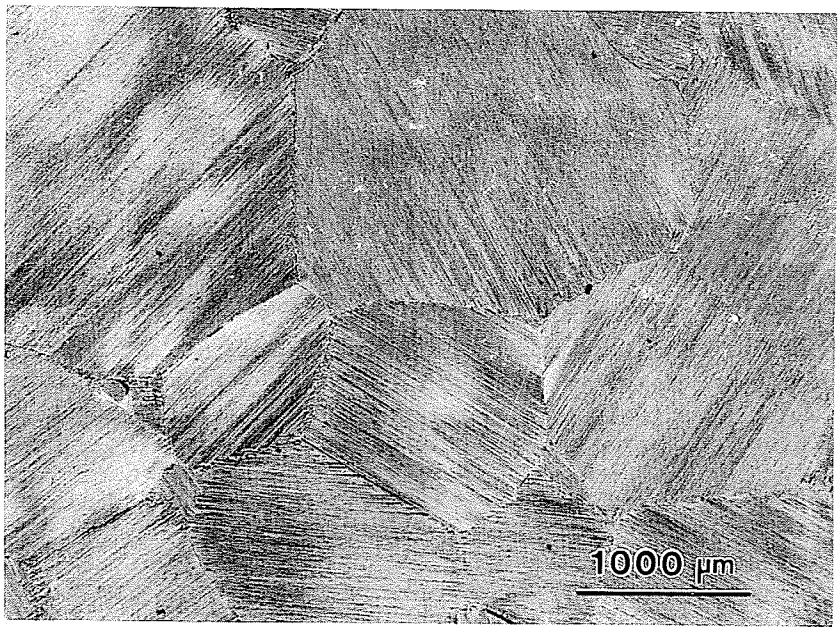

(d)

Figure 4.59 (continued...)

(e)

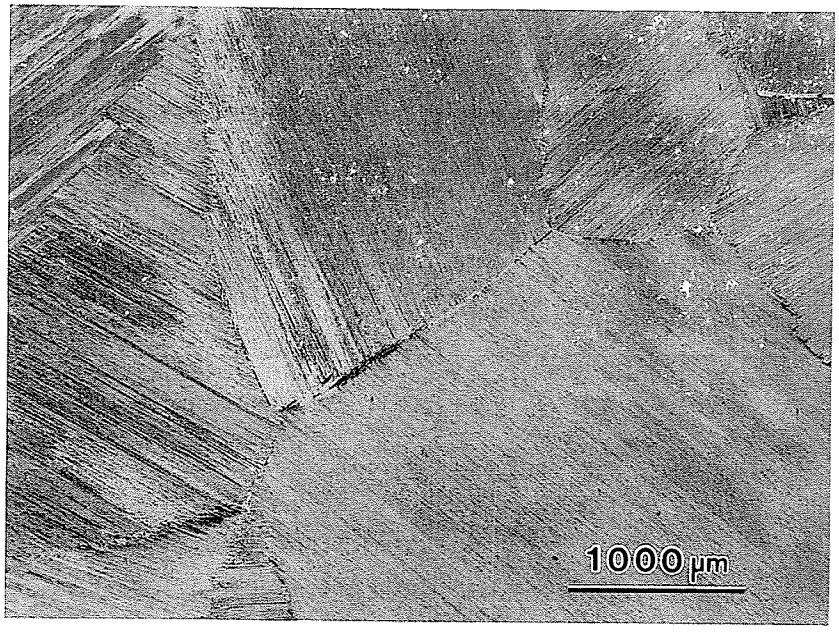

(f)

Figure 4.59 (continued...)

(g)

Figure 4.59: Optical micrographs showing the variation in grain size in the FC samples of alloy II with annealing time after annealing at 1350°C for (a) 15, (b) 30, (c) 60, (d) 90, (e) 120, (f) 150 and (g) 240 minutes.

Table 4.15 Grain size data of alloy II

Annealing time, min	Grain size, microns	Standard deviation
15	1014	143
30	1112	297
60	1391	366
90	1646	359
120	1889	474
150	2300	849
240	2784	1129

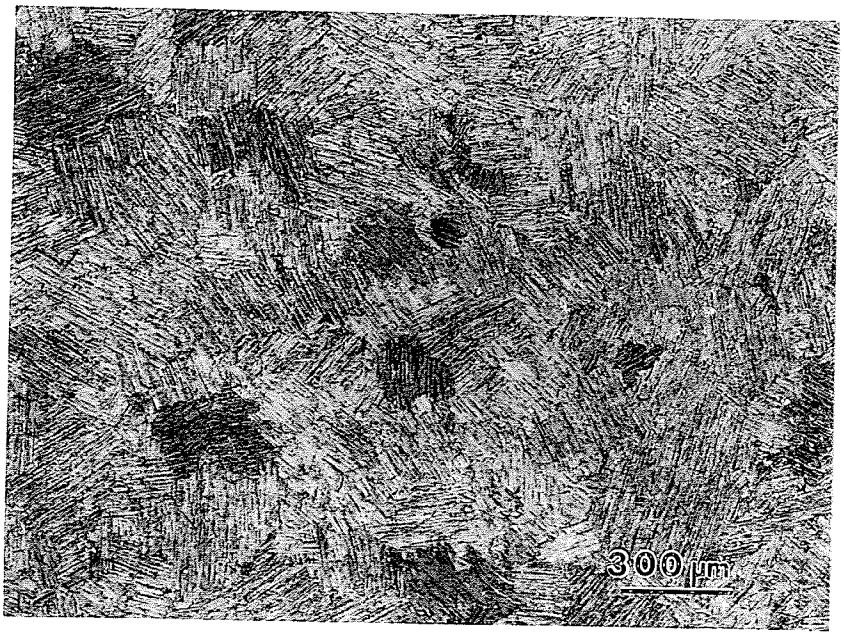

Figure 4.60: Optical micrograph showing fine lamellar microstructure in alloy IV obtained by two step cooling after annealing at 1350°C for 30 minutes.

4.8 HARDNESS OF HEAT TREATED SPECIMENS

The Vickers pyramid hardness (VPH) of the cross-sections of the heat-treated specimens were measured on Vickers hardness tester using a load of 10 Kilos. The dependence of hardness values on cooling rate of variously heat-treated specimens, and the variation in hardness with annealing time for various alloys is presented next:

Specimens of alloys I, II, III and IV were heated at 1350°C for 30 minutes and subsequently cooled by furnace cooling, air cooling, oil quenching and water quenching. The hardness (VPH) of the heat-treated specimens versus the cooling rates are given in Table 4.16. It is seen that the hardness of a given alloy increased with increase in cooling rate. Alloy I, however, did not seem to follow this trend. As seen from table 4.16, the hardness of the heat-treated specimens of alloy I decreased with increase in cooling rate. The decrease in hardness values was, however, not very significant. Increasing the cooling rate from AC to WQ resulted in a decrease in hardness value from ~440 to ~420.

The samples of alloys II and III were annealed at 1350°C for various time periods ranging from 15 to 240 minutes and subsequently furnace cooled to study the phenomenon of grain growth of these alloys in the α-phase field. The hardness of these annealed samples was also measured so as to establish a relationship between the hardness and grain size. The measured hardness values of alloys II and III as a function of annealing time are given in Table 4.17.

Table 4.16: Variation of Vickers hardness of heat-treated samples with cooling rate and composition.

Cooling rate	Alloy IV		Alloy III		Alloy II		Alloy I	
	VPH	Std. dev.	VPH	Std. dev.	VPH	Std. dev.	VPH	Std. dev.
FC	282	4	291	5	295	7	290	5
AC	407	7	398	9	426	33	441	17
OQ	410	4	412	7	433	21	423	20
WQ	431	10	440	17	462	15	420	28

Table 4.17 Variation of hardness with annealing time for alloys II and III.

Annealing time, min	Alloy III		Alloy II	
	Hardness, VPH	Std. dev.	Hardness, VPH	Std. dev.
15	269	6	281	10
30	282	10	295	13
60	272	8	306	8
90	299	10	297	9
120	278	10	293	10
150	288	13	283	12
240	279	10	280	5

Chapter 5

DISCUSSION

5.1 SURFACE DAMAGE DUE TO DEPOSITION OF Si AND Ti – DEPLETION

The samples were encapsulated in quartz capsules before being heat-treated. The presence of Si on the surface of the heat-treated (air cooled) samples, which was not present on the unheat-treated samples, was confirmed by the EDS analysis of the surface of the specimen and the observed discoloration of the quartz capsule. The gain in weight of the heat-treated specimens (Table 4.1) can also be attributed to the deposition of Si during the heat treatment. Therefore, it is suggested that Si evaporated from the interior surface of the capsule during heat-treatment and deposited itself on the surface of the titanium aluminide specimen. Decomposition of silica would also make oxygen available for reaction with the alloy specimen. The EDS analysis of the surface layer, however, did not show the presence of any detectable amount of oxygen on the surface of the specimen. It is therefore suggested that even if oxygen reacted with the specimen, either the amount of oxide formed was very small or the oxide layer spalled off the surface of the specimen. It is of interest to note that a gain in weight is in contrast to the loss in weight due to the loss of aluminum which was observed during the heat treatments of the specimens, wrapped in Ta-foil prior to being encapsulated in quartz tube, at 1200°C and 1000°C [152]. Deposition of Si on the surface of the specimen, due to the specimen not being wrapped in Ta-foil, and subsequent formation of titanium silicide layer seems to

have prevented the evaporation of aluminum from the specimen. Thus, it can be concluded that coating materials containing Si should prevent loss of aluminum from the surface of the specimens during exposure to high temperature. Si has also been reported to improve the oxidation resistance of titanium aluminides by forming a more stable and protective silicon oxide layer on the surface [13,153].

The free energy change associated with the formation of the Ti-Si intermetallic compounds is more negative than that associated with the formation of Ti-Al intermetallic compounds. The standard free energy change ($\Delta G°$) involved in the formation of TiAl is approximately -21 kCal/mol and that involved in the formation of Ti_5Si_3 is approximately -154 kCal/mol [154]. Moreover, composition of the surface indicated the presence of ~37 at.% Si which corresponds to the stability range of Ti_5Si_3. Therefore, the most probable compound to be present at the surface of the heat-treated specimen is Ti_5Si_3. Also, the electronegativity values of the elements indicate that Si is more electronegative than Ti and Al. Owing to this difference in electronegativity, Ti would tend to form compounds with a greater ease with Si than with Al. Al and Si are, however, not known to form any intermetallic compound. Therefore, it would seem that the Ti-Si intermetallic compounds are more stable and Ti has a greater affinity for Si than for Al. Consequently, upon deposition of Si onto the surface of the specimen at 1350°C, Ti would diffuse outwards to form titanium silicide leaving behind the observed aluminum rich layer (Figure 4.4) in the specimen.

5.2 ANALYSIS OF MICROSTRUCTURAL EVOLUTION IN THE BULK

As discussed earlier, surface and sub-surface regions of the alloy specimens underwent undesirable changes during heat treatment at 1350°C. Phase transformations in these alloys were therefore, studied by microstructural examination of the interior of the cross-section of the heat-treated specimens. The effects of cooling rates experienced by the alloys during heat treatment and the effect of composition of the alloys on microstructural evolution in the bulk of the specimens are discussed in the following sections.

5.2.1 On the Effect of Cooling Rate

The results presented in sections 4.4.1 through 4.4.4 indicate that a particular alloy's susceptibility to massive transformation increased with an increase in cooling rate. At very slow cooling rate (FC), a fully transformed lamellar microstructure was observed in all the four alloys. At increased cooling rate, the mode of transformation from α to γ was massive, with the amount of massively transformed product varying with the variation in Mn and Nb concentration in the alloy. However, at very high cooling rates, the massive transformation was suppressed in favor of $\alpha \rightarrow \alpha_2$ ordering reaction. Massive transformation, hence, requires a certain critical cooling rate, which also varies with the composition of the alloy. A certain amount of undercooling was required for the reaction to proceed completely massively rather than through bulk diffusion. It should also be noted that massively transformed microstructure was observed even at intermediate cooling rates, but the competing lamellar morphology dominated. Veeraraghavan *et al*

[111,116] have also suggested that at lower levels of undercooling "equilibrium lamellar precipitation" is predominant, and with an increase in undercooling, $\alpha \rightarrow \alpha_2$ transformation predominates. This effect of cooling rate on the mode of transformation is however, understandable considering the partitionless nature of massive transformation.

The amount of massively transformed gamma was also found to increase with increasing cooling rate. However, when the cooling rate was increased beyond the critical cooling rate, the amount of transformation product decreased and finally the transformation was suppressed by the competing $\alpha \rightarrow \alpha_2$ transformation. Increase in cooling rate increased the susceptibility to massive transformation. However, beyond the critical cooling rate, the rate of massive transformation became slower. This is better illustrated by comparing Figures 4.33, 4.36 and 4.39. Increasing the cooling rate from furnace cooling to air-cooling changed the microstructure from fully lamellar to fully massive. However, further increase in cooling rate resulted in a decrease in the volume fraction of γ_m, implying a decrease in the rate of transformation. It was indeed observed in a Ti-47.5Al alloy [116], that the growth rate decreased from ~ 0.14×10^{-2} m/s to 0.07×10^{-2} m/s when the amount of undercooling increased from ~ 210°C to 310°C.

5.2.2 On the Effect of Composition

Massive transformation has been observed in the past in various TiAl based alloys of composition ranging from 46.5 to 49 at.% Al, with and without the presence of alloying elements [23,103-118]. It was also suggested by Jones and Kaufman [23], that massive transformation does not take place in binary Ti-45Al alloy and is favored when the

overall alloy composition is close to the equilibrium composition of the gamma phase. The binary Ti-45Al alloy used in their investigation underwent complete alpha to alpha-2 ordering transformation when quenched into ice water from the alpha phase field. On the contrary, massive transformation was observed in Ti-45Al binary alloy (alloy I) in the present investigation. It should be noted that the oxygen concentration in the two alloys was comparable, that is, 400-700 ppm in the alloy used by Jones and Kaufman and 450 ppm in the binary alloy used in this study. However, in their investigation, Jones and Kaufman reported that the accuracy of composition measurement was ±1 % of nominal composition, which was 45 at.%. This suggests that the composition of the alloy used could have been in the range of 44 to 46 at.% Al. The microstructural response of the alloy containing less than 45 % Al is expected to be significantly different from that of the alloy containing 45 at.% or more Al. Also, the cooling rate experienced by the sample during quenching was not quantified. On the other hand, the composition of alloy I in the present research was measured to be 45.5 at.%. Based on the results obtained in the present investigation, the CCT diagram proposed by Jones and Kaufman has therefore, been modified to incorporate the curve for massive transformation in the schematic CCT diagram for Ti-45Al alloy (Figure 5.1). According to this modified diagram, upon furnace cooling the single phase alpha would transform to a fully lamellar microstructure. Upon air-cooling, the cooling rate would be fast enough to partially suppress the formation of lamellar microstructure and bring about massive transformation from α to γ_m. Upon increasing the cooling rate to oil quenching, the formation of lamellar structure would be suppressed by $\alpha \rightarrow \alpha_2$ ordering reaction and $\alpha \rightarrow \gamma$ transformation would take place in a massive manner. The cooling curve just passes to the left of the $\alpha \rightarrow \alpha+\gamma$

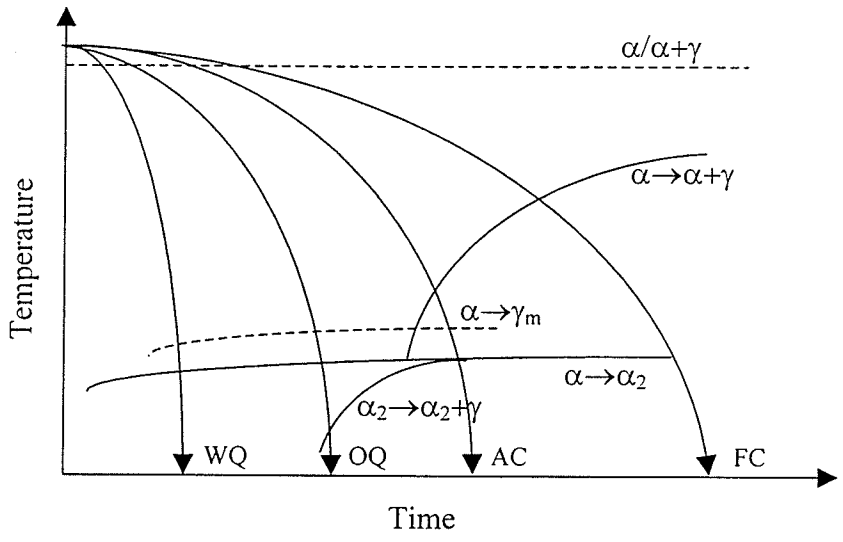

Figure 5.1: Schematic CCT diagram for alloy I (Ti-45Al). The superimposed cooling curves correspond to furnace cooling (FC), air cooling (AC), oil quenching (OQ) and water quenching (WQ).

transformation curve. The cooling curve for water quenching passes further left to the $\alpha \rightarrow \alpha+\gamma$ and the $\alpha_2 \rightarrow \alpha_2+\gamma$ transformation curves. The transformation product in this case was mainly α_2 with small percentage of massively transformed gamma phase. It should also be noted, that massive transformation never proceeded to 100 percent completion in alloy I. At lower cooling rates, the lamellar structure formation was predominant and at relatively high cooling rates, the massive transformation was suppressed by the ordering reaction.

In the present investigation, massive transformation was also observed in Ti-45Al-2Nb, Ti-45Al-2Nb-0.4Mn, and Ti-45Al-2Nb-2Mn alloys when cooled from the alpha phase field at various cooling rates. The details of microstructural evolution in the bulk of the specimens during various heat treatments are summarized in Table 5.1. It is seen that all the four alloys underwent massive type transformation when cooled at relatively higher cooling rates. The extent and rate of massive transformation, however, varied with the type and amount of alloying elements in the alloy and with the type of heat treatment that the samples were subjected to (Table 5.2). This effect of alloying elements on the massive transformation can be explained by considering the effect of alloying elements on the binary phase diagram through their site preferences in the equilibrium phases and, also through their influence on prior alpha grain size. It was suggested by Jones and Kaufman [23], that the nose of the CCT curve shifts towards left (shorter time) as the aluminum concentration increases and that the predominant equilibrium phase transformation at higher aluminum concentrations is the formation of lamellar microstructure, which takes place by the precipitation of γ-phase from the high

Table 5.1 Summary of microstructural evolution in the bulk

Alloys	Cooling Rate			
	FC	**AC**	**OQ**	**WQ**
Alloy I (45-0-0)	Fully Lamellar	Fine lamellar + occasional patches of massive gamma	α_2 + ~20% massive gamma; fine lamellar in some regions	α_2 + ~ 8 - 10% massive gamma
Alloy II (45-2-0)	Fully Lamellar	α_2 + small regions of massive gamma + fine lamellae near grain boundaries	Mainly α_2 + very small proportion of massive gamma	α_2
Alloy III (45-2-0.4)	Fully Lamellar	Massive gamma + small regions of α_2	Massive + α_2	α_2 + patches of γ_m
Alloy IV (45-2-2)	Fully Lamellar	Lamellar + Patches of gamma	Massive gamma + fine lamellar near grain boundaries	Massive + α_2

Table 5.2 Variation of amount of massively transformed gamma with composition and cooling rate

Cooling rate	Volume fraction of massive gamma, %			
	45-0-0	45-2-0	45-2-0.4	45-2-2
AC	5	8	100	-
OQ	20	3	90-93	-
WQ	8-10	~0	20-25	70

temperature α-phase and subsequent ordering of α to α_2-phase. In the binary Ti-Al system, higher the aluminum concentration in the alloy, more difficult it is to prevent decomposition of the high temperature alpha phase to a lamellar α_2/γ microstructure. In other words, much higher cooling rates are required to suppress the lamellar transformation and to bring other modes of phase transformation in operation in the alloys whose aluminum concentration is close to that of the single-phase gamma.

In the ternary Ti-Al-Nb alloy system, Nb has been reported to preferentially substitute for Ti sub-lattice sites in TiAl [41-45], thereby, increasing the equilibrium aluminum concentration of the gamma phase. Addition of Nb also expands the alpha phase field to higher Al concentrations. Addition of Nb to the binary Ti-45Al alloy would therefore move the equilibrium composition of the gamma phase ($(\alpha+\gamma)/\gamma$ phase boundary) as well as the $\alpha/\alpha+\gamma$ phase boundary away from the average composition of the alloy. Jones *et al.* [23] and Denquin *et al.* [105] have suggested that the massive type transformation is favored when the alloy composition is close to the equilibrium aluminum concentration of the gamma phase. According to this, addition of Nb to a binary TiAl alloy would reduce the alloy's susceptibility to massive transformation. However, it is important to note that addition of Nb to a binary Ti-45Al alloy would significantly reduce the diffusivity and, hence, at a given cooling rate it would be much easier to prevent long range diffusion in the ternary alloy (alloy II). This implies that it would require a relatively slower cooling rate to suppress the formation of the equilibrium lamellar microstructure and bring about massive transformation in the ternary alloy II (Ti-45Al-2Nb), as compared to its binary counterpart. This is more evident from Figures 4.20 and

4.31. Also, at a given cooling rate, addition of Nb tends to lower the rate of transformation. For instance, as seen from the Table 5.2, upon water quenching Ti-45Al alloy from the α-phase field, 8-10 % of α-phase massively transformed gamma (γ_m) whereas, in Ti-45Al-2Nb the volume fraction of massively transformed gamma was nil. In addition, as seen from Table 5.3, addition of 2 at.% Nb to the binary Ti-45Al alloy increased the prior alpha grain size. The increase in grain size would result in a reduction in the number of nucleation sites available for the nucleation of the gamma phase at grain boundaries, and hence would reduce the rate of transformation. This in turn would cause the C-curve for $\alpha/\alpha+\gamma$ transformation and that for $\alpha \rightarrow \gamma_m$ transformation to shift to the right (longer times), thereby, decreasing the critical cooling rate required for the initiation of massive transformation. The CCR in alloy II was observed to be slower and the competing phase transformation was the $\alpha \rightarrow \alpha_2$ ordering transformation. This is in contrast to alloy I, where air-cooling resulted primarily in a lamellar microstructure. This also implies that addition of Nb to binary Ti-Al alloy would suppress $\alpha \rightarrow \alpha+\gamma$ lamellar transformation. Also, the amount of massively transformed gamma observed in the microstructure was smaller in alloy II as compared to alloy I, suggesting a decrease in the rate of transformation with the addition of Nb to the alloy. Incorporating this effect of Nb, the CCT diagram for binary Ti-45Al has been modified for Ti-45Al-2Nb alloy as shown in Figure 5.2. This influence of addition of Nb is manifested as the shifting of the transformation curves to longer times.

Table 5.3 Variation of grain size with composition

Alloys	Grain size, microns
45-0-0 (alloy I)	980
45-2-0 (alloy II)	1125
45-2-0.4 (alloy III)	850
45-2-2 (alloy IV)	500

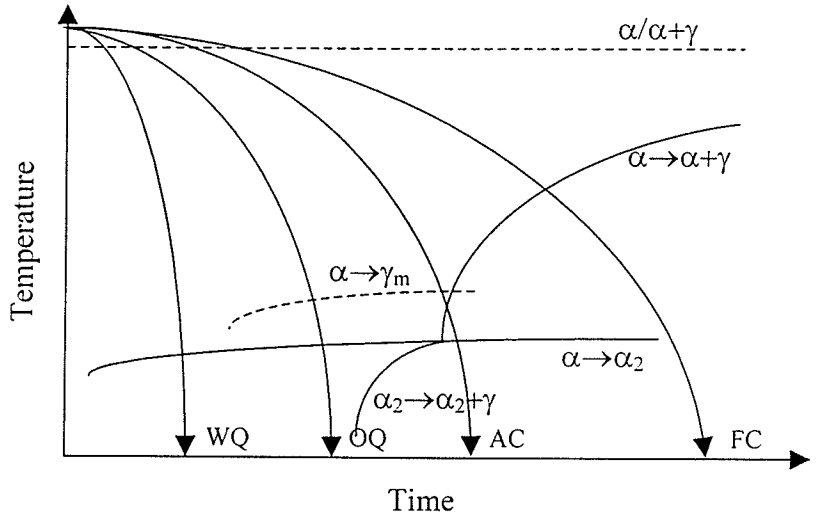

Figure 5.2: Schematic CCT diagram for alloy II (Ti-45Al-2Nb). The superimposed cooling curves correspond to furnace cooling (FC), air cooling (AC), oil quenching (OQ) and water quenching (WQ).

On the other hand, in the ternary Ti-Al-Mn system, Mn has been reported to preferentially substitute for the Al sub-lattice sites in TiAl when present in small concentrations [42-45], thereby reducing the equilibrium concentration of the gamma phase. This would bring the overall composition of the alloy closer to the equilibrium composition of the gamma phase, which in turn would tend to favor massive transformation. Addition of 0.4 at.% Mn to ternary Ti-45Al-2Nb alloy resulted in a dramatic change in microstructure. Upon air-cooling, the microstructure obtained in alloy II consisted mainly of α_2 phase with few massively transformed patches near the grain boundaries. Also observed was occasional presence of fine lamellae near grain boundaries. Unlike alloy II, the microstructure obtained in alloy III upon air-cooling consisted primarily of massively transformed gamma. This implies that addition of a mere 0.4 at.% of Mn significantly altered the mode of transformation and enhanced the alloy's susceptibility to massive transformation. It is therefore, suggested that massive transformation would be a preferred mode of transformation in the presence of Mn. The effect of addition of 0.4 %Mn to Ti-45Al-2Nb alloy on the CCT diagram is shown schematically in Figure 5.3. The curve for massive transformation shifts to shorter times with the addition of Mn to the ternary Ti-45Al-2Nb alloy. It was also observed that the volume fraction of γ_m increased with the addition of Mn (see Fig.4.28 and 4.36, and Table 5.2), which also implies that the rate of massive transformation is accelerated by the addition of Mn. This influence of Mn on the rate of massive transformation can be attributed to the reduction in prior grain size in the presence of Mn, which would increase the nucleation rate and, hence, the overall rate of transformation.

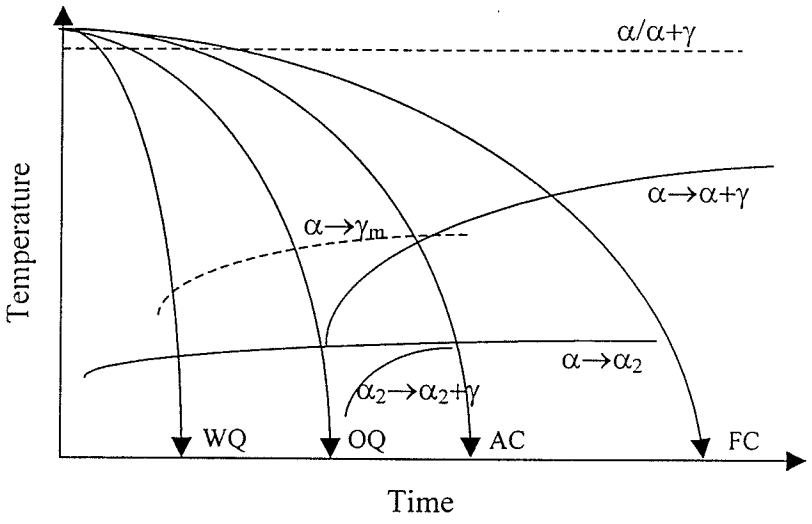

Figure 5.3: Schematic CCT diagram for alloy III (Ti-45Al-2Nb-0.4Mn). The superimposed cooling curves correspond to furnace cooling (FC), air cooling (AC), oil quenching (OQ) and water quenching (WQ).

In addition, it should be also noted that Mn is a γ-phase stabilizer and that it promotes lamellar structure formation [44,64]. This implies that an increase in Mn concentration of the alloy would increase the critical cooling rate (CCR) required for massive transformation. In the present investigation, the critical cooling rate for massive transformation was indeed observed to be a function of Mn concentration. Increase in Mn concentration from 0.4 to 2 at.%, decreased the susceptibility of the alloy to massive transformation (see Figs. 4.33 and 4.43). That is, a much higher cooling rate was required to suppress the equilibrium lamellar transformation in alloy IV as compared to alloy III. The CCR for the complete massive transformation of alloy III was close to AC and that for alloy IV was found to be between OQ and WQ. Therefore, it is suggested that an increase in Mn concentration of the alloy would increase the critical cooling rate for massive transformation. This suggests that the addition of Mn would shift the $\alpha \rightarrow \alpha+\gamma$ transformation curve to shorter times. This modification has been incorporated in Figure5.4 and is manifested as the shifting of the C-curve for the precipitation of equilibrium gamma phase to shorter times. It is known that the site preference of Mn in TiAl is sensitive to Al concentration and to the amount of Mn in the alloy [44,45]. With increase in Mn concentration in the alloy, the probability for Mn atoms to occupy Ti sub-lattice sites increases. The alloys III and IV are quaternary alloys containing the same amounts of Al and Nb but different Mn concentrations. A detailed analysis of the effect of Nb on the site occupancy of Mn in quaternary TiAl alloy is required so as to comprehensively elucidate the phase transformation behavior in quaternary alloys. Based on the present results, it is suggested that an increase in Mn and the presence of Nb in the alloy would reduce the probability of Mn atoms occupying Al sub-lattice sites.

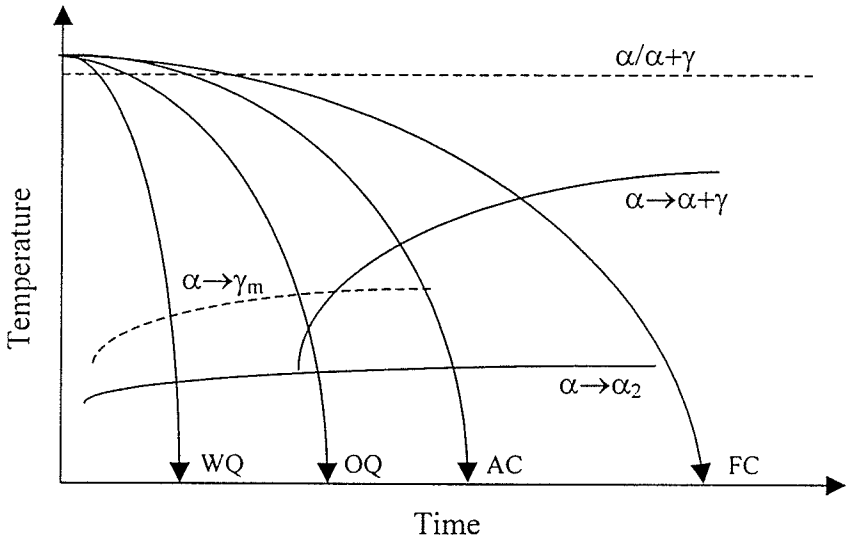

Figure 5.4: Schematic CCT diagram for alloy IV (Ti-45Al-2Nb-2Mn). The superimposed cooling curves correspond to furnace cooling (FC), air cooling (AC), oil quenching (OQ) and water quenching (WQ).

Despite the reduced susceptibility to massive transformation, the volume fraction of massively transformed gamma (γ_m) was observed to increase with increase in Mn concentration of the alloy (see figures 4.31, 4.39 and 4.48a). The effect of Mn concentration on grain size of fully lamellar microstructure and on the volume fraction of γ_m in water-quenched samples is graphically represented in Figure 5.5. Larger volume fraction of the massively transformed product suggests a faster transformation rate. This phenomenon can be attributed to the reduction in grain size accompanying the increase in Mn concentration of the alloy. Addition of Mn reduced the grain size and also made the grain boundaries more irregular and curved. The lamellar grains are presumed to represent the prior alpha grains and grain boundaries. Therefore, addition of Mn would refine the prior alpha grain size and also make the prior boundaries more irregular. This, in turn, would increase the number of sites available for the nucleation of massive gamma at the grain boundaries and, hence, increase the probability of nucleation. This would result in an increase in the rate of nucleation and hence the overall rate of transformation.

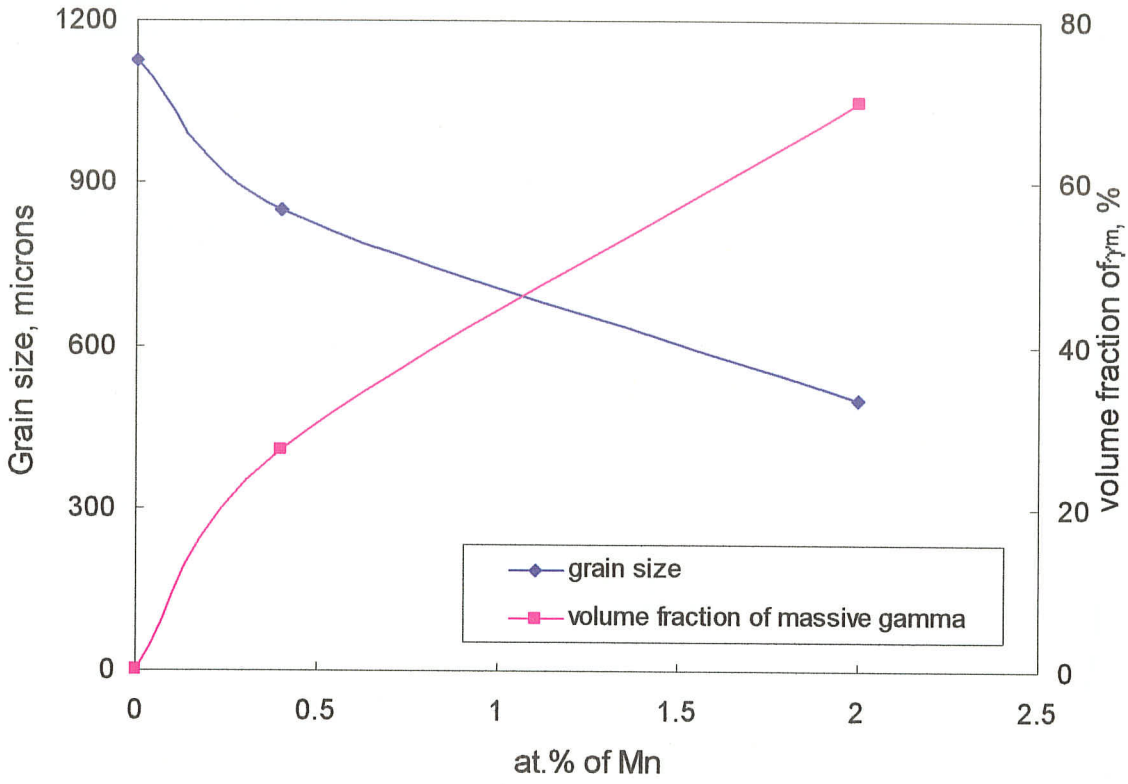

Figure 5.5: Plot of lamellar grain size and volume fraction of massively transformed gamma versus Mn concentration in the alloy.

5.3 ON THE MECHANISM OF MASSIVE TRANSFORMATION

One of the issues of major concern regarding massive transformation in the Ti-Al system is its nucleation and growth mechanism. Different mechanisms have been analyzed and proposed in the light of the nature of the interface between the product γ_m phase and the parent α-phase [105,113,128]. However, no consensus exists regarding these mechanisms. Based on the present results, the most plausible mechanisms for the nucleation and growth of γ_m are discussed within the scope of this research next.

5.3.1 Nucleation of γ_m

Nucleation mechanism has been studied in detail only by Denquin and Naka [105] and by Zhang *et al.* [113]. It was suggested by Denquin and Naka that the nucleation of γ_m phase takes place essentially at the initial α grain boundaries. No rational orientation relationship was observed between the product γ_m phase and the parent phase. Nonetheless, they have proposed that γ_m phase nucleates at the grain boundary coherent with one grain. Subsequent growth takes place by propagation of γ_m in the neighboring incoherent grain. Also, they associated the apparent absence of low index orientation relationship to the experimental difficulties in crystallographically examining the nascent γ_m phase, which, they found to be restricted to the vicinity of the α grain boundary. In the present investigation, however, the γ_m phase was found to be present near the grain boundaries as well as inside the prior α-grains (see Fig.4.48b). Hence, it is suggested that though the grain boundaries act as primary nucleation sites, γ_m phase also tend to nucleate well within the interior of prior α-grains. Careful tilting experiments in TEM also

suggested that no specific/rational orientation relationship existed between the parent and the product phase. Moreover, nascent gamma phase was observed in one of the samples at a grain boundary (see Figures 4.14a and 4.15). The absence of any low index orientation relationship, however, again suggests that γ_m did not nucleate coherently with either of the two grains. To definitively establish the nature of the grain boundaries and the inter-phase interfaces, so as to confirm the mechanism of nucleation for γ_m, comprehensive high resolution TEM (HRTEM) analysis is required. Nonetheless, based on the results obtained so far, it is suggested/hypothesized here that γ_m phase primarily nucleates incoherently at the prior alpha grain boundaries with occasional nucleation taking place inside the grains. This phenomenon was more predominant in the high Mn alloys, where the volume fraction of γ_m was also observed to be higher i.e., the transformation rate was faster.

In their investigation, Zhang *et al* [113] never observed any γ_m without the presence of lamellar gamma (γ_l). According to their suggested nucleation mechanism, when γ_l intersects a grain boundary, it would propagate into the neighboring untransformed alpha grain in massive manner. However, it should be noted that the γ lamellae could also coarsen and spread in the neighboring grain even during discontinuous coarsening. TEM analysis of our samples did not indicate any such phenomenon. Moreover, the mechanism suggested by Zhang *et al* fails to justify the formation of γ_m without the presence of any lamellar γ, such as those observed in very rapidly cooled samples (e.g. WQ) in this study. Therefore, their mechanism is discounted in the context to the present alloys.

5.3.2 Growth of γ_m - Nature of growth front and mechanism of γ_m growth

According to Perepezko [125] and Massalski [126], the growth of a massive product may be achieved by either of the following two mechanisms: (1) Thermally activated short-range jump of atoms across the incoherent interface, in which the interface should be curved; or (2) By ledge mechanism, in which the interface should be planar. Both coherent and incoherent interfaces have been observed to be present between the massively transformed product and the parent phase in the Ti-Al system during massive transformation [105,113,128]. Denquin and Naka [105] reported the γ_m/α interface to be curved. On the other hand, Lin *et al* [128] reported a completely coherent interface preserving the perfect crystallographic orientation relationship, i.e, $(111)_{\gamma m}$ // $(0001)_\alpha$ and $[110]_{\gamma m}$ // $[11\bar{2}0]_\alpha$ and hence, suggested a ledge mechanism for the growth of γ_m. Wang *et al* [115] observed both curved and planar interfaces, however, they did not observe any low index rational orientation relationship between the γ_m and α-phase. Zhang *et al* [113] also observed faceted/planar interfaces but no orientation relationship was observed. Based on their results and analyses, both of the groups have proposed that the interface is incoherent. In the present investigation, many such γ_m/α interfaces were examined and both irregular/curved and planar interfaces were observed (see Figures 4.12 and 4.19). However, no low index orientation relationship existed between the parent and product phase. It is therefore, proposed that the growth of γ_m would seemingly take place by transfer of atoms across the 'incoherent' interface. The factors that would restrain the transfer of atoms would therefore reduce the rate of transformation.

Recently, Nie *et al* [127] have shown that even in the apparent absence of any low-index/rational orientation relationship, the interfaces can be partially coherent rather than incoherent. A meticulous HRTEM analysis is required to establish the nature of the inter-phase interfaces obtained under various HT conditions in alloys with varying composition, so that the mechanism of interface migration, i.e., the growth mechanism of γ_m can be ascertained. Nonetheless, within the scope of this research, it is inferred here that the product-parent phase interfaces are incoherent in nature and that the growth of massively transformed product takes place by transfer of atoms across these interfaces.

5.4 MASSIVE TRANSFORMATION – GRAIN SIZE EFFECT

Figure 4.55 on page (146-149) shows that the lamellar grain size was found to increase with increase in annealing time at 1350°C. This suggests rapid coarsening of alpha grains during annealing in the alpha-phase field. It was also observed that the volume fraction of γ_m decreased with increase in annealing time, i.e., with increased grain size. Figure 5.6 shows the trend of grain size and volume fraction of γ_m as a function of annealing time at 1350°C. The volume fraction of the transformed product is indicative of the rate of transformation. This would imply that the transformation rate is slower when the prior alpha grain size is coarser. The grain size dependence of the transformation kinetics of $\alpha \rightarrow \gamma_m$ massive type transformation can be rationalized by considering the availability of nucleation sites in different grain sized materials.

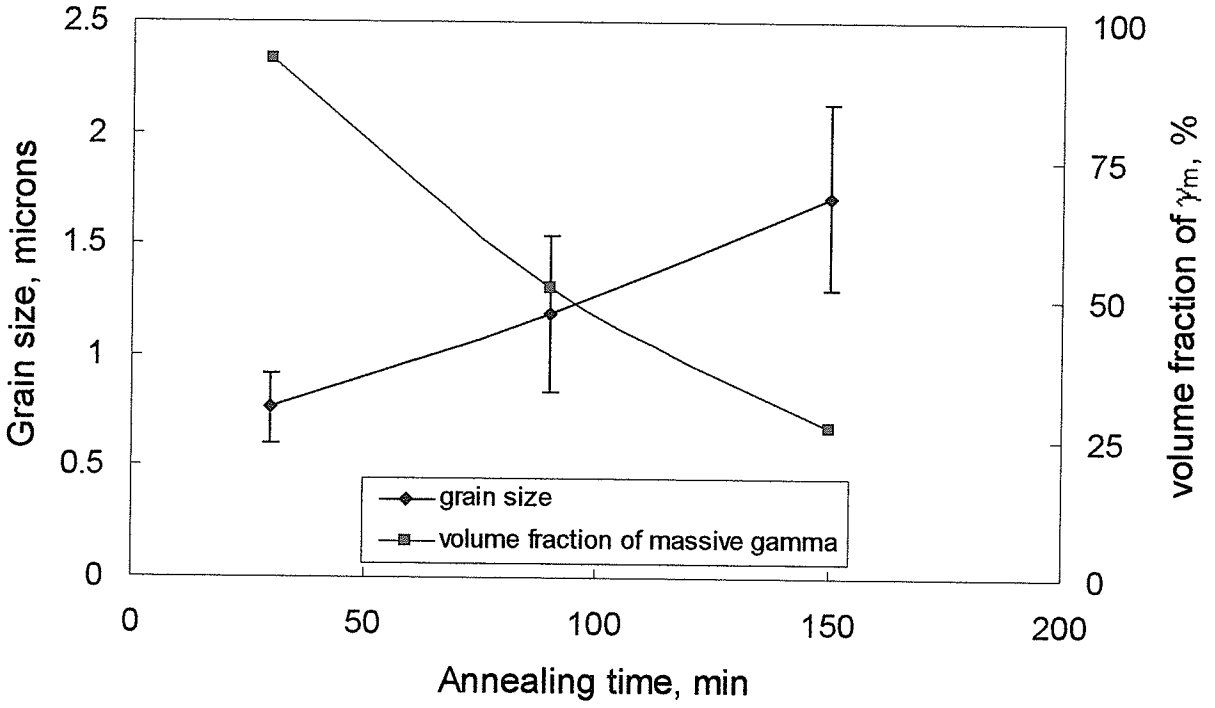

Figure 5.6: Plot of grain size of furnace cooled samples and volume fraction of massively transformed gamma in IWQ samples of alloy III (Ti-45Al-2Nb-0.4Mn) versus annealing time at 1350°C.

When the grain size is large, it reduces the total grain boundary area per unit volume. Also, as discussed in the previous section (section 5.3), the pre-existing grain boundaries are considered to be the primary nucleation sites for massive transformation. It has been previously suggested [126,155] that the growth of massively transformed product is always very rapid and that the overall rate of transformation is primarily controlled by nucleation rate. The reduction in grain boundary area per unit volume would reduce the probability of nucleation of γ_m at prior grain boundaries and hence, the rate of nucleation. Consequently, the volume fraction of the transformed product would also be reduced. With increase in grain size, the grain boundaries also become more planar and energy of the boundaries decreases. This would also reduce the probability of nucleation at the grain boundaries. In effect, the increase in prior alpha-grain size would retard the rate of massive transformation. Figure 5.7 shows a log-log plot of volume fraction of massively transformed (V_f) in IWQ samples versus grain size (G.S) which yields a straight line graph. The equation of the straight line can be written as follows:

$$\log (V_f) = C_o + m \log (G.S) \qquad \text{..... Eq. [5.1]}$$

The slope of the straight line, m, obtained from the graph was – 1.5. The negative slope of the line is implicative of a decrease in the rate of massive transformation with increase in grain size, keeping the composition of the alloy constant.

At a given cooling rate and composition, the growth rate is expected to be constant. Hence, the rate of transformation would be primarily governed by the rate of nucleation. A slower rate of transformation would therefore, imply a longer incubation period for the transformation to start which in turn would cause the CCT curve for massive

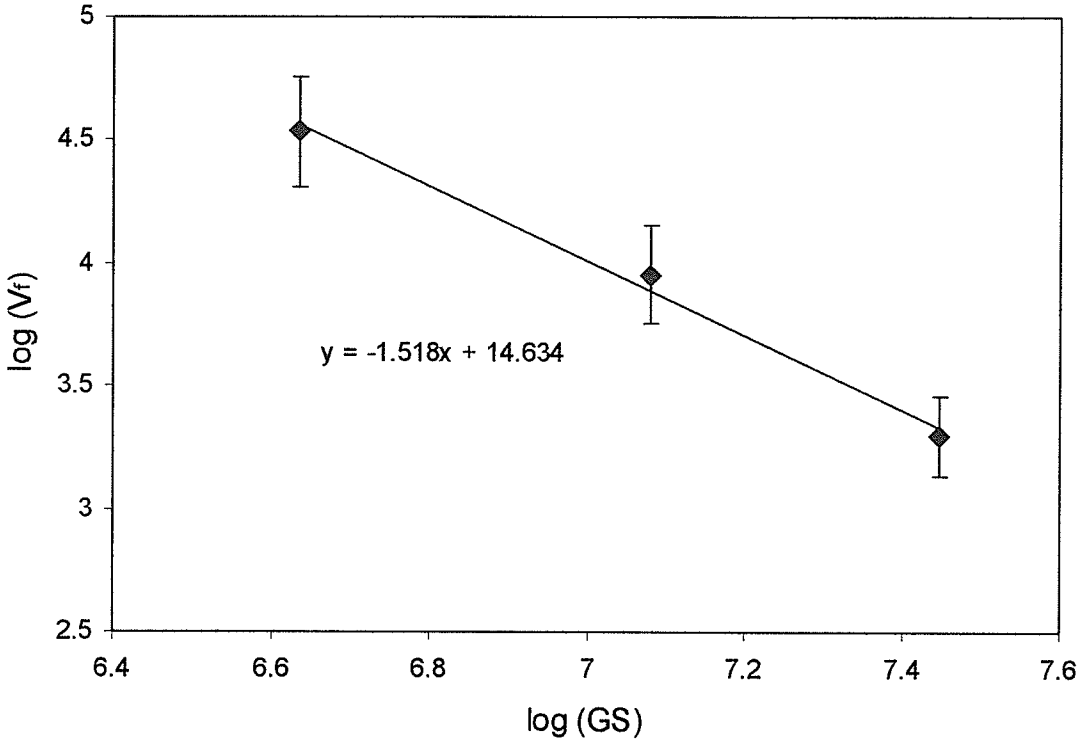

Figure 5.7: log – log plot of volume fraction of massively transformed gamma in IWQ samples versus grain size of FC samples of alloy III.

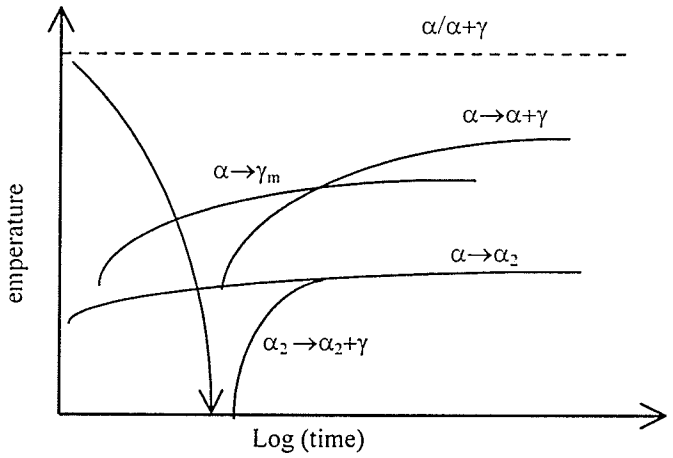

(a)

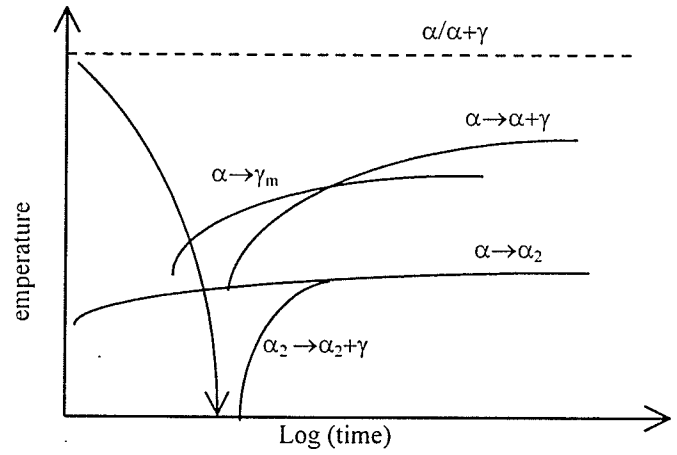

(b)

Figure 5.7: Schematic CCT diagram of alloy III (Ti-45Al-2Nb-0.4Mn) modified for (a) fine grained and (b) coarse grained material.

transformation to shift to the right i.e. to longer times. An increase in grain size would therefore shift the C-curve to longer times. Conversely, a reduction in grain size would increase the rate of transformation, hence shifting the C-curve for massive transformation to shorter times. This also implies that the critical cooling rate for massive transformation would be higher in a small grained material as compared to a coarse grained material. This influence of grain size on massive transformation and hence on the CCT diagram of Ti-45Al-2Nb-0.4Mn (alloy III) is schematically depicted in Figure 5.8 (a&b).

5.5 ANALYSIS OF GRAIN GROWTH KINETICS – EFFECT OF COMPOSITION

Upon furnace cooling, formation of lamellar microstructure takes place by the precipitation of γ lamellae in the pre-existing α-grains. The lamellar colony size can therefore, be presumed to be representative of the prior alpha grains. The relationship between the average grain size, D and the annealing time, t can be expressed by the empirical grain growth equation as follows:

$$D = Kt^n \quad \ldots \quad \text{Eq. [5.2 a]}$$

$$\text{or, } \log D = \log K + n \log t \quad \ldots \quad \text{Eq. [5.2 b]}$$

Where, K is a constant; and

n is the grain growth exponent.

Under ideal conditions, the value of n should be equal to 0.5 for pure metals for parabolic growth. For non-ideal conditions, the value of n has been found to vary from 0.2 to 0.5,

depending on composition of the material and the annealing temperature (that is, on the factors which affect the rate of grain growth). Several such analyses have also been done on other γ-TiAl based alloys with varying concentrations of Al and other alloying elements such as Nb, Ta, W, Cr and Si [156-160]. The value of grain growth exponents in these alloys was found to vary from 0.2 to 0.45. The rate of grain growth will however, depend on composition because different alloying elements have different influence on the lamellar grain size and grain growth; and also on the temperature of annealing because grain growth is a thermally activated process.

Figure 5.9 shows a log-log plot of average grain diameters and annealing time for alloy II and III. As seen, the graph yields straight line for both the alloys with a linear slope of 0.38 and 0.52 for alloy II and alloy III, respectively. This suggests that alloy II exhibits a slower rate of grain growth as compared to alloy III. This difference in rate of grain growth can be rationalized by considering the difference in the initial grain sizes and the nature of grain boundaries of the two alloys. The driving force for grain growth lies in the total internal energy of the system. During grain growth, some grains grow while the others disappear and the average grain size increases. Thus the overall effect of grain growth is the reduction in the total internal energy due to a decrease in total grain boundary area per unit volume. Smaller the grain size, greater will be the grain boundary area per unit volume and hence, higher will be the total internal energy of the system. This will make the system more unstable and increase the driving force available for grain growth, which in turn will result in higher rate of grain growth. Mn reduced the grain size of fully lamellar microstructure. Increase in Mn concentration from 0 to 2 at.%

resulted in a significant decrease in grain size of the lamellar microstructure (see Table 5.3). The driving force available for grain coarsening in alloy II would therefore be less as compared to alloy III.

In addition, it should also be noted here, that the grain boundaries of alloy III were more irregular and curved as compared to those of alloy II. It is generally accepted that the grains whose boundaries are concave outward, grow in size and those having convex outward boundaries shrink during annealing. This is due to the more closely packed arrangement of boundary atoms on the concave side. Also, during grain growth, the grain boundaries migrate towards their center of curvature and the rate of boundary migration (rate of grain growth, $\dot{G}$) varies inversely with the radius of curvature, R:

$$\dot{G} \propto 1 / R \qquad \text{.... Eq. [5.3]}$$

The larger the curvature of the boundary, the faster would be the movement of grain boundaries. Therefore, the rate of grain growth would be higher in a material having more curved grain boundaries. This could be one of the reasons of the experimentally observed higher rate of grain growth in alloy III which had a more irregular lamellar colony boundaries as compared to alloy II. Here the boundaries between lamellar colonies are presumed to represent nature of prior alpha grain boundaries.

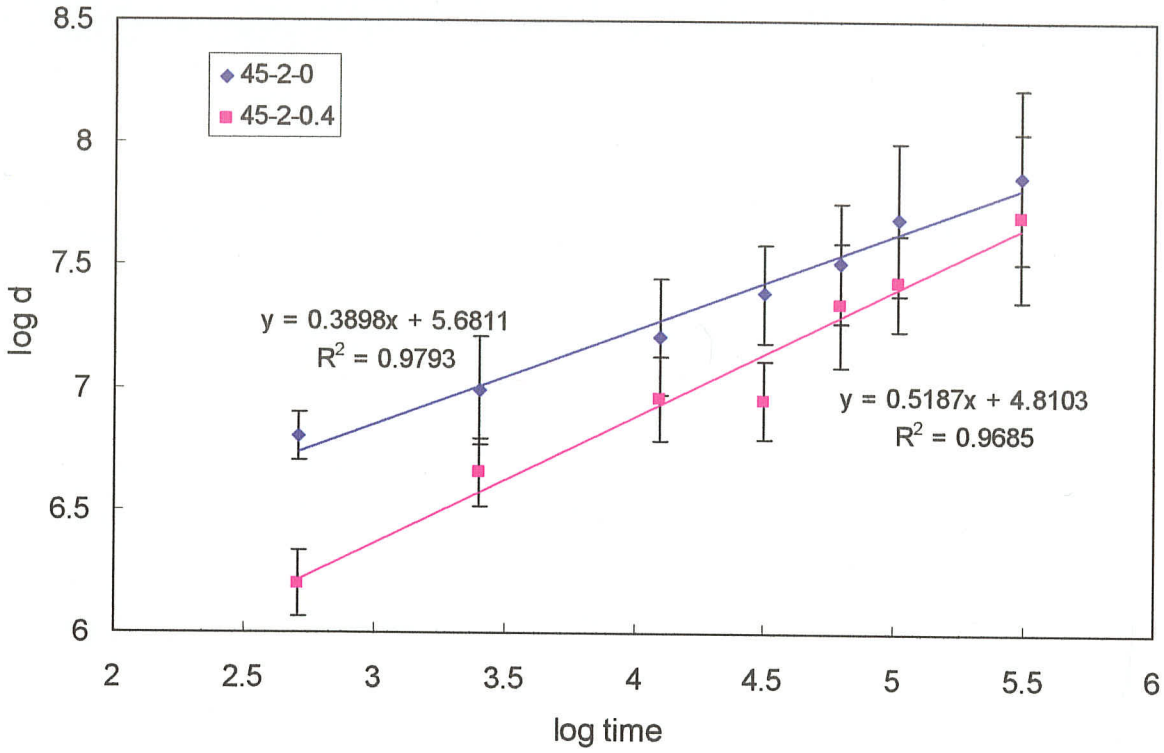

Figure 5.9: log – log plot of average grain size versus annealing time for alloy II (Ti-45Al-2Nb) and alloy III (Ti-45Al-2Nb-0.4Mn).

5.6 ON THE LAMELLAR STRUCTURE FORMATION

The grain size increased with increase in annealing time. Gamma lamellae (γ_l) primarily nucleate at SF's in α-phase. However, it has been suggested [86] that the grain boundaries that act as a source of SF can serve as nucleation sites for γ_l. The increase in grain size results in a reduction in the total grain boundary area available for the nucleation of gamma plates. This would result in a reduction in the nucleation rate and would result in an increase in interlamellar spacing with increasing annealing time/grain size. Figure 5.10 shows the variation in grain boundary area per unit volume and interlamellar spacing as a function of annealing time for alloy III. The grain boundary area per unit volume was determined using the equation [161]:

$$S_v = 2\overline{N_L} \qquad \ldots \text{Eq. [5.4]}$$

Where,

S_v = grain boundary area per unit volume, mm^2/mm^3; and

$\overline{N_L}$ = average number of intersections per unit length of a random test line, mm^{-1}.

It is seen from the graph, that the interlamellar spacing increased from ~ 0.6 μm to ~1.13 μm when the grain boundary area per unit volume decreased from ~2.79 mm^2/mm^3 (30 min) to ~0.64 mm^2/mm^3 (240 min).

It was also observed that short annealing times resulted in interlocked lamellar grain boundaries. The grain boundaries/lamellar colony boundaries, however, became increasingly planar with increasing annealing time (see Figure 4.55). Zhang *et al* [162]

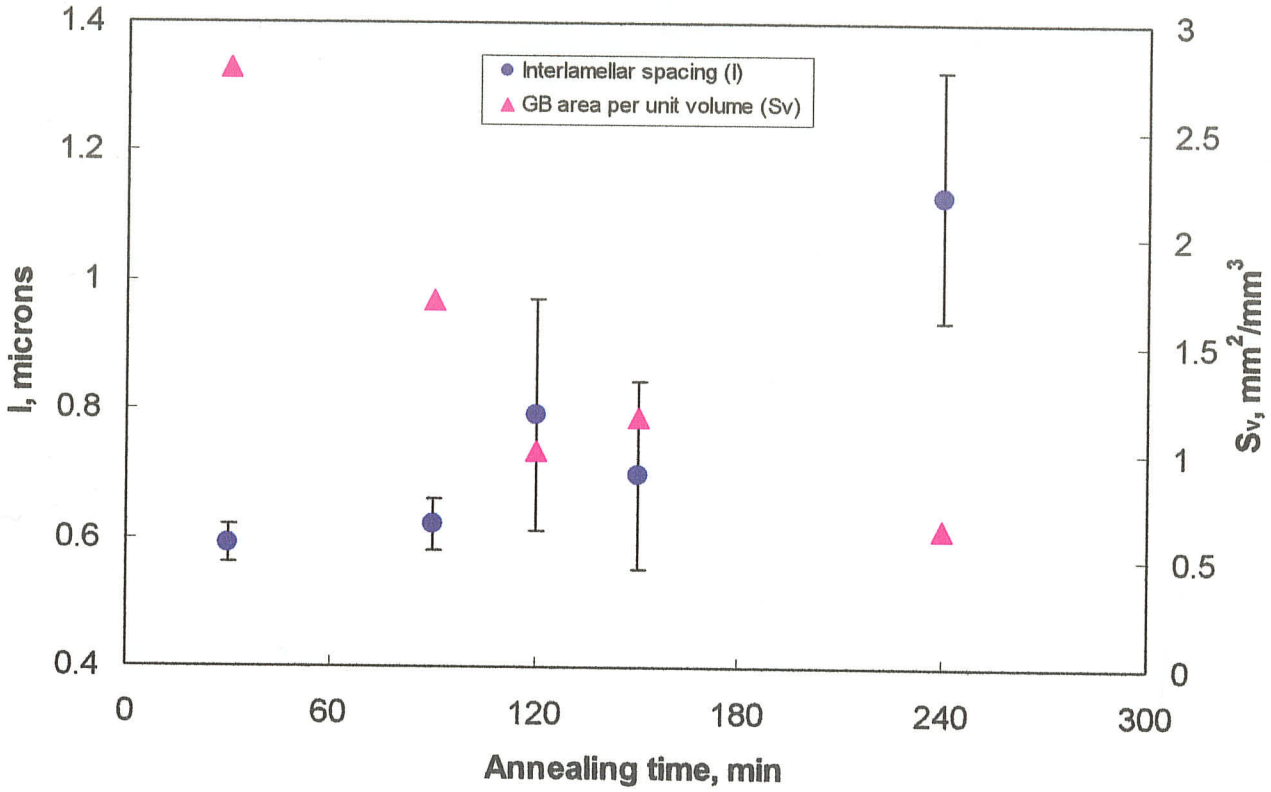

Figure 5.10: Graph showing variation of grain boundary area and interlamellar spacing with annealing time

have associated the formation of interlocked grain boundaries with cooling rate and have suggested that higher cooling rates resulted in more planar grain boundaries. Dudzinski *et al* [148], on the other hand suggested the lowering of grain boundary energy level to be responsible for the formation of planar boundaries. It should be noted that the interlocked grain boundaries form only along certain specific boundaries. The grain boundaries that are interlocked, most likely possess higher energy and hence, the growth of lamellar laths would take place across such boundaries so as to reduce the total internal energy.

5.7 SCOPE OF GRAIN REFINEMENT IN TWO PHASE ALLOYS

Generally fully lamellar alloys are coarse grained and exhibit poor tensile properties. Grain refinement, however, provides an effective avenue for improving the ductility of titanium aluminides having fully lamellar microstructure. Many grain refinement methods have been explored and identified, specifically, alloying additions, thermo-mechanical processing, cyclic thermal treatments, etc. Two types of heat treatments have been documented to effectively refine the lamellar grain size [140-144]. Both the methods involve initial heating of the alloy in the α-phase field followed by quenching and tempering treatment. Quenching resulted in $\alpha \rightarrow \gamma_m$ or $\alpha \rightarrow \gamma_f$ transformation. Subsequent tempering was done either in the $\alpha_2+\gamma$ or $\alpha+\gamma$ phase fields. Grain sizes of 150 to 200 microns have been observed by tempering in the $\alpha_2+\gamma$ phase field [141]. On the other hand lamellar grains as small as ~ 10-25 microns in size have been observed by tempering in the $\alpha+\gamma$ phase field [142-144].

These grain refinement techniques are less tedious and more cost effective as compared to alloying and thermo-mechanical processing. For these methods to be effective, the alloy must undergo massive transformation upon fast cooling. Therefore the alloys that are more susceptible to massive transformation exhibit excellent promise for grain refinement. Alloy III transformed to almost 100 % γ_m when air cooled from the α-phase field. Subsequent tempering treatment of this heat-treated alloy could lead to a significant grain refinement. Also alloy IV would transform completely to γ_m when cooled at a rate between OQ and WQ. Thus the alloys, III and IV, possess high potential for grain refinement and hence improvement of tensile properties. The grain size of the fully lamellar microstructure obtained by conventional furnace cooling of alloy III and IV was ~850 microns and ~500 microns, respectively. Moderately fine-grained (grain size ~ 150 microns) fully lamellar microstructure was also obtained in alloy IV during a two step cooling from the α-phase field (see figure 4.60). The exact mechanism of formation of this fine lamellar microstructure, however, needs to be investigated in detail. Alloys I and II, on the other hand, were inherently relatively coarse grained and 100 % $\alpha \rightarrow \gamma_m$ transformation was never accomplished. Thus, grain refinement of these alloys would never be achieved solely by heat treatment and some sort of thermo-mechanical treatment will be required to bring about grain refinement.

5.8 COMPOSITION / MICROSTRUCTURE / HARDNESS CORRELATION

The hardness measurement data of variously heat-treated samples of alloys I, II, III and IV are graphically represented in Figure 5.11. In furnace cooled condition, alloy I possessed highest hardness value. Alloys II and III, that contain 2 at.% Nb each and, 0 and 0.4 at% Mn, respectively, had almost similar hardness values (VPH ~ 290). Alloy IV exhibited lowest hardness in FC condition. Hence, it is suggested that an increase in Mn concentration decreased the hardness of the alloy. It is important to note here that there was only a marginal difference in the hardness values of the FC samples of the four alloys used in this study.

Effect of cooling rate: With an increase in cooling rate from furnace cooling to air cooling, there was a significant increase in the hardness values. The hardness numbers increased from 280-290 to 400-440. Further increase in cooling rate to oil quenching resulted in only a slight increase in hardness numbers in all the alloys except alloy I, which exhibited an inverse trend. Water quenching resulted in a significant increase in the hardness values for alloys II, III and IV.

Figure 5.12 and 5.13 show the variation of hardness and volume fraction of massively transformed gamma with cooling rate for alloys II and III, respectively. As seen, the volume fraction of γ_m decreased and the hardness increased with increased cooling rate. This can be attributed to the increase in the volume fraction of untransformed alpha-2 phase, which is the harder of the two phases.

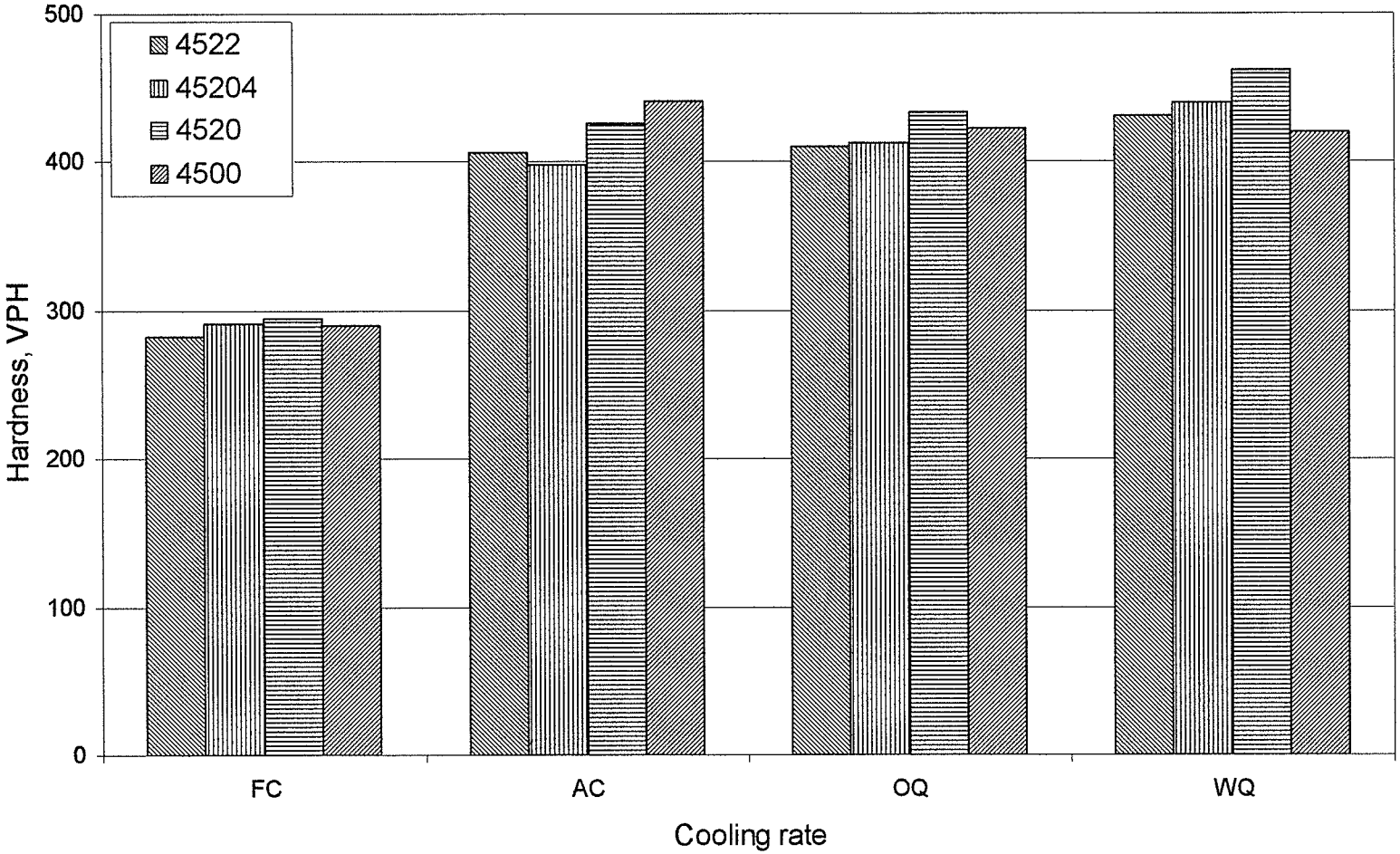

Figure 5.11: Bar graph showing the variation of hardness with cooling rate for alloys I, II, III and IV.

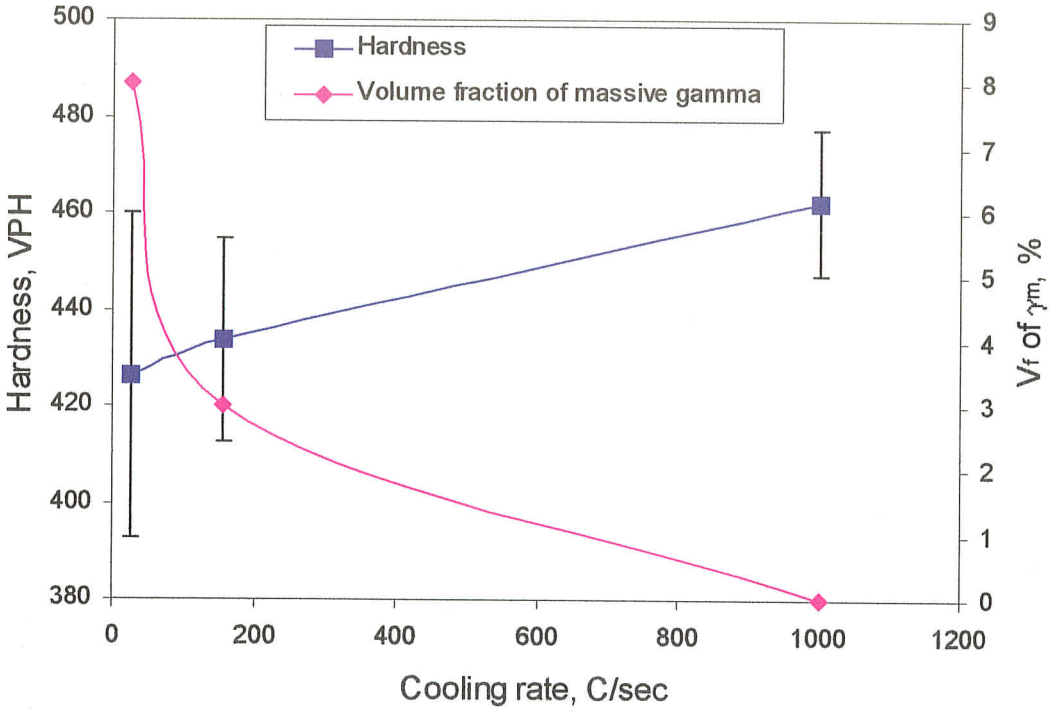

Figure 5.12: Plot of volume fraction of massively transformed gamma and the hardness of the heat-treated samples of alloy II versus cooling rate.

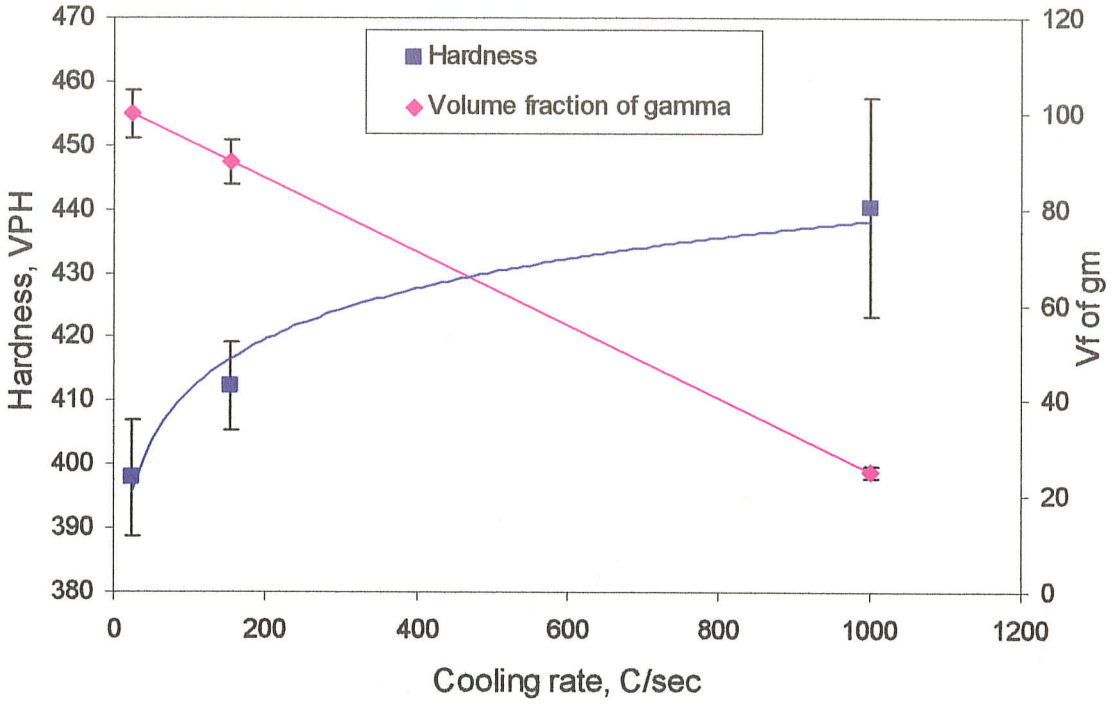

Figure 5.13: Plot of volume fraction of massively transformed gamma and the hardness of the heat-treated samples of alloy III versus cooling rate.

For a given cooling rate, the hardness was decreased with increase in the Mn concentration of the alloy. For instance, the water-quenched sample of alloy II had highest hardness value (~ 462) and alloy IV had lowest hardness value (~ 430) (see Figure 5.14). This composition dependence of the hardness of quenched samples can also be attributed to the variation in the extent of massive transformation, i.e. the volume fraction of alpha-2 and γ_m in the microstructure, with the Mn concentration of the alloy.

Effect of grain size: The annealed samples exhibited fully transformed lamellar microstructure. The grain size was observed to increase with annealing time. Figure 5.15 shows the variation of hardness with annealing time. As seen from the figure, the hardness first increase with increase in annealing time, reached a maximum value and then decreased with further increase in annealing time. This behavior is better illustrated in alloy II. The hardness data of alloy III were scattered and hence, no specific trend could be deduced. Mechanical testing of fully lamellar alloys with different grain sizes is required to establish a relationship between grain size and tensile properties.

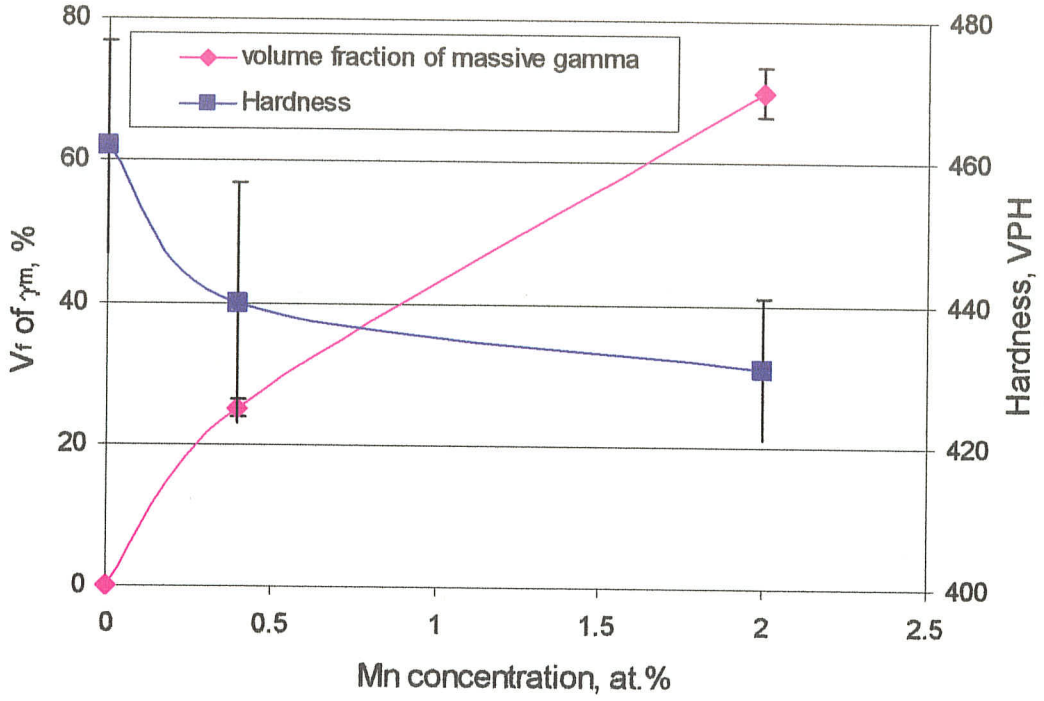

Figure 5.14: Plot of volume fraction of massively transformed gamma and the hardness of the water quenched samples versus Mn concentration.

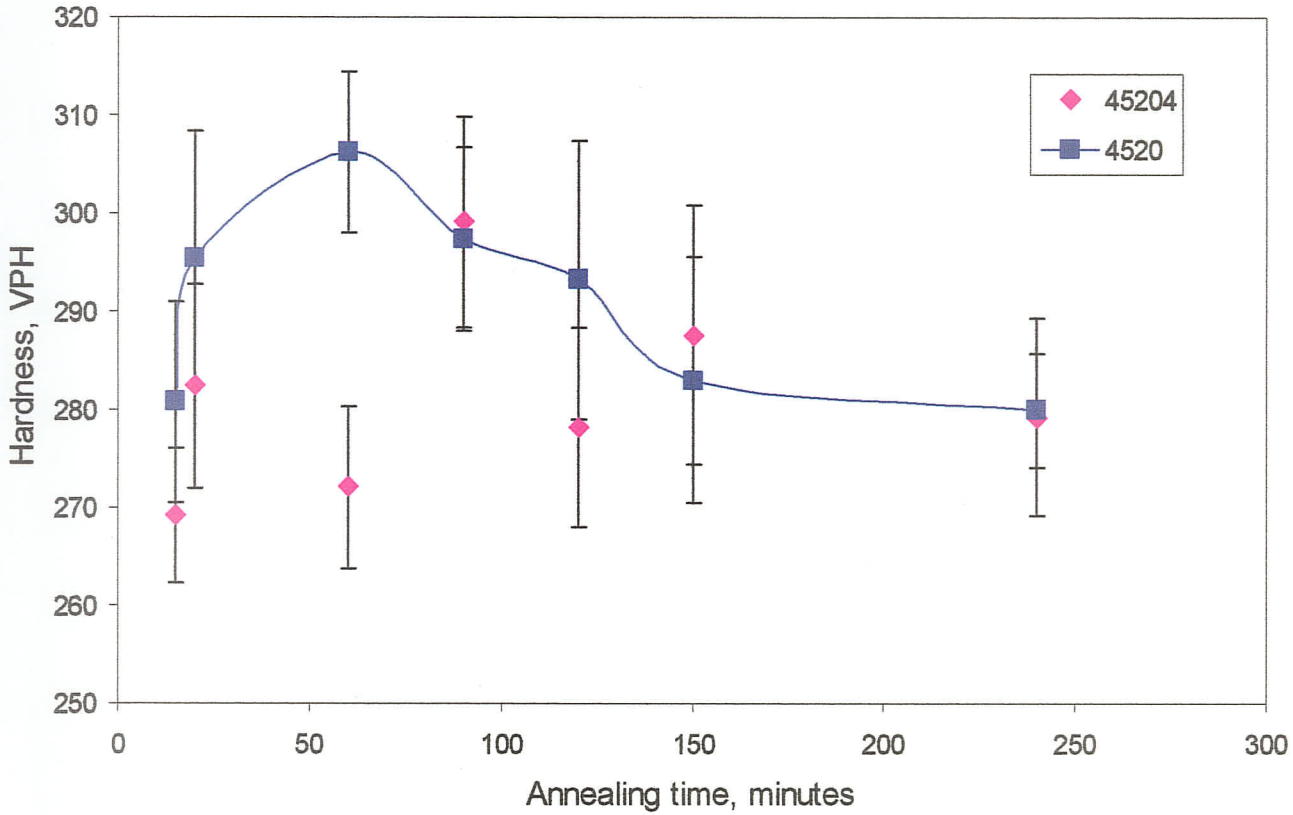

Figure 5.15: Graph showing the variation in hardness with annealing time in FC samples of alloys II and III.

Chapter 6

SUMMARY AND CONCLUSIONS

Microstructural evolution in four different Ti-45Al based aluminides, namely Ti-45Al, Ti-45Al-2Nb, Ti-45Al-2Nb-0.4Mn and Ti-45Al-2Nb-2Mn, was studied during cooling from α-phase field. Based on the results and discussions of this study presented in the preceding chapters, following conclusions can be drawn:

1. Furnace cooling of the alloys from 1350°C resulted in a complete decomposition of the high temperature α-phase resulting in a fully lamellar microstructure.

2. Massive transformation was observed in all the four alloys when cooled at relatively high rates. With increased cooling rate the alloys' susceptibility to massive transformation increased. However, at very high cooling rates, the massive transformation was suppressed by the $\alpha \rightarrow \alpha_2$ ordering reaction.

3. It is suggested that massive transformation requires a certain critical cooling rate (CCR). The CCR was found to be dependent on the alloy composition, that is, the alloys' susceptibility to massive transformation was observed to vary with alloy composition.

4. The susceptibility to massive transformation decreased with increase in Mn concentration in the alloy, i.e. a much higher cooling rate was required to bring about massive transformation in the alloy containing highest concentration of Mn (alloy IV). The site preference of Mn in TiAl and its effect on phase boundaries were attributed for this influence of Mn on massive transformation.

5. Based on the microstructural characterization of variously heat-treated specimens, schematic CCT diagrams are proposed for the present alloys. Addition of Nb to binary Ti-45Al alloy shifted the curve for the lamellar structure formation and massive transformation to the right. Addition of Mn to ternary Ti-45Al-2Nb alloy caused the curves to shift to shorter time, that is, to the left.

6. Increase in Mn concentration in the alloy also increased the rate of massive transformation in rapidly cooled specimens. Increase in Mn concentration from 0 (alloy II) to 2 at.% (alloy IV) resulted in a significant increase in the volume fraction of massively transformed gamma (γ_m) from 0 to ~70 vol.%. An increase in rate of transformation has been attributed to the decrease in prior alpha grain size in higher Mn alloy.

7. At a fixed composition and cooling rate, an increase in grain size was found to decrease the rate of massive transformation. The log-log plot of volume fraction of massively transformed gamma and grain size yielded a straight line with a linear slope of –1.5. The negative slope is implicative of decrease in the volume fraction of

massively transformed gamma with grain size and hence, the rate of transformation. Increase in grain size also shifted the CCT curve to the right, that is, to longer time.

8. A mechanism for the massive transformation of alpha phase in titanium aluminides is proposed. According to the proposed mechanism, γ_m primarily nucleated incoherently at the prior alpha grain boundaries with occasional nucleation taking place inside the grains. The growth of nucleated γ_m then took place by transfer of atoms across the parent product interfaces.

9. Grain growth kinetics of Ti-45Al-2Nb (alloy II) and Ti-45Al-2Nb-0.4Mn (alloy III) alloys were studied by annealing at 1350°C for various time periods. It was found that alloy II exhibited a slower rate of grain growth. The grain growth exponent of alloy II was determined to be 0.38 and that for alloy III was 0.52.

10. Addition of Mn reduced the grain size in FC samples as well as increased the rate of massive transformation in rapidly cooled samples. Hence, it is suggested that alloy IV that had highest concentration of Mn would be more flexible to microstructural control and exhibit higher potential for grain refinement.

11. Hardness of heat-treated specimens increased with cooling rate. The Vickers pyramid hardness number increased from 280-290 to 400-440 with increase in cooling rate from FC to AC. The hardness of rapidly cooled specimens exhibited an increasing trend with a decrease in the volume fraction of massively transformed gamma. The

hardness of annealed alloys first increased with annealing time (grain size) and then decreased after a attaining a certain maximum value. No specific relationship between the hardness and grain size was observed.

Chapter 7

SUGGESTIONS FOR FUTURE WORK

1. The most plausible mechanism of massive transformation in TiAl-based alloys has been proposed within the scope of this research. However, to further ascertain and definitively establish the mechanism of transformation, it is required to meticulously analyze the nature of the interface between the parent and product phases. This could be achieved by electron back scattered diffraction pattern (EBSP) and/or high resolution transmission electron microscopy (HRTEM) analyses of the heat-treated specimens.

2. Room temperature ductility and strength of different alloys in various heat-treated conditions could be determined by tensile-pull testing of the samples prepared from variously heat-treated alloys. These tests will help establish relationship between mechanical properties and microstructure of the titanium aluminide alloys used in this research.

3. As shown in section 4.7, two-step cooling of alloy IV (Ti-45Al-2Nb-2Mn) resulted in moderately fine grain fully lamellar microstructure. In addition, as discussed in 5.7, alloy IV exhibits high potential of microstructural refinement. Appropriate thermal treatments could be designed to refine the microstructure and improve the mechanical properties of this alloy.

4. As discussed in section 5.1, Si-deposited on the surface of the samples during heat treatment and this caused undesirable changes near the surface of the specimen. A suitable surface treatment could be designed to prevent any surface damage during heat treatment of titanium aluminides.

REFERENCES

1. R.E.Schafrik, Structural Intermetallics, eds. K.J.Hemker *et al.*, 2001, p.13.
2. N.A.Walker and N.E.Glover, Structural Intermetallics, eds. K.J.Hemker *et al.*, 2001, p. 19.
3. W.Smarsley *et al*, Structural Intermetallics, eds. K.J.Hemker *et al.*, 2001, p. 25.
4. R.I.Prihar, Structural Intermetallics, eds. K.J.Hemker *et al.*, 2001, p. 819.
5. Y.W.Kim, JOM, 46 (7), 1994, p. 30.
6. P.A.Bartolotta and D.LKrause, Gamma Titanium Aluminides, eds. Y.W.Kim, D.M.Dimiduk and M.H.Loretto, TMS, 1999, p. 3.
7. D.Rugg, Gamma Titanium Aluminides, eds. Y.W.Kim, D.M.Dimiduk and M.H.Loretto, TMS, 1999, p. 11.
8. C.M.Austin *et al.*, Structural Intermetallics, eds. M.V.Nathal *et al.*, TMS, 1997, p. 413.
9. S.Isobe and T.Noda, Structural Intermetallics, eds. M.V.Nathal *et al.*, TMS, 1997, p. 427.
10. Y.W.Kim and D.M.Dimiduk, JOM, 43 (8), 1991, p. 40.
11. Y.W.Kim, JOM, July 1989, p. 24.
12. Y.W.Kim and D.M.Dimiduk, Structural Intermetallics, eds. M.V.Nathal *et al.*, TMS, 1997, p. 531.
13. S.C.Huang and J.C.Chesnutt, Intermetallic Compounds, vol.2, *Practice*, eds. J.H.Westbrook and R.L.Fleischer, John Wiley and Sons Ltd., 1994, p. 73.
14. Y.W.Kim, Acta Met., 40, 1992, p.1121.

15. Y.W.Kim, Gamma Titanium Alimindes, eds. Y.W.kim, R.Wagner and M.Yamaguchi, TMS, 1995, p. 637.

16. D.M.Dimiduk, Intermetallics, vol.6, 1998, p.613.

17. Y.W.Kim, Intermetallics, vol.6, 1998, p. 623.

18. T.Noda, Intermetallics, vol.6, 1998, p. 709.

19. H.R.Ogden *et al.*, Journal of Metals, vol. 3 (12), 1951, p. 1150.

20. E.S.Bumps, H.D.Kessler and M.Hansen, Journal of Metals, vol. 4 (6), 1952, p. 609.

21. J.L.Murray, Met. Trans., vol.19A, 1988, p.243.

22. C.McCullough *et al.*, Acta Met., vol. 37 (5), 1989, p. 1321.

23. S.A.Jones and M.J.Kaufman, Acta Met., vol.41(2), 1993, p.387.

24. J.J.Ding *et al.*, Journal of Phase Equilibria, vol. 17 (2), 1996, p.117.

25. U.R.Kattner, J.C.Lin and Y.A.Chang, Met. Trans., vol.23A, 1992, p. 2081.

26. G.Petzow and G.Effenberg (eds.), A Comprehensive Compendium of Evaluated Constitutional Data and Phase Diagram, vol. 7.

27. D.Veeraraghavan *et al.*, Acta Met., vol. 46 (2), 1998, p. 401.

28. J.C.Mishurda, J.C.Lin, Y.A.Chang and J.H.Perepezko, Mat. Sci. Symp. Proc., vol. 133, 1989, p. 57.

29. J.Braun and M.Ellner, Met. Trans., vol. 32A, 2001, p. 1037.

30. F.H.Froes, C.Suryanarayana, D.Eliezer, Journal of Material Science, vol. 27, 1992, p. 5113.

31. F.H.Froes and C.Suryanarayana, in Physical Metallurgy and Processing of Intermetallic Compounds, eds. N.S.Stoloff and V.K.Sikka, Chapman and Hall, 1996, p. 297.

32. D.Banerjee, Intermetallic Compounds, vol.2, *Practice*, eds. J.H.Westbrook and R.L.Fleischer, John Wiley and Sons Ltd., 1994, p. 91.

33. V.M.Imayev *etal.*, Structural Intermetallics, eds. M.V.Nathal *et al.*, 1997, p. 505.

34. Y.W.Kim, MRS Symp. Proc., vol. 213, 1991, p. 777.

35. L.A Bendersky *et al.*, Acta Met., vol. 38, 1990, p. 931.

36. R.Strychor, J.C.Williams and W.A.Soffa, Met. Trans., vol. 19A 1988, p. 225.

37. C.H.Ward, Int. Mat. Rev., vol. 38 (2), 1993, p.79.

38. H.A.Lipsitt, M.J.Blackburn and D.M.Dimiduk, Structural Intermetallics, eds. K.J.Hemker *et al.*, TMS, 2001, p.73.

39. D.M.Dimiduk, Gamma Titanium Aluminides, eds. Y.W.Kim, R.Wagner and M.Yamaguchi, TMS, 1995, p. 3.

40. J.H.Perepezko *et al.*, High Temperature Aluminides and Intermetallics, eds., S.H.Whang *et al.*, TMS, 1990, p.19.

41. Y.G.Li and M.H.Loretto, Acta Met., vol. 42 (6), 1994, 2009.

42. D.G.Konitzer, I.P.Jones and H.L.Fraser, Scripta Met., vol. 20, 1986, p. 265.

43. E.Mohandas and P.A.Beaven, Scripta Met., vol. 25, 1991, p. 2023.

44. Y.L.Hao *et al.*, Acta Met, vol. 47 (4), 1999, p. 1129.

45. C.Woodward, SA.Kajihara, S.I.Rao and D.M.Dimiduk, Gamma Titanium Aluminides, eds. Y.W.Kim, D.M.Dimiduk and M.H.Loretto, TMS, 1999, p. 49.

46. R.F.Domagala and W.Rostoker, Trans. ASM, vol. 48, 1955, p.565.

47. D.J.Chakrabarti, Met. Trans., vol. 8B, 1977, p. 121.

48. I.Jacob and D.Shaltiel, Mat. Res. Bull., vol. 13, 1978, p. 1193.

49. K.Hashimoto *et al.*, J. Jpn. Inst. Met., vol. 52, 1988, p. 816.

50. C.J.Butler *et al.*, Acta Met., vol. 45 (7), 1997, p. 2931.

51. C.J.Butler and D.G.McCartney, Acta Met., vol. 46 (6), 1998, p. 1875.

52. K.Kaltenbach *et al.*, Z. Metallkd., vol. 80, 1989, p. 535.

53. A.Hellwig, M.Palm and G.Inden, Intermetallics, vol. 6 (2), 1998, p.79.

54. T.J.Jewett *et al.*, MRS Symp. Proc., vol. 133, 1989, p. 133.

55. A.Zdziobek *et al.*, Z. Metallkd., vol. 86, 1995, p. 334.

56. E.S.K.Menon, P.R.Subramanian and D.M.Dimiduk, Scripta Met., vol. 27, 1992, p. 265.

57. G.L.Chen *et al.*, Intermetallics, vol. 4 (1), 1996, p. 13.

58. D.Banerjee, A.K.Gogia, T.K.Nandy and A.K.Joshi, Acta Met., vol. 36, 1988, p. 871.

59. K.Muraleedharan *et al.*, Met. Trans, vol. 23A, 1992, p. 401.

60. S.C.Huang and E.Hall, Met Trans., vol. 22A, 1991, p. 2619.

61. S.C.Huang and E.Hall, Acta Met., vol. 39, 1991, p. 1053.

62. T.Tsujimoto and K.Hashimoto, MRS Symp. Proc., vol. 133, 1989, p.391.

63. M.Morinaga, J.Saito, N.Yukawa and H.Adachi, Acta Met., vol. 38 (1), 1990, p. 25.

64. S.G.Pyo and N.J.Kim, Gamma Titanium Aluminides, eds. Y.W.Kim, R.Wagner and M.Yamaguchi, TMS, 1995, p. 779.

65. P.R.Bhowal, W.A.Konkel and H.F.Merrick, Gamma Titanium Aluminides, eds. Y.W.Kim, R.Wagner and M.Yamaguchi, TMS, 1995, p. 787.

66. M.L.VanMeter, S.L.Kampe and L.Christodoulou, Scripta Met, vol. 34 (8), 1996, p. 1251.

67. T.T.Cheng, Gamma Titanium Aluminides, eds. Y.W.Kim, D.M.Dimiduk and M.H.Loretto, TMS, 1999, p. 389.

68. T.Kawabata, H.Fukai and O.Izumi, Acta Met., vol. 46 (6), 1998, p. 2185.

69. M.Nobuki, D.Vanderscheuren and M.Nakamura, Acta Met., vol. 42 (8), 1994, p. 2623.

70. P.L.Martin, M.G.Mendiratta and H.A.Lipsitt. Met trans, vol. 14A, 1983, p.2170.

71. S.Tsuyama, S.Mitao and K.Minakawa, Mat. Sci. Engg. A, vol. 153A, 1992, p. 451.

72. W.M.Yin and V.Lupinc, Scripta Met., vol. 37 (2), 1997, p. 1545.

73. J.N.Wang and T.G.Nieh, Scripta Met., vol. 7 (10), 1997, p. 2775.

74. X.Du, J.N.Wang and J.Zhu, Scripta Met., vol. 45, 2001, p. 19.

75. J.Beddoes, W.Wallace and L.Zhao, Intl. Mat. Rev., vol. 40 (5), 1995, p. 197.

76. J.Beddoes, D.Y.Seo, W.R.Chen and L.Zhao, Intermetallics, vol. 9, 2001, p. 915.

77. D.Y.Seo *et al.*, Gamma Titanium Aluminides, eds. Y.W.Kim, R.Wagner and M.Yamaguchi, TMS, 1995, p.745.

78. M.Es-Souni, A.Bartels and R.Wagner, Acta Met., vol. 43 (1), 1995, p. 153.

79. J.Beddoes *et al.*, Gamma Titanium Aluminides, eds. Y.W.Kim, R.Wagner and M.Yamaguchi, TMS, 1995, p.959.

80. F.Sun *et al.*, Scripta Met., vol. 44, 2001, p. 2001.

81. W.H.Tian and M.Nemoto, Gamma Titanium Aluminides, eds. Y.W.Kim, R.Wagner and M.Yamaguchi, TMS, 1995, p.689.

82. C.T.Liu and P.J.Maziasz, Intermetallics, vol. 6, 1998, p. 653.

83. K.F.Yao, H.Inui, K.Kishida and M.Yamaguchi, Acta Met., vol. 43 (3), 1995, p. 1075.

84. Y.G.Li and M.H.Loretto, Acta Met., vol. 42 (9), 1994, p. 2913.

85. A.Denquin and S.Naka, Gamma Titanium Aluminides, eds. Y.W.Kim, R.Wagner and M.Yamaguchi, TMS, 1995, p.141.

86. Q.Xu, C.H.Lei and Y.G.Zhang, Gamma Titanium Aluminides, eds. Y.W.Kim, R.Wagner and M.Yamaguchi, TMS, 1995, p.189.

87. Y.Yamabe, M.Takeyama and M.Kikuchi, Scripta Met., vol. 30, 1994, p. 553.

88. C.R.Feng, D.J.Michel and C.R.Crowe, Scripta Met., vol. 22, 1988, p. 1481.

89. D.S.Schwartz and S.M.L.Sastry, Scipta Met., vol. 23, 1989, p. 1621.

90. Y.S.Yang and S.K.Wu, Scripta Met., vol. 24, 1990, p. 1801.

91. Y.S.Yang and S.K.Wu, Phil. Mag., vol. 65, 1992, p. 15.

92. L.Zhao and K.Tangri, Acta Met., vol. 39, 1991, p. 2209.

93. R.J.Mahon and J.M.Howe, Met. Trans., vol. 21A, 1990, pp, 1655.

94. Y.Zeng, L.Zhao and K.Tangri, Scripta Met., vol. 26, 1992, p. 219.

95. A.Denquin, S.Naka and T.Khan, Titanium '92:Science and Technology, eds. F.H.Froes and I.L.Caplan, TMS, p. 1017.

96. A.Denquin and S.Naka, Acta Met., vol. 44 (1), 1996, p. 343.

97. D.S.Shong and Y.W.Kim, Scripta Met., vol. 23, 1989, p. 254.

98. M.F.Bartholomeusz and J.A.Wert, Met. Trans., vol. 25A, 1994, p. 2371.

99. S.Mitao and L.A.Bendersky, Gamma Titanium Aluminides, eds. Y.W.Kim, R.Wagner and M.Yamaguchi, TMS, 1995, p.181.

100. G.Qin and S.Hao, Scripta Met., vol. 37 (7), 1997, p. 937.

101. S.Mitao and L.A.Bendersky, Acta Met, vol. 45 (11), 1997, p. 4475.

102. S.Mitao and L.A.Bendersky, Structural Intermetallics, eds. M.V.Nathal *et al.*, TMS, 1997, p. 177.

103. P.Wang, G.B.Viswanathan and V.K.Vaasudevan, Met. Trans., vol. 23A, 1992, p. 690.

104. P.Wang and V.K.Vasudevan, Scripta Met., vol. 27, 1992, p. 89.

105. A.Denquin and S.Naka, Acta Met., vol. 4 (1), 1996, p. 353.

106. E.Abe, T.Kumagai and M.Nakamura, Structural Intermetallics, eds. M.V.Nathal *et al.*, TMS, 1997, p. 167.

107. D.Veeraraghavan and V.K.Vasudevan, Mat. Sci. Engg., vol. A192/193, 1995, p. 950.

108. M.C.Chaturvedi, N.L.Richards and Q.Xu, Mat. Sci. Engg. A, vol. A239-240, 1997, p. 605.

109. Q.Xu, M.C.Chaturvedi and N.L.Richards, Met. Trans., vol. 30A, 1999, p. 1717.

110. X.D.Zhang, T.A.Dean and M.H.Loretto, Acta Met., vol. 42, 1994, p. 2035.

111. D.Veeraraghavan and V.K.Vasudevan, Gamma Titanium Aluminides, eds. Y.W.Kim, R.Wagner and M.Yamaguchi, TMS, 1995, p. 157.

112. Y.Yamabe, M.Takeyama and M.Kikuchi, Gamma Titanium Aluminides, eds. Y.W.Kim, R.Wagner and M.Yamaguchi, TMS, 1995, p. 111.

113. X.D.Zhang *et al.*, Acta Met., vol. 44 (9), 1996, p. 3723.

114. T.Kumagai, E.Abe, M.Takeyama and M.Nakamura, Scripta Met., vol. 36 (5), 1997, p. 523.

115. P.Wang, M.Kumar, D.Veeraraghavan and V.K.Vasudevan, Acta Met., vol. 46 (1), 1998, p. 13.

116. D.Veeraraghavan, P.Wang and V.K.Vasudevan, Acta Met., vol. 47 (11), 1999, p. 3313.

117. T.Kumagai, E.Abe and M.Nakamura, Met. Trans., vol. 29A, 1998, p. 19.

118. P.A.McQuay, D.M.Dimiduk and S.L.Semiatin, Scripta Met., vol. 25, 1991, p. 1689.

119. M.J.Blackburn, in The Science, Technology and Applications of Titanium, eds. R.I.Jaffee and N.E.Promisel, vol. 633, 1970.

120. S.Zghal, S.Naka and A.Couret, Acta Met., vol. 45 (7), 1997, p. 3005.

121. P.R.Bhowal, H.F.Merric and D.E.Larse, Jr., Mat. Sci, Engg A, vol. A192/193, 1995, p. 685.

122. P.J.Maziasz and C.T.Liu, Met. Trans., vol. 29A, 1998, p. 105.

123. J.D.Livingston and J.N.Cahn, Acta Met., vol. 22, 1974, p. 495.

124. F.Zhang, S.L.Chen, Y.A.Chang, U.R.Kattner, Intermetallics, vol. 5 (6), 1997, p. 471.

125. J.H.Perepezko, Met. Trans., vol. 15A, 1984, p. 437.

126. T.B.Massalski, Met. Trans., vol. 15A, 1984, p. 421.

127. J.F.Nie, B.C.Muddle, T.Furuhara and H.I.Aaronson, Scripta Met., vol. 39 (4 – 5), 1998, p. 637.

128. J.G.Lin, C.E.Wen, Y.G.Zhang and C.Q.Chen, Journal of Mat. Sci. Lett, vol. 18, 1999, p. 927.

129. G.E.Fuchs, Gamma Titanium Aluminides, eds. Y.W.Kim, R.Wagner and M.Yamaguchi, TMS, 1995, p. 563.

130. S.L.Semiatin, Gamma Titanium Aluminides, eds. Y.W.Kim, R.Wagner and M.Yamaguchi, TMS, 1995, p. 509.

131. M.A.Morris, M.Leboeuf and L.Batawi, Scripta Met., vol. 32 (1), 1995, p. 71.

132. S.J.Davey *et al.*, Titanium '95: Science and Technology, vol. I, 1995, p. 566.

133. D.Rugg, M.Kearns and S.A.Blackham, Titanium '95: Science and Technology, vol. I, 1995, p. 201.

134. Y.W.Kim, Mat. Sci. Engg. A, vol. A192-193, 1995, p. 519.

135. K.Chan and Y.W.Kim, Met. Trans., vol. 23A, 1992, p. 1663.

136. K.Chan, Gamma Titanium Aluminides, eds. Y.W.Kim, R.Wagner and M.Yamaguchi, TMS, 1995, p. 835.

137. S.C.Huang, US Patent # 5,228,931; July 1993.

138. Y.W.Kim and D.M.Dimiduk, Structural Intermetallics, eds. K.J.Hemker *et al.*, TMS, 2001, p. 625.

139. C.T.Liu *et al.*, Gamma Titanium Aluminides, eds. Y.W.Kim, R.Wagner and M.Yamaguchi, TMS, 1995, p. 679.

140. J.N.Wang and K.Xie, Scripta Met., vol. 43, 2000, p. 441.

141. W.J.Wang, E.Evangelista and L.Fracesconi, Scripta Met., vol. 35 (1), 1996, p. 41.

142. Y.Wang, J.N.Wang, Q.Xia and J.Yang, Mat. Sci. Engg. A, vol. A293, 2000, p. 102.

143. S.L.Semiatin, D.S.Lee and D.M.Dimiduk, US Patent # H,1659; July 1997.

144. L.Zhao, P.Au, J.C.Beddoes and W.Wallace, US Patent # 5,653,828; August 1997.

145. K.S.Chan and Y.W.Kim, Acta Met., vol. 43 (2), 1995, p. 439.

146. R.V.Ramanujan and P.J.Maziasz, Met. Trans., vol. 27A, 1996, p. 1661.

147. P.J.Maziasz, C.T.Liu and J.L.Wright, Structural Intermetallics, eds. M.V.Nathal *et al.*, TMS, 1997, p. 245.

148. D.Dudzinski, L.Zhao, J.Beddoes and W.Wallace, Scripta Met., vol. 35 (3), p. 367.

149. T.Tsuyama, S.Mitao and K.Minakawa, Mat. Sci. Engg. A, vol. A153, 1992, p. 451.

150. R.W.Hayes and P.A.McQuay, Scripta Met, vol. 30, 1994, p. 259.

151. B. London *et al.*, Structural Intermetallics, eds. R.Darolia *et al.*, TMS, 1993, p. 151.

152. U.Prasad, Q.Xu, M.C.Chaturvedi and A.K.Jena, Intermetallics, vol. 8, 2000, p. 125.

153. K.Maki *et al.*, Mat. Sci. Engg. A, vol. A153, 1992, p. 591.

154. O.Kubaschewski and C.B.Alcock, Metallurgical Thermochemistry (International Series on Material Science and Technology), vol. 24, Pergamon Press, NY, 1979.

155. M.R.Plichta, W.A.Clark and H.I.Aaronson, Met. Trans., vol. 15A, 1984, p. 427.

156. M.A.Morris and M.Leboeuf, Scripta Met., vol. 38, 1998, p. 369.

157. W.J.Zhang, L.Francesconi and E.Evangelista, Mat. Sci. Engg. A, vol. A220, 1996, p. 168.

158. J.Beddoes, L.Zhao and W.Wallace, Scripta Met., vol. 28, 1993, p. 383.

159. V.Seetharaman and S.L.Semiatin, Met. Trans., vol. 28A, 1997, p. 947.

160. S.L.Semiatin, V.Seetharaman, D.M.Dimiduk and K.H.G.Ashbee, Met. Trans., vol. 29A, 1998, p. 7.

161. E.E.Underwood, in Quantitative Microscopy, eds. R.T.DeHoff and F.N.Rhines, McGraw-Hill Book Company, 1968, p. 79.

162. W.J.Zhang, L.Francesconi, E.Evangelista and G.L.Chen, Scripta Met., vol. 37, 1997, p. 627.